



HAL
open science

Graphene based Composites with Cellulose Nanofibrils for Energy storage applications

Yasir Beeran Pottathara

► **To cite this version:**

Yasir Beeran Pottathara. Graphene based Composites with Cellulose Nanofibrils for Energy storage applications. Materials Science [cond-mat.mtrl-sci]. Université de Bretagne Sud, 2017. English. NNT : 2017LORIS450 . tel-01870276

HAL Id: tel-01870276

<https://theses.hal.science/tel-01870276>

Submitted on 7 Sep 2018

HAL is a multi-disciplinary open access archive for the deposit and dissemination of scientific research documents, whether they are published or not. The documents may come from teaching and research institutions in France or abroad, or from public or private research centers.

L'archive ouverte pluridisciplinaire **HAL**, est destinée au dépôt et à la diffusion de documents scientifiques de niveau recherche, publiés ou non, émanant des établissements d'enseignement et de recherche français ou étrangers, des laboratoires publics ou privés.



**Graphene Based Composites with
Cellulose Nanofibrils for Energy
Storage Applications**

Yasir Beeran POTTATHARA

Thesis Director: Prof. Yves GROHENS

Thesis Co-Director: Prof. Sabu THOMAS

Statement of Originality

I, Yasir Beeran POTTATHARA, formally submit the dissertation entitled “Graphene based composites with cellulose nanofibrils for energy storage applications” to University of South Brittany (UBS), Lorient, France for the acquirement of the academic degree of Doctor of Philosophy in Engineering Sciences. The work presented here was carried out from May 2014 till December 2016 at the International and Inter University Centre for Nanoscience and Nanotechnology, Mahatma Gandhi University, Kottayam India, Institute of Engineering Materials and Design, University of Maribor, Maribor, Slovenia and Laboratoire Ingenierie des Mateiriaux de Bretagne, UBS, Lorient Cedex, France. I hereby certify that this submission is solely my work and that, to the best of my knowledge and belief, it contains no material previously published or written by another person, except where due reference is made in the thesis itself. Neither the dissertation, nor any sections thereof, has been previously submitted for a degree or other qualification to any other University or Institution. Any contribution made to the research by others, with whom I have worked at the above-mentioned laboratories, is unambiguously acknowledged in the thesis.

Yasir Beeran POTTATHARA

Lorient, France

20-03-2017

Contents

<i>Contents</i>	1-7
<i>Acknowledgements</i>	8-9
<i>Chapter 1: Graphene-cellulose composites for energy storage applications</i>	13-34
<i>1. Introduction</i>	
<i>1.1 Energy storage systems</i>	
<i>1.1.1 Conventional capacitors</i>	
<i>1.1.2 Batteries</i>	
<i>1.1.3 Electrochemical capacitors</i>	
<i>1.2 Selection of materials for high charge storage capacity</i>	
<i>1.2.1 Polymer composites</i>	
<i>1.2.1.1 Graphene as a filler material</i>	
<i>1.2.1.2 Synthesis of graphene based fillers</i>	
<i>1.2.1.3 Cellulose as a matrix</i>	
<i>1.2.1.4 Chemical modifications on cellulose</i>	
<i>1.3 Graphene- cellulose composites for energy storage applications</i>	
<i>1.4 Objectives of research</i>	
<i>1.5 References</i>	

Chapter 2: Materials and methods.....35-44

2.1 Introduction

2.2 Materials

2.3 Methods of fabrication of different nanocomposites

2.3.2 Fabrication of ammonia functionalized graphene oxide (NGO) filled pristine and oxidized cellulose nanofibrils (CNF) composites

2.3.3 Fabrication of graphene oxide (GO) filled pristine and oxidized cellulose nanofibrils (CNF) composites

2.3.4 Fabrication of thermally reduced graphene oxide (RGO) filled cellulose nanofibrils (CNF) composites as film like xerogels and cryogels

2.4 Characterization techniques

2.4.1 Potentiometric titration

2.4.2 Raman spectroscopy

2.4.3 Attenuated Total Reflectance - Fourier Transform Infrared (ATR-FTIR)

2.4.4 X-Ray diffraction (XRD) analysis

2.4.5 UV-Visible spectroscopy analysis

2.4.6 Contact angle and surface energy analysis

2.4.7 Transmission Electron Microscopy (TEM)

2.4.8 Scanning Electron Microscopy (SEM)

2.4.9	<i>Tensile strength analysis</i>	
2.4.10	<i>Dynamic mechanical analysis (DMA)</i>	
2.4.11	<i>Thermal Gravimetric Analysis (TGA)</i>	
2.4.12	<i>Dielectric studies</i>	
2.4.13	<i>Cyclic voltammetry (CV) analysis</i>	
2.4.14	<i>Electrochemical impedance spectroscopy (EIS)</i>	
2.5	<i>Conclusions</i>	
2.6	<i>References</i>	

Chapter 3: Oxidization of pristine CNF using TEMPO reagent and synthesis, reduction and characterization of graphene oxide (GO).....45-60

3.1	<i>Summary</i>	
3.2	<i>Oxidization of pristine cellulose nanofibrils</i>	
3.3	<i>Characterization of pristine and oxidized CNF</i>	
3.3.1	<i>Potentiometric titration analysis</i>	
3.3.2	<i>ATR-FTIR analysis</i>	
3.3.3	<i>XRD studies</i>	
3.3.4	<i>UV-Visible spectroscopy analysis</i>	
3.3.5	<i>Scanning Electron Microscopy (SEM) studies</i>	

- 3.4 *Synthesis of graphene oxide*
- 3.5 *Characterization of synthesized graphene oxide*
 - 3.5.1 *Transmission Electron Microscopy (TEM) studies*
 - 3.5.2 *XRD analysis*
 - 3.5.3 *Raman spectroscopy*
 - 3.5.4 *ATR-FTIR analysis*
- 3.6 *UV induced reduction of graphene oxide (GO) filled pristine and oxidized CNF composites*
 - 3.6.1 *UV irradiation experiment*
- 3.9 *Thermal reduction of graphene oxide (GO)*
- 3.10 *Characterization of thermally reduced graphene oxide (RGO)*
 - 3.10.1 *Transmission Electron Microscopy (TEM) studies*
 - 3.10.2 *XRD analysis*
 - 3.10.3 *Raman spectroscopy*
 - 3.10.4 *ATR- FTIR analysis*
- 3.11 *Conclusions*
- 3.12 *References*

Chapter 4: Structure, morphology, mechanical, dielectric and electrochemical storage properties of ammonia functionalized graphene oxide (NGO) filled pristine and oxidized cellulose nanofibrils (CNF) composites.....61-85

- 4.1 Summary
- 4.2 ATR-FTIR spectroscopy analysis
- 4.3 XRD studies
- 4.4 UV-visible spectra analysis
- 4.5 Contact angle and surface energy studies
- 4.6 Scanning Electron Microscopy (SEM) studies
- 4.7 Mechanical properties
- 4.8 Thermal properties
- 4.9 Dielectric properties
- 4.10 Electrochemical properties
- 4.11 Conclusions
- 4.12 References

Chapter 5: Structure, morphology, mechanical, dielectric and electrochemical properties of untreated and UV treated composites of graphene oxide (GO) filled pristine and oxidized cellulose nanofibril composites.....86-107

- 5.1 *Summary*
- 5.3 *Potentiometric titration studies*
- 5.4 *ATR-FTIR spectroscopy analysis*
- 5.5 *XRD analysis*
- 5.6 *UV-Visible spectra studies*
- 5.7 *Dynamic mechanical analysis (DMA) studies*
- 5.8 *Dielectric properties of untreated composites*
- 5.9 *Dielectric properties of UV treated composites with different treatment time*
- 5.10 *Electrochemical properties of untreated and UV treated composites*
- 5.11 *Conclusions*
- 5.12 *References*

Chapter 6: Structure, morphology, dielectric and electrochemical storage properties of thermally reduced graphene oxide (RGO) filled cellulose nanofibrils based xerogels and cryogels.....108-124

- 6.1 *Summary*
- 6.2 *ATR-FTIR spectroscopy analysis*
- 6.3 *XRD analysis*
- 6.4 *Scanning Electron Microscopy (SEM) studies of composite films*
- 6.5 *Temperature dependent dielectric properties of films*

6.6 *SEM analysis of aerogel composites*

6.7 *BET analysis of film and aerogels*

5.9 *Electrochemical properties of film and aerogel composites*

5.10 *Conclusions*

5.11 *References*

Chapter 7: Conclusions and Perspectives.....125-128

Chapter 1

Graphene-cellulose composites for energy storage applications

1. Introduction

As the population of human kind continues to grow, there is a strong motive to achieve sustainable and renewable energy resources due to global warming, depleting fossil fuels and climate change. Hydroelectricity, solar and wind energy, geothermal and bioenergy, wave and tidal power technologies are fulfilling our energy efficiency in sustainable and renewable way. Eco friendly electric cars and vehicles nowadays providing a clean energy source and competing against greenhouse gas emission. These energy resources are not available on demand; besides, the cost of energy has risen steeply as crude oil and gas prices continue to rise. Moreover, the production of hydroelectric, solar and wind energies remains luxurious. These scenarios highly recommending the prerequisite for energy storage. Therefore, the necessity for energy storage devices, whether stationary or mobile, is inevitable. and playing a major role in our lives.

1.1 Energy storage systems

The increased energy consumption by the entire world motivating the need of alternative energy production and storage. Presently the most familiar energy storage devices are capacitors, batteries and fuel cells. Especially Electrochemical capacitors or supercapacitors and lithium-ion batteries are replacing conventional fossil fuel-based energy sources. Fig 1.1 shows a Ragone plot, a plot of specific power against specific energy, for various energy storage devices.

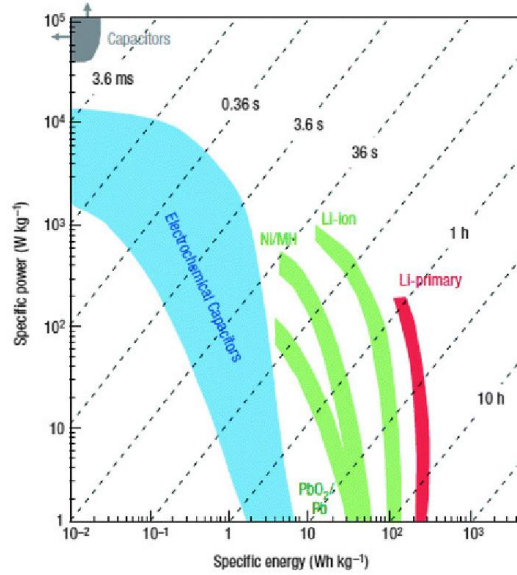


Fig. 1.1: Specific power vs. specific energy (Ragone plot) for different energy storage devices. Reprinted by permission Nature Materials, [1], copyright (2008)

1.1.1 Conventional capacitors

Commonly, a capacitor system stores energy as electric charge using a dielectric material separated with two conductive plates, as demonstrated in Figure 1.2. When a voltage is applied across the two electrodes of the material, charges get separated from the dielectric system. The positive charges (cations) get accumulated to the negatively charged electrodes and negative charges (anions) get attracted to the positively charged electrode, thus generating an electric field and stores energy.

The capacitance, C , of a capacitor is the ratio of charge, Q to the applied voltage, V

$$\text{Capacitance, } C = \frac{Q}{V} \quad (1)$$

Generally, a capacitor with two parallel plates having a surface area of A separated by a dielectric medium with a permittivity of ϵ and a thickness of d , the voltage is defined as

$$\text{Voltage, } V = \frac{Qd}{A} \quad (2)$$

Therefore, the capacitance would be as:

$$\text{Capacitance, } C = \frac{\epsilon A}{d} \quad (3)$$

Mostly, conventional capacitors can distribute large amount of power, but they can store less amount of energy.

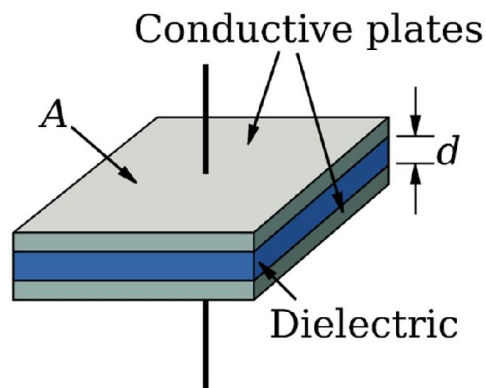


Fig.1.2: Schematic of a conventional capacitor with a dielectric

1.1.2 Batteries

Batteries are energy storage devices that convert the stored chemical energy directly into electrical energy by the means of redox reactions. Generally, an electric battery consists of one or more electrochemical cells with two electrodes which are connected to an electrolyte. Redox reactions power the battery. At the time of charging, cations are reduced, while anions are oxidized. The whole process is reversed during discharge.

Lithium-ion (Li-ion) batteries are now a commonly used type of rechargeable batteries offering light weight, low-discharge rates and environmental benefits. The working principle of a li-ion

battery explains as; while charging, lithium ions is inserted into electrodes and while discharge, lithium ions is extracted from the electrode. Li-ion batteries are common in home electronics.

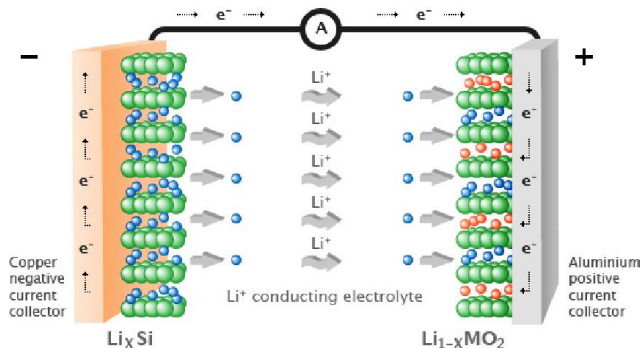


Fig.1.3: Schematic of the working principle of Li-ion battery

1.1.3 Electrochemical capacitors

Electrochemical capacitors, regularly called as supercapacitors or ultracapacitors are a class of energy storage devices that links the gap between conventional capacitors and batteries. These kinds of electrochemical capacitors have high capacitance value than other capacitors also having high specific power and long cycle life and outstanding power density [2-5]. Supercapacitors have efficiently been used in various fields such as automobiles, electrical load leveling in stationary and transport systems, etc. [6].

Supercapacitors stores energy in the form of charge at the electrode/electrolyte interface of materials. Supercapacitors are subdivided in to (a) electrochemical double layer capacitors (EDLCs) and (b) pseudocapacitors. EDLCs stores charges electrostatically just like conventional capacitors. In the case of double layer capacitors, the sandwiched electrode material which is soaked with electrolyte is attached to the current collector. Upon the application of a voltage across the electrodes, charges will accumulate on the electrode surface. This charge accumulation leads to the distribution of opposite charges across the separator; leading to the creation of double layer

on each electrode. The few nanometer thicknesses of this electrode layer along with high surface electrodes, EDLCs has a high capacitance than conventional capacitors. The total capacitance of the EDLCs system of two parallel plates would be as the following form

$$\frac{1}{C_{cell}} = \frac{1}{C_1} + \frac{1}{C_2} \quad (4)$$

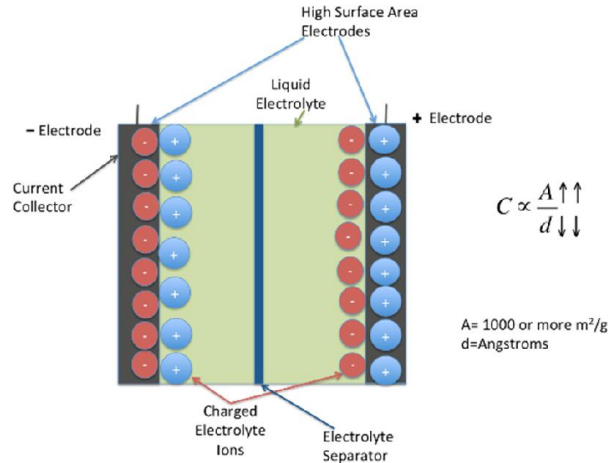


Fig.1.4: Schematic of the working principle of a double layer supercapacitor

In contrast to traditional capacitors and electrochemical double layer capacitors, pseudocapacitors have faradaic nature, means these kind of capacitors transfers charges between the electrode and electrolytes. Because of the fast charging and discharging of these devices they look like actual capacitors. If Δq is the charge transferred and Δv is the electrode potential, the capacitance of a pseudocapacitor electrode can be calculated as [7]

$$C = \frac{\Delta q}{\Delta v} \quad (5)$$

Metal oxides such as manganese oxide, nickel hydroxide and ruthenium oxide and conducting polymers such as polyaniline (PANI) and polypyrrole (PPy) are the most widely used pseudocapacitor materials.

1.2 Selection of materials for high charge storage capacity

Modern electronics and electric power systems highly requires the dielectric materials for controlling and storing charges and electrical energy. The development of high dielectric constant materials has become one of the major scientific and technology issues [8 and 9]. A material with high dielectric constants are highly required not only for the use of as capacitor dielectrics, but also in a wide range of advanced electromechanical applications, such as high frequency transducers, actuators and sonars [10].

1.2.1 Polymer composites

Polymer composites with high dielectric constant have been increasingly demanded than ceramic based composites [11] for energy storage devices in microelectronics [12], electric actuators [13], electromagnetic interference shielding [14], embedded capacitors [15], and flexible electronics [16]. For gas sensors and supercapacitor applications, materials with high values of dielectric constants are more advantageous [17]. Researchers paying their attention to develop polymer based composites with conducting nanofillers, especially graphene or carbon nanotubes, because of their better electrical properties and aspect ratio for energy storage applications [18-21]. More particularly, graphene derivatives are abundant, easy to process and cheaper than carbon nanotubes.

1.2.1.1 Graphene as a filler material

In recent years, there has been an upsurge in scientific motivation for using carbonaceous materials for various applications in the field of physical, chemical and biological sciences. Graphene, a primary building block of graphite, having one-atom-thick sheet of hexagonally arranged sp^2 -hybridized carbon atoms. The graphitic layers have lamellar structure and stacked

together by van der Waals forces. It was predicted that these individual layers have extraordinary electronic properties [22]. Graphene has extraordinary electrical and thermal conductivities, ultra-high theoretic specific surface area ($\sim 2630 \text{ m}^2/\text{g}$) and high mechanical strength [23]. These excellent properties make graphene a promising candidate for energy storage devices, composites and electronics. High specific surface area and electrical conductivity with mechanical strength make this material a promising choice for energy storage devices.

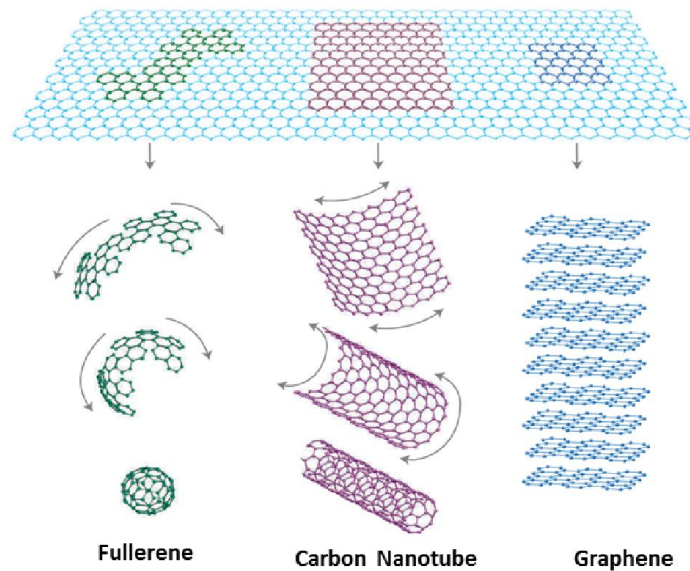


Fig. 1.4: Various graphitic forms. Reprinted by permission Nature Materials, [24], copyright (2007)

1.2.1.2 Synthesis of Graphene based fillers

There are a lot of routes available for graphene synthesis using different starting materials like graphite oxide, graphite intercalated compounds (GICs) and graphene oxide (GO) [25]. For the preparation of graphitic forms, many methods are existing including liquid intercalation, two-zone vapor transport, electro-chemical and co-intercalation techniques. Synthesis routes of graphite oxide and graphene oxide (GO) are reported by Brodie [26] Staudenmaier [27] and

Hummers and Offeman [28]. By these routes, graphite is oxidized by means of KMnO_4 , H_2SO_4 , and NaNO_3 . The improved synthesis of graphene oxide was reported later with excluding NaNO_3 and increasing the amount of KMnO_4 in the presence of $\text{H}_2\text{SO}_4 / \text{H}_3\text{PO}_4$ mixture [29]. The functional ketone, hydroxyl and epoxy groups present in the graphene oxide are very useful for the covalent bond links and excellent dispersibility in a polymer matrix by generating interfacial bonding with the polymer matrix [25 and 30-31].

Rapid pyrolysis and surface modifications of graphene oxide or graphite oxide is a possible method for the formation of graphene or graphite nanoplatelets (GNPs). By the modification, either chemical or thermal, of graphite and graphene oxide (GO), reduce graphene oxide (r-GO), is prepared. The chemical reduction of graphene oxide is mainly carried out with the presence of hydrazine [32] and dimethyl hydrazine [33]. Some chemical reduction was reported with the help of hydroquinone [34] and UV-irradiated TiO_2 [35]. However, the use of toxic chemicals and their high cost are the drawbacks of the chemical reduction. Thermal reduction of graphene oxide was possible by quick heating of dried graphene oxide at higher temperature under inert gas atmosphere [36]. The graphene sheets produced by this method would be exfoliated and wrinkled due to the disruption of interlayer van der Waals forces [37]. This method gives the advantage of high electrical conductivity in addition to the avoidance of organic solvents for dispersion.

1.2.1.3 Cellulose as matrix

Cellulose have become extensively interesting recently in scientific and industrial fields as a promising sustainable substrate material for its versatile usage also in flexible energy storage devices [38]. Cellulose accumulates as the most abundant biopolymer in earth principally in wood biomass. Moreover, cellulose can be extracted from agricultural or bio waste which makes it more economically viable. Cellulose fibres, in original form as well as mechanically and chemically

modified form, were using over a long history in various fields such as paper, textile, liquid crystal displays, hollow fibres for artificial kidney dialysis, and food additives [39]. The basic chemical structure of cellulose is given in fig.1.5. It consists of a linear homo polysaccharide consisting of D-glucopyranose units linked together by β -1-4-linkages. The hydroxyl groups attached with each monomer enables cellulose for the formation of crystalline structure and various physical properties.

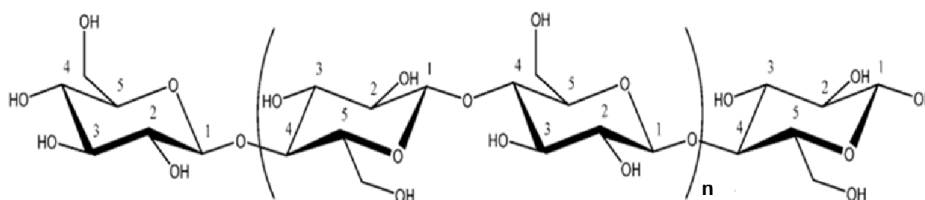


Fig. 1.5: Basic chemical structure of cellulose. Reprinted by permission ACS Chemical Reviews [46], copyright (2010)

There are two kinds of nano sized cellulosic derivatives such as cellulose nanofibrils (CNF) and cellulose nanowhiskers or cellulose nanocrystals (CNC). In the case of cellulose nanowhiskers, the amorphous phase can be removed due to the acid hydrolysis of native celluloses and successive mechanical agitation of the acid-hydrolyzed residues in water results highly crystalline nature. Cellulose nanofibrils (CNF) refers to individual microfibrils or cellulose microfibril aggregates obtained from plant cell wall [40]. Turbak et al were first produced CNF in 1983 by subjecting a wood pulp slurry to a homogenizer with high mechanical forces [50]. These nanofibers have a few micrometers length with a typical lateral dimension of 5–20 nm. It has been widely used as a biodegradable matrix material for flexible dielectrics due to their light weight nature, low price, high aspect ratio (greater than 250) [41] and crystallinity [42], excellent

transmittance [43], high flexibility [44], high mechanical strength (200-400 MPa) including to high modulus (up to 145 GPa) [45] and low coefficient of thermal expansion (12-28.5 ppm K⁻¹) [42].

1.2.1.4 Chemical modifications on cellulose

Generally, the chemical modifications are performed on the three alcoholic hydroxyl groups of cellulose. Primary hydroxyl group at C-6 and secondary hydroxyls at C-2 and C-3 participate on the modifications such as esterification, etherification and oxidation reactions. Besides, silylation, mercerization, peroxide treatment, benzylation, graft copolymerization are the other reported methods of surface modifications on cellulose fibres.

Silane modification generally reducing the number of hydroxyl groups at fibre-matrix interface which results improved degree of cross linking in the interface region and offer a perfect covalent bonding with the cell wall [47]. On the other hand, mercerization process reduces the fibre diameter and increasing the aspect ratio with a rough surface topography resulting high quality cellulose fibres with improved mechanical properties [48 and 49]. Organic peroxides easily decompose to free radicals and further react with the matrix and cellulose fibres resulting improved mechanical properties. Benzylation treatment generally decreasing the hydrophilicity of cellulosic materials [49].

2,2,6,6-tetramethylpiperidine-1-oxyl radical (TEMPO) and its analogues are water-soluble, and stable nitroxyl radicals. Cellulose fibers after the TEMPO mediated oxidation have mostly uniform diameters of 3–4 nm and large aspect ratios of >50, and are dispersed as individual nanofibrils in water [51]. TEMPO mediated oxidation simply relies on the catalytic oxidation of 2,2,6,6-tetramethylpiperidine-1-oxyl radical in water. This kind of modification has been applied to cellulose derivatives for preparing individual fibers by the selective conversion of primary

hydroxyl groups to carboxylate groups, using NaBr and NaClO as an additional catalyst and primary oxidant, respectively, at pH 9-11[52-55]. Transparent and highly viscous TEMPO oxidized cellulose nanofibrils (TCNF)/water dispersions will be obtained due to the effective electrostatic repulsion between negatively charged TCNFs during and after the nanofibrillation process. The formation of inter-fibril hydrogen bonds in nanocellulose is expected to improve their mechanical properties.

1.3 Graphene-cellulose composites for energy storage applications

Graphene-cellulose composites were mostly reported so far as a biodegradable material for dielectric storage and electrochemical charge storage applications such as supercapacitors. For dielectric applications, the dielectric constant of a graphene-cellulose nanocomposites is the measure of micro-capacitors which are formed by graphene sheets acting as electrodes filled with insulating matrices, cellulose, and the polarization centres which are initiated from the defects in the graphene structure [56]. For a polymer composites, the dielectric performance originates from the Maxwell–Wagner–Sillars (MWS) polarization effect in which the polymer–filler interfacial interaction is necessary to induce changes. The nanocomposite provides the enormous interfacial area for abundant sites for the reinforced MWS effect [57]. When a current flow across the two-material dielectric interfaces, GO sheets and CNFs matrices, charges accumulate at the interface because of the presence of functional groups and conjugation on the GO sheet surface, which forms an effective capacitor network to store energy [58].

Several studies have been reported on the enhancement of dielectric responses of various cellulose materials with graphene-based fillers [59-61]. These cases, dielectric responses were focussed on the lower frequency regions of the dielectric permittivity of the materials. Generally, the dielectric constant increases with frequency-lowering due to the space charge contribution.

Moreover, at low frequencies, the external effects, such as the presence of surface layers (for example, due to the formation of Schottky barriers) often govern the dielectric response [62]. The dielectric properties of cellulose/GO composites were studied by Kafy et al at 20 Hz and achieved for 190 times enhancement for the 3 wt% GO filled composites rather than neat cellulose. Mohiuddin et al. reported an 80% increase in the dielectric constant in modified reduced GO/cellulose acetate composites compared to the neat cellulose acetate at 150 Hz. Sadasivuni et al described the dielectric enhancement of reduced GO/cellulose films at 22 Hz and 1 KHz and obtained 44 and 4 times improvements respectively over neat polymer.

Since the electrochemical energy storage properties of polymer composites is mainly depended on the homogeneous dispersion of additives, interfacial interaction, surface area and pore structure, several kinds of strategies were used to alter these parameters. Cellulose composites incorporated with graphene derivatives were reported as both paper electrodes [63, 64] and three dimensional porous structures [65, 66] for supercapacitor applications. Better electrical conductivity, high surface area and high porosity with three dimensional networks, aerogels, sometimes called as cryogels, are promising electrode materials for supercapacitor devices than conventional paper electrodes [67]. For achieving outstanding performance for a supercapacitor electrode, the transfer of ions through the electrolyte must be stable and to ensure the effective diffusion or mass transfer through it [68]. The large specific surface area of $\sim 2630 \text{ m}^2 \text{ g}^{-1}$ and electronic transport of graphene sheets with the advantage of porous network of cellulose fibrils may attain the tremendous electrochemical storage properties [69].

Flexible graphene-cellulose paper electrode fabricated by weng *et al* [63] showed a capacitance per geometric area of 81 mF cm^{-2} while graphene filled cellulose fibres as a flexible double layer supercapacitor displays a capacity of 252 F/g at a current density of 1 A/g [64].

Ouyang *et al* [65] fabricated 3D graphene filled cellulose aerogels with a specific capacitance of 71.2 F/g whereas CNF–RGO hybrid aerogel based flexible supercapacitor reported by Gao *et al* [66] having a capacitance of 207 F g⁻¹.

1.4 Objectives of research

The goal of this work is to fabricate a biodegradable electrode materials based on pristine and oxidized cellulose nanofibrils (CNF) with different graphene based fillers such as graphene oxide (GO), ammonia functionalized graphene oxide (NGO) and reduced graphene oxide (RGO) for dielectric storage as well as electrochemical charge storage applications.

1. Fabrication of flexible dielectric papers with high mechanical strength based on biodegradable cellulose nanofibers for dielectric energy storage.
2. Detailed dielectric analysis on the higher frequency region to investigate the intrinsic material properties.
3. The reduction of graphene oxide to graphene by UV irradiation in cellulose composites as a dry method for promising alternative to solvent based methods.
4. Electrochemical studies for both pristine and oxidized cellulose-graphene composites electrodes
5. Comparison of electrochemical properties of film like xerogels and porous cryogel composites by vacuum filtration and one-directional freezing respectively.

To accomplish the goals, various experimental techniques and equipments will be used to characterize the composite material such as Scanning Electron Microscope (SEM), Transmission Electron Microscope (TEM), UV- Visible and Raman spectroscopy, Attenuated Total Reflectance-Fourier Transform Infrared (ATR-FTIR) spectroscopy, X-ray Diffraction

(XRD) analysis, Tensile strength and dynamic mechanic analysis (DMA), Thermal gravimetric analysis (TGA), dielectric measurements and electrochemical studies such as Cyclic Voltammetry (CV), electrochemical Impedance spectroscopy (EIS).

1.5 References

2. Simon, Patrice, and Yury Gogotsi. "Materials for electrochemical capacitors." *Nature materials* 7.11 (2008): 845-854.
3. Yu, Xinzhi, Bingan Lu, and Zhi Xu. "Super Long-Life Supercapacitors Based on the Construction of Nanohoneycomb-Like Strongly Coupled CoMoO₄-3D Graphene Hybrid Electrodes." *Advanced Materials* 26.7 (2014): 1044-1051.
4. Portet, Cristelle, et al. "High power density electrodes for carbon supercapacitor applications." *Electrochimica Acta* 50.20 (2005): 4174-4181.
5. Karden, Eckhard, et al. "Energy storage devices for future hybrid electric vehicles." *Journal of Power Sources* 168.1 (2007): 2-11.
6. Oakes, Landon, et al. "Surface engineered porous silicon for stable, high performance electrochemical supercapacitors." *Scientific reports* 3 (2013).
7. Béguin, François, and Elzbieta Frackowiak, eds. *Carbons for electrochemical energy storage and conversion systems*. CRC Press, 2009.
8. Conway, B. E., and W. G. Pell. "Double-layer and pseudocapacitance types of electrochemical capacitors and their applications to the development of hybrid devices." *Journal of Solid State Electrochemistry* 7.9 (2003): 637-644.
9. Reynolds, T. G., and Relva C. Buchanan. "Ceramic capacitor materials." *MATERIALS ENGINEERING-NEW YORK*- 25 (2004): 141-206.
10. Scott, J. F. "Applications of modern ferroelectrics." *science* 315.5814 (2007): 954-959.
11. Zhang, Q. M., et al. "An all-organic composite actuator material with a high dielectric constant." *Nature* 419.6904 (2002): 284-287.

12. Min, Chao, et al. "A graphite nanoplatelet/epoxy composite with high dielectric constant and high thermal conductivity." *Carbon* 55 (2013): 116-125.
13. Dang, Zhi-Min, et al. "Flexible nanodielectric materials with high permittivity for power energy storage." *Advanced Materials* 25.44 (2013): 6334-6365.
14. Huang, Xingyi, et al. "Role of interface in highly filled epoxy/BaTiO₃ nanocomposites. Part I-correlation between nanoparticle surface chemistry and nanocomposite dielectric property." *IEEE Transactions on Dielectrics and Electrical Insulation* 21.2 (2014): 467-479.
15. Kashi, Sima, et al. "Dielectric properties and electromagnetic interference shielding effectiveness of graphene-based biodegradable nanocomposites. " *Materials & Design* 109 (2016): 68-78.
16. Zhang, Xin, et al. "Ultrahigh Energy Density of Polymer Nanocomposites Containing BaTiO₃@ TiO₂ Nanofibers by Atomic-Scale Interface Engineering." *Advanced Materials* 27.5 (2015): 819-824.
17. Tong, Wangshu, et al. "Achieving significantly enhanced dielectric performance of reduced graphene oxide/polymer composite by covalent modification of graphene oxide surface." *Carbon* 94 (2015): 590-598.
18. Hong, Xinghua, and D. D. L. Chung. "Exfoliated graphite with relative dielectric constant reaching 360, obtained by exfoliation of acid-intercalated graphite flakes without subsequent removal of the residual acidity." *Carbon* 91 (2015): 1-10.
19. Chen, Zhe, et al. "Achieving large dielectric property improvement in polymer/carbon nanotube composites by engineering the nanotube surface via atom transfer radical polymerization." *Carbon* 95 (2015): 895-903.

20. Wan, Yan-Jun, et al. "Covalent polymer functionalization of graphene for improved dielectric properties and thermal stability of epoxy composites." *Composites Science and Technology* 122 (2016): 27-35.
21. Ge, Dengteng, et al. "Foldable supercapacitors from triple networks of macroporous cellulose fibers, single-walled carbon nanotubes and polyaniline nanoribbons." *Nano Energy* 11 (2015): 568-578.
22. Yuan, Kai, et al. "Nanofibrous and graphene-templated conjugated microporous polymer materials for flexible chemosensors and supercapacitors." *Chemistry of Materials* 27.21 (2015): 7403-7411.
23. Wallace, Philip Richard. "The band theory of graphite." *Physical Review* 71.9 (1947): 622.
24. Inui, Tetsuji, et al. "A miniaturized flexible antenna printed on a high dielectric constant nanopaper composite." *Advanced Materials* 27.6 (2015): 1112-1116.
25. Geim, Andre K., and Konstantin S. Novoselov. "The rise of graphene." *Nature materials* 6.3 (2007): 183-191.
26. Gao, Wei, et al. "New insights into the structure and reduction of graphite oxide." *Nature chemistry* 1.5 (2009): 403-408.
27. Brodie, B. "Note sur un nouveau procédé pour la purification et la désagrégation du graphite." *Ann. Chim. Phys* 45 (1855): 351-353.
28. Staudenmaier, L. "Verfahren zur darstellung der graphitsäure." *Berichte der deutschen chemischen Gesellschaft* 31.2 (1898): 1481-1487.
29. William, S., J. R. Hummers, and Richard E. Offeman. "Preparation of graphitic oxide." *J Am Chem Soc* 80.6 (1958): 1339.

30. Marcano, Daniela C., et al. "Improved synthesis of graphene oxide." *ACS nano* 4.8 (2010): 4806-4814.
31. Mkhoyan, K. Andre, et al. "Atomic and electronic structure of graphene-oxide." *Nano letters* 9.3 (2009): 1058-1063.
32. Novoselov, Kostya S., et al. "Electric field effect in atomically thin carbon films." *science* 306.5696 (2004): 666-669.
33. Romasanta, Laura J., et al. "Functionalised graphene sheets as effective high dielectric constant fillers." *Nanoscale research letters* 6.1 (2011): 1.
34. Stankovich, Sasha, et al. "Graphene-based composite materials." *nature* 442.7100 (2006): 282-286.
35. Wang, Guoxiu, et al. "Facile synthesis and characterization of graphene nanosheets." *The Journal of Physical Chemistry C* 112.22 (2008): 8192-8195.
36. Williams, Graeme, Brian Seger, and Prashant V. Kamat. "TiO₂-graphene nanocomposites. UV-assisted photocatalytic reduction of graphene oxide." *ACS nano* 2.7 (2008): 1487-1491.
37. Yang, Xiaoming, et al. "Synthesis and characterization of layer-aligned poly (vinyl alcohol)/graphene nanocomposites." *Polymer* 51.15 (2010): 3431-3435.
38. McAllister, Michael J., et al. "Single sheet functionalized graphene by oxidation and thermal expansion of graphite." *Chemistry of materials* 19.18 (2007): 4396-4404.
39. Zhang, Yi-Zhou, et al. "Flexible supercapacitors based on paper substrates: a new paradigm for low-cost energy storage." *Chemical Society Reviews* 44.15 (2015): 5181-5199.

40. Isogai, Akira, Tsuguyuki Saito, and Hayaka Fukuzumi. "TEMPO-oxidized cellulose nanofibers." *Nanoscale* 3.1 (2011): 71-85.
41. Moon, Robert J., et al. "Cellulose nanomaterials review: structure, properties and nanocomposites." *Chemical Society Reviews* 40.7 (2011): 3941-3994.
42. Saito, Tsuguyuki, et al. "Cellulose nanofibers prepared by TEMPO-mediated oxidation of native cellulose." *Biomacromolecules* 8.8 (2007): 2485-2491.
43. Fukuzumi, Hayaka, et al. "Transparent and high gas barrier films of cellulose nanofibers prepared by TEMPO-mediated oxidation." *Biomacromolecules* 10.1 (2008): 162-165.
44. Yagyu, Hitomi, et al. "Chemical Modification of Cellulose Nanofibers for the Production of Highly Thermal Resistant and Optically Transparent Nanopaper for Paper Devices." *ACS Applied Materials & Interfaces* 7.39 (2015): 22012-22017.
45. Zhu, Hongli, et al. "Biodegradable transparent substrates for flexible organic-light-emitting diodes." *Energy & Environmental Science* 6.7 (2013): 2105-2111.
46. Iwamoto, Shinichiro, et al. "Elastic modulus of single cellulose microfibrils from tunicate measured by atomic force microscopy." *Biomacromolecules* 10.9 (2009): 2571-2576.
47. Habibi, Youssef, Lucian A. Lucia, and Orlando J. Rojas. "Cellulose nanocrystals: chemistry, self-assembly, and applications." *Chemical reviews* 110.6 (2010): 3479-3500.
48. Agrawal, Richa, et al. "Activation energy and crystallization kinetics of untreated and treated oil palm fibre reinforced phenol formaldehyde composites." *Materials Science and Engineering: A* 277.1 (2000): 77-82.
49. Kalia, Susheel, et al. "Cellulose-based bio-and nanocomposites: a review." *International Journal of Polymer Science* 2011 (2011).

50. Joseph, K., et al. "Natural fiber reinforced thermoplastic composites." *Natural polymers and agrofibers composites* 159 (2000).
51. Turbak, ALBIN F., FRED W. Snyder, and KAREN R. Sandberg. "Microfibrillated cellulose, a new cellulose product: properties, uses, and commercial potential." *J. Appl. Polym. Sci.: Appl. Polym. Symp.:(United States)*. Vol. 37. No. CONF-8205234-Vol. 2. ITT Rayonier Inc., Shelton, WA, 1983.
52. Fujisawa, Shuji, et al. "Preparation and characterization of TEMPO-oxidized cellulose nanofibril films with free carboxyl groups." *Carbohydrate Polymers* 84.1 (2011): 579-583.
53. Saito, Tsuguyuki, and Akira Isogai. "TEMPO-mediated oxidation of native cellulose. The effect of oxidation conditions on chemical and crystal structures of the water-insoluble fractions." *Biomacromolecules* 5.5 (2004): 1983-1989.
54. Montanari, Suzelei, et al. "Topochemistry of carboxylated cellulose nanocrystals resulting from TEMPO-mediated oxidation." *Macromolecules* 38.5 (2005): 1665-1671.
55. Saito, Tsuguyuki, et al. "Homogeneous suspensions of individualized microfibrils from TEMPO-catalyzed oxidation of native cellulose." *Biomacromolecules* 7.6 (2006): 1687-1691.
56. Saito, Tsuguyuki, et al. "Cellulose nanofibers prepared by TEMPO-mediated oxidation of native cellulose." *Biomacromolecules* 8.8 (2007): 2485-2491.
57. P. C. P. Watts, W.-K. Hsu, A. Barnes and B. Chambers, *Adv. Mater.*, 2003, **15**, 600–603
58. J. K. Yuan, S. H. Yao, Z. M. Dong, A. Sylvestre, M. Genestoux and J. Bai, Giant Dielectric Permittivity Nanocomposites: Realizing True Potential of Pristine Carbon

- Nanotubes in Polyvinylidene Fluoride Matrix through an Enhanced Interfacial Interaction, *J. Phys. Chem. C*, 2011, 115, 5515–5521
59. W. Ouyang, J. Sun, J. Memon, C. Wang, J. Geng and Y. Huang, Scalable preparation of three-dimensional porous structures of reduced graphene oxide/cellulose composites and their application in supercapacitors, *Carbon*, 2013, 62, 501–509
60. A. Kafy, K. K. Sadasivuni, H. Kim, A. Akther and J. Kim, *Phys. Chem. Chem. Phys.*, 2015, 17, 5923–5931
61. M. Mohiuddin, K. K. Sadasivuni, S. Mun and J. Kim, *RSC Adv.*, 2015, 5, 34432–34438.
62. K. K. Sadasivuni, A. Kafy, H.-C. Kim, H.-U. Ko, S. Mun and J. Kim, *Synth. Met.*, 2015, 206, 154–161
63. P. Lunkenheimer, V. Bobnar, A. V. Pronin, A. I. Ritus, A. A. Volkov and A. Loidl, *Phys. Rev. B*, 2002, 66, 052105
64. Weng, Zhe, et al. "Graphene–cellulose paper flexible supercapacitors." *Advanced Energy Materials* 1.5 (2011): 917-922.
65. Kang, Yan-Ru, et al. "Fabrication of electric papers of graphene nanosheet shelled cellulose fibres by dispersion and infiltration as flexible electrodes for energy storage." *Nanoscale* 4.10 (2012): 3248-3253.
66. Ouyang, Wenzhu, et al. "Scalable preparation of three-dimensional porous structures of reduced graphene oxide/cellulose composites and their application in supercapacitors." *Carbon* 62 (2013): 501-509.
67. Gao, Kezheng, et al. "Cellulose nanofiber–graphene all solid-state flexible supercapacitors." *Journal of Materials Chemistry A* 1.1 (2013): 63-67.

68. Zu, Guoqing, et al. "Nanocellulose-derived highly porous carbon aerogels for supercapacitors." *Carbon* 99 (2016): 203-211.
69. Wu, Xi-Lin, and An-Wu Xu. "Carbonaceous hydrogels and aerogels for supercapacitors." *Journal of Materials Chemistry A* 2.14 (2014): 4852-4864.
70. Stoller, Meryl D., et al. "Graphene-based ultracapacitors." *Nano letters* 8.10 (2008): 3498-3502.

Chapter 2

Materials and Methods

2.1 Introduction

This chapter provides the details about different materials, procedures and experimental details used for the different composite systems based on pristine and oxidized cellulose nanofibrils (CNF) with various graphene derivatives such as graphene oxide (GO), ammonia functionalized graphene oxide (NGO) and reduced graphene oxide (RGO). It contains the different fabrication methods for the fabrication and various techniques for characterization of prepared samples.

2.2 Materials

Cellulose nanofibrils (CNFs) were obtained from the University of Maine (U.S.A). The ammonia functionalized graphene oxide (NGO with concentration of 1 mg mL^{-1} ; Sigma no. 777013), natural graphite flakes, 2,2,6,6-tetramethylpiperidine-1-oxyl (TEMPO) reagent, conc. Sulfuric acid (H_2SO_4), Potassium permanganate (KMnO_4), sodium nitrate (NaNO_3), sodium bromide (NaBr), sodium hypochlorite (NaClO) solution, dimethyl sulfoxide (DMSO), ethanol (EtOH), and other chemicals were procured from Sigma-Aldrich and used as received.

2.3 Methods of fabrications

This part contains the various fabrication methods of various cellulose-graphene composites using pristine and oxidized CNF matrices and different graphene based fillers.

2.3.1 Fabrication of ammonia functionalized graphene oxide (NGO) filled pristine and oxidized cellulose nanofibrils (CNF) composites

The NGO/CNF and NGO/TCNF composite films were fabricated by a cost-effective solution-casting method. The NGO aqueous dispersion was mixed with 50 ml of 1.2 wt% of CNF and TCNF, respectively. Pure CNF and TCNF films without the addition of NGO were made as references. The solutions were mixed by the magnetic stirrer (Tehtnica Rotamix SHP-10) for 15 min, cast on to Petri dishes (120 x 17 mm), and dried at room temperature (23 ± 1 °C) for up to 4 days. The composite films of NGO with CNF were named as CNG-0.5, CNG-1, CNG-2, and CNG-3, while films prepared with TEMPO-mediated CNF (TCNF) as TCNG-0.5, TCNG-1, TCNG-2 and TCNG-3, respectively. The average thickness of CNG and TCNG composite films were in the range of $50\pm 2\mu\text{m}$ and $70\pm 2\mu\text{m}$ respectively.

2.3.2 Fabrication of graphene oxide (GO) filled pristine and oxidized cellulose nanofibrils (CNF) composites

The composite films were fabricated by mixing graphene oxide dispersion with CNF and TCNF followed by solution casting. The GO dispersions were prepared by mixing 200 mg of graphene oxide in 100 ml of deionized water and treated by ultrasonically for 1 hr to get homogeneous dispersion. The GO solutions having 0.003/0.006/0.0125/0.019 g were mixed with 50 ml of 1.2 wt% of CNF and TCNF, respectively using magnetic stirrer (Tehtnica Rotamix SHP-10) and cast on to Petri dishes for drying at room temperature. The fabricated films of GO with CNF were named as CGO-0.5, CGO-1, CGO-2, and CGO-3, whereas films of GO with TCNF as TCGO-0.5, TCGO-1, TCGO-2 and TCGO-3, respectively.

2.3.3 Fabrication of reduced graphene oxide (RGO) filled cellulose nanofibrils (CNF) as film like xerogels and cryogels

Various quantity of RGO (0.0003, 0.0008, 0.0013, 0.0025, 0.005, 0.0125 g) was mixed with 15 ml of DMSO using ultrasonic processor (CV 334) for 1 hour to obtain a stable solution. 20 ml of 1.2 wt% CNF solution were mixed with each of the RGO solutions by stirring for another 30 minutes to get homogeneous CNF-RGO (CRGO) dispersions. The resultant CRGO dispersions were vacuum filtered to remove DMSO and dried at room temperature to obtain film-like xerogel. The composite films were termed as CNF, CRGO-0.1, CRGO-0.3, CRGO-0.5, CRGO-1, CRGO-2 and CRGO-5. In parallel, the solvent-removed CRGO-5 water-dispersion was put into Teflon Petri dishes of 50 mm and placed on a temperature-controlled (by the software programme Supercool®) Cu-plate of a self-constructed cryo-unit with a temperature set to -50°C and -80°C , respectively, for about 3 hours to allow the cryogelation process and formation of the porous structure, followed by lyophilisation for 48 hours using a Christ Alpha 1-2 LD plus freeze-dryer to remove water.

2.4 Characterization techniques

2.4.1 Potentiometric titration

Potentiometric titration was used to quantify the contents of the carboxyl groups of the films by using a Mettler Toledo T70 with two-burette instrument, equipped with a combined glass electrode (Mettler TDG 117). The burettes were filled with 0.1 M HCl (Merck, Titrisol) and 0.1 M KOH (Baker, Dilut-it). Titration was carried out at room temperature ($23\pm 1^{\circ}\text{C}$) in forward and back runs between pH 2.5 and 11, within an inert (N_2 gas) atmosphere. The quantity of carboxylic groups was determined from the back-titration data.

2.4.2 Raman spectroscopy

Raman spectrum was recorded using a Horiba Jobin–Yvon LabRAM Micro-Raman spectrometer with Argon ion laser, with 514.5 nm as excitation wavelength to confirm the reduction of graphene oxide.

2.4.3 Attenuated Total Reflectance - Fourier Transform Infrared (ATR-FTIR)

Attenuated Total Reflectance - Fourier Transform Infrared (ATR-FTIR) spectroscopic analysis was performed to identify the spectral differences associated with the molecular structure of the films, as well as to identify the nature of their interaction. For that purpose, a Perkin–Elmer IR spectrophotometer was used with a Golden Gate Attenuated Total Reflection (ATR) attached to a diamond crystal. The spectra were accumulated under ambient conditions from obtaining 16 scans at resolutions of 4 cm^{-1} within a region of $4000\text{--}500\text{ cm}^{-1}$, with air spectrum subtraction performed in parallel as a background. The Spectrum 5.0.2 Software Programme was applied for the data acquisition analysis.

In the case of composites with NGO and GO, a linear baseline was subtracted, and the resulting (absorbance) spectra were normalised before performing the spectral deconvolution in the OH region ($3000\text{--}3700\text{ cm}^{-1}$) as well as the carbonyl region ($1500\text{--}1800\text{ cm}^{-1}$), only for GO based composites, followed by the Gaussian curve fitting procedure, being processed by using Peakfit 4.12 software (Galactic Industries Corporation, New Hampshire, USA). Band position and area were assessed and compared.

2.4.4 X-Ray diffraction (XRD) analysis

X-ray Diffraction (XRD) technique were employed to confirm the reduction of graphene oxide and to study the crystallinity of the composite films. The X-ray equatorial diffraction patterns of the composite films were obtained with an X-ray Diffractometer (Bruker Diffractometer D8

Advance Model) using Cu K α radiation ($\lambda= 0.1539$ nm) at the operating voltage and current of 40 KV and 40 mA, respectively, at room temperature (23 ± 1 °C) at a scan rate of 2° min^{-1} .

2.4.5 UV-Visible spectroscopy analysis

The transmittance curves of the NGO based composite films within the 250-750 nm wavebands were recorded using a Lambda 900 UV- Vis spectrophotometer (Perkin Elmer) with an integrated sphere of the scanning speed of 450 nm/min.

2.4.6 Contact angle and surface energy analysis

Film surface free energy and surface energy components were determined from Contact Angle (CA) measurements with four pure liquids of different polarities, namely water, formamide, diiodomethane, and glycerol. Contact Angle (CA) measurements of the NGO based films were performed using an SCA20 contact angle measurement system from Dataphysics (Germany). All measurements were conducted at room temperature on two independent surfaces with a test liquid volume of 3 mL. Each CA value was the average of at least eight drops of liquid per surface. The Surface Free Energy (SFE) of the films was calculated from the Contact Angle values of the test liquids by the van Oss and Good method [6-7]. The values of the surface tension and the components of the probe liquids used for CA measurements were taken from the Dataphysics database. The total SFE (γ_s^{TOT}) was calculated using the acid-base approach of van Oss and Good, which divides the total SFE into the dispersive Lifshitz–van der Waals interaction (γ_s^{LW}) and the polar Lewis acid–base interactions (γ_s^{AB}) according to the following Equations:

$$\gamma_s^{\text{TOT}} = \gamma_s^{\text{LW}} + \gamma_s^{\text{AB}} \quad (1)$$

$$\gamma_s^{\text{AB}} = 2 \sqrt{(\gamma_s^+ \gamma_s^-)} \quad (2)$$

Where the Lewis acid–base interactions are subdivided into electron donor γ_s^- (Lewis base) and electron acceptor γ_s^+ (Lewis acid) parts.

2.4.7 Transmission Electron Microscopy (TEM)

Transmission Electron Microscope (JEOL JEM 2100) was used for the structural and morphological analysis of graphene oxide and reduced graphene oxide powders by drop-casting on carbon-coated copper grids.

2.4.8 Scanning Electron Microscopy (SEM)

For NGO and GO composites, a field emission scanning electron microscope (FESEM) imaging system was performed using the Ultra + (Zeiss, Germany) microscope to study the morphology. The samples were coated with a platinum layer using an ion sputter PECS - Precision Etching Coating System, Model 682 (Gatan US). Surface characterization and quantification of the films was performed with an ImageJ plugin for surface assessment, denominated by the SurfCharJ plugin.

For RGO based xerogels and cryogels, Scanning Electron Microscope (SEM) imaging was performed using a JEOL JSM 6460 LV scanning electron microscope. The samples were coated with a thin layer of gold by sputtering using EDWARDS scan-coat on the surface and the cross-sections. The surface characterization and quantification of the pore structure was performed with an ImageJ software.

2.4.9 Tensile strength analysis

The tensile strength at maximum (MPa) and the tensile strain at break (%) of the samples was measured using a Shimadzu AGS-X electromechanical universal testing machine. For the

testing, the samples were cut into a size of 1 cm x 5 cm and mounted vertically with two clamps at 2.5 cm distance and tested at a speed of 1 mm/min with a 5 kN load cell.

2.4.10 Dynamic mechanical analysis (DMA)

Dynamic mechanical analysis of UV treated and untreated composite samples were performed with a Perkin Elmer DMA 8000 using rectangular shaped samples (5 x 2.5 x 0.55 mm³) at the heating rate of 4 ° C / min up to 250 ° C with a frequency of 10 Hz.

2.4.11 Thermal Gravimetric Analysis (TGA)

Thermal Gravimetric Analysis (TGA) of pristine and NGO incorporated composites were performed by using a STAR Thermogravimetric System, Mettler Toledo under nitrogen purge with a flow rate of 100 mL/min. The scanning rate was 10°C/min and the temperature range was from 100 to 800°C.

2.4.12 Dielectric studies

For dielectric measurements, film samples were sputtered by Cr/Au electrodes with 0.4 mm diameter (RF magnetron sputtering, 5 Pa). The capacitance C and conductivity G were measured by a Novocontrol Alpha High-Resolution Dielectric Analyzer (Novocontrol Technologies GmbH, Hundsangen, Germany) in a frequency range of 1 kHz to 10 MHz with the amplitude of the probing ac electric signal of 50 mV. Then, the real part of the complex dielectric constant, i.e., the dielectric permittivity ϵ' and the real part of the ac electrical conductivity σ' were calculated via $\epsilon' = (Cd)/(\epsilon_0 S)$ and $\sigma' = Gd/S$, where S and d were the areas of the electrode and thickness of the film, respectively, and ϵ_0 is the dielectric constant of free space.

2.4.13 Cyclic voltammetry (CV) analysis

Cyclic voltammetry (CV) measurements were performed using a PGSTAT101 controlled by an Autolab Nova Software version 1.8. All experiments were carried out in a 100 mL Metrohm cell using fabricated film samples as working electrode. A counter (Pt) electrode with an Ag/AgCl saturated reference electrode (Metrohm) was used throughout. The electrochemical measurements were performed in a 1M H₂SO₄ of 50 ml solution serving as the electrolyte. The voltammetric curves were recorded at a scan rate from 5 to 100 mV/s. The specific capacitance of the electrodes has been calculated according to the following equation:

$$C = \frac{1}{m v k} \int_{V^-}^{V^+} I dV \quad (3)$$

where C is the specific capacitance (F/g), m is the mass (g) of the active electrode, V is the potential difference, and k is the scan rate (m V/s).

2.4.14 Electrochemical impedance spectroscopy (EIS)

Impedance measurements were performed with a Gamry 600™ potentiostat/galvanostat by using 4 cm² of film samples as the working electrode. Experiments were performed in a three-electrode glass cell (volume 1 L) closed to the air under stagnant conditions at 25 °C, using 1 M H₂SO₄ solution as the electrolyte. A saturated calomel electrode (i.e. SCE, 0.2444 V vs. SHE) was used as the reference electrode and a Pt mesh as the counter electrode. Spectra were obtained in the frequency range from 0.01 Hz to 0.1 MHz, with 10 points per decade and 5 mV (peak to peak) amplitude of the excitation signal. For xerogels and cryogels, the impedance spectra were obtained after 10, 20, 30, 40, 50, and 60 min of immersion and the frequency range from 50 mHz to 0.1 MHz was used with 10 points per decade and a 5 mV (peak to peak) amplitude of the excitation signal.

2.5 Conclusions

This chapter has given an insight to all the characterization techniques, experimental details, different studies for various composites used in this thesis.

2.6 References

1. Saito, Tsuguyuki, et al. "Cellulose nanofibers prepared by TEMPO-mediated oxidation of native cellulose." *Biomacromolecules* 8.8 (2007): 2485-2491
2. Fukuzumi, Hayaka, et al. "Transparent and high gas barrier films of cellulose nanofibers prepared by TEMPO-mediated oxidation." *Biomacromolecules* 10.1 (2008): 162-165.
3. Saito, Tsuguyuki, et al. "Homogeneous suspensions of individualized microfibrils from TEMPO-catalyzed oxidation of native cellulose." *Biomacromolecules* 7.6 (2006): 1687-1691
4. Hummers Jr, William S., and Richard E. Offeman. "Preparation of graphitic oxide." *Journal of the American Chemical Society* 80.6 (1958): 1339-1339.
5. Marcano, Daniela C., et al. "Improved synthesis of graphene oxide." *ACS nano* 4.8 (2010): 4806-4814.
6. Tadros, T. "Interfacial forces in aqueous media, Carel J. van Oss, Marcel Dekker Inc., New York, 1994, viii+ 440 pp., price US \$165.00. ISBN 0 8247 9168 1." (1995): 311-311.
7. Van Oss, Carel J., Manoj K. Chaudhury, and Robert J. Good. "Interfacial Lifshitz-van der Waals and polar interactions in macroscopic systems." *Chem. Rev* 88.6 (1988): 927-941.

Chapter 3

Oxidization of pristine CNF using TEMPO reagent and synthesis, reduction and characterization of graphene oxide (GO)

3.1 Introduction

This chapter provides the details about the oxidization of pristine cellulose nanofibrils (CNF) by TEMPO reagent and their characterization. It also includes the UV induced reduction of graphene oxide incorporated pristine and oxidized cellulose nanofibrils (CNF) composites. The thermal reduction of graphene oxide and the characterization also describes in this chapter.

3.2 Oxidization of pristine CNF using TEMPO reagent

TEMPO-mediated oxidation of CNF was performed based on the previously reported methods [1-3]. For that purpose, the oxidation solution was prepared by dissolving 0.01475 g of TEMPO and 0.162 g NaBr in distilled water and added to 1 wt% of CNF dispersion. The NaClO solution (25 ml, 10%) was added slowly to this slurry and stirred at room temperature, and the pH of the solution was adjusted to be 10 and kept constant for 3 h by using 0.1 M HCl and 0.1 M NaOH. After stirring for the designated time the oxidation was quenched by adding 7 mL of EtOH. The oxidized cellulose was washed thoroughly with water and weighed to measure the mass recovery ratios. The TEMPO oxidized CNF was named as TCNF.

3.3 Characterization of pristine and oxidized CNF

3.3.1 Potentiometric titration analysis

Potentiometric titration analysis was used to calculate the carboxylate content of fabricated pristine and oxidized CNF films. The titration graphs are shown in Fig. 3.1. The carboxylate content increased from $0.3 \pm 0.15 \text{ mmol g}^{-1}$ for pristine CNF, to $1.63 \pm 0.21 \text{ mmol g}^{-1}$ for the oxidized CNF. The increased amount of carboxyl groups proves the oxidation using TEMPO reagent.

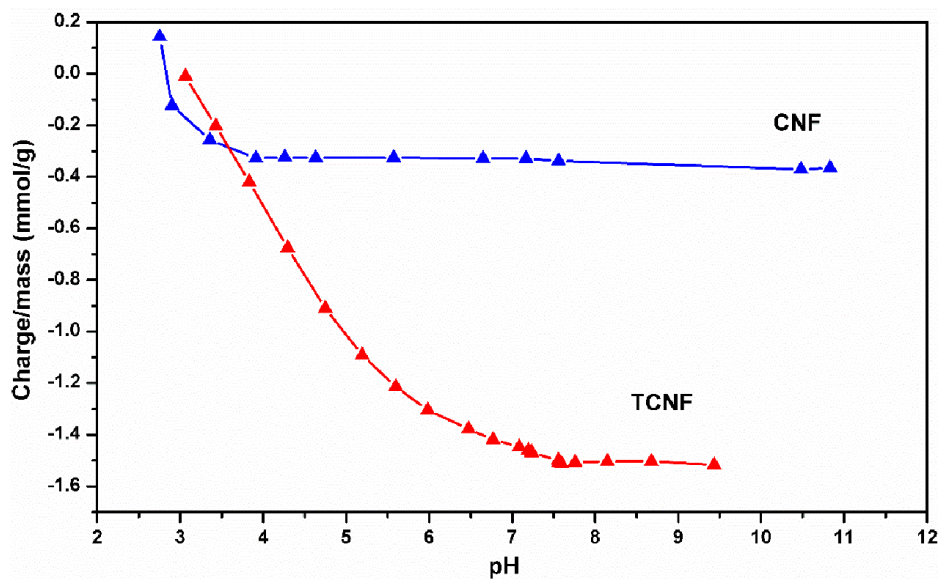


Fig. 3.1 Potentiometric titration of pristine CNF and TEMPO oxidized CNF (TCNF)

3.3.2 ATR-FTIR analysis

The ATR-FTIR spectra of pristine CNF and TEMPO oxidized CNF (TCNF) are presented in Fig. 3.2. The typical cellulose-related IR bands at $\sim 3333\text{-}3335 \text{ cm}^{-1}$, $\sim 2900\text{-}2923 \text{ cm}^{-1}$, $\sim 1318 \text{ cm}^{-1}$, $\sim 1160 \text{ cm}^{-1}$, $\sim 1023 \text{ cm}^{-1}$, $\sim 1028 \text{ cm}^{-1}$ were identified within both CNF and TCNF spectral lines, while the bands at $\sim 1596 \text{ cm}^{-1}$ and $\sim 1739 \text{ cm}^{-1}$ were associated with C=O stretching vibration in carboxylic (COO^-) and its protonated (COOH) form, respectively, identified within the TCNF spectra only. Moreover, the vibration peaks at $\sim 1318 \text{ cm}^{-1}$ indicate the presence of bending vibration of C-H bonds in the cellulose glucose rings, while the peak at $\sim 1023\text{-}1028 \text{ cm}^{-1}$ is characteristic for the anhydrous group' C-O stretching vibration.

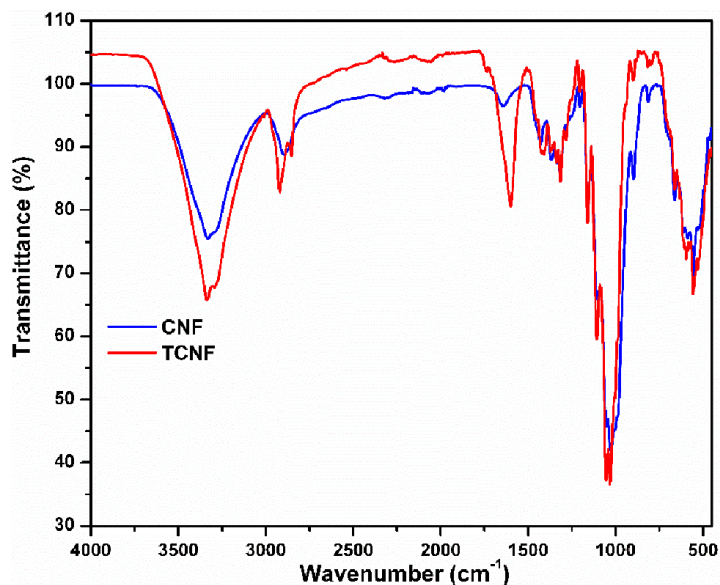


Fig. 3.2 ATR-FTIR spectra for CNF and TEMPO oxidized CNF (TCNF)

3.3.3 XRD studies

The XRD patterns of CNF and TCNF films are shown in Fig. 3.3. The X-ray diffraction patterns of both pristine and TEMPO-oxidized celluloses were similar unless their intensity and were of typical cellulose I allomorph. In the case of CNF and TCNF, two characteristic peaks centred at around 15.5° and 22.8° are observed, corresponding to the planes (1 0 1), and (0 0 2), a typical profile of cellulose I allomorph [4]. The broad diffraction peak at 15.5° indicates the partly crystalline nature of the cellulose.

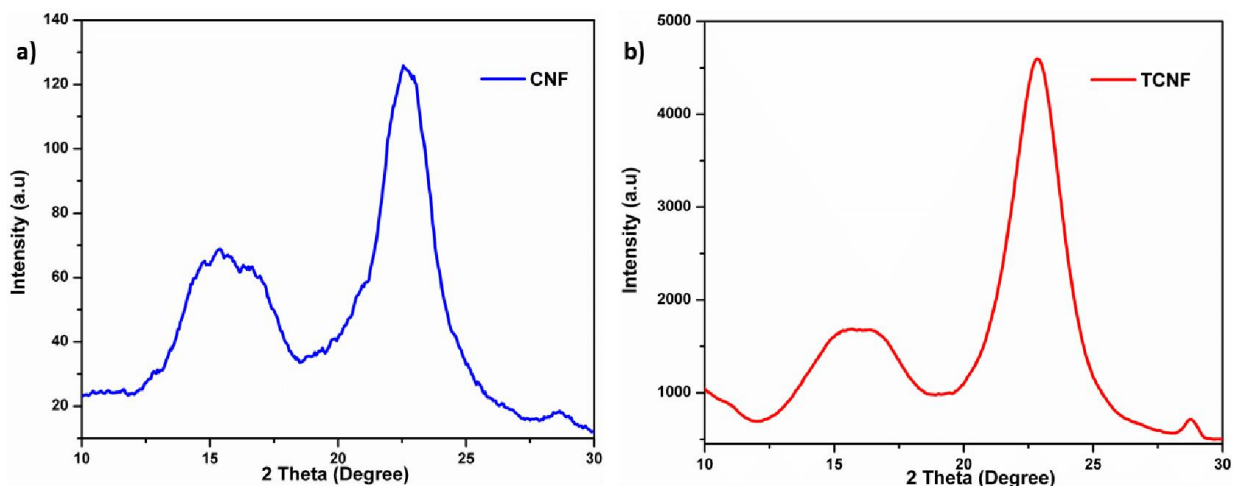


Fig. 3.3 XRD patterns of (a) CNF and (b) TEMPO oxidized CNF (TCNF)

3.3.4 UV-Visible spectroscopy analysis

The UV-visible spectra for pristine and TEMPO oxidized CNF films were measured in the wavelengths region of 250-750 nm as shown in Fig. 3.4. The spectrum of CNF exhibits the highest transmittance (~90 %) compared to the TCNF film (~83%) in the visible light range (400-800), which may be credited to the presence of the large amount of carboxyl functional groups in TCNF as compared to the CNF matrix.

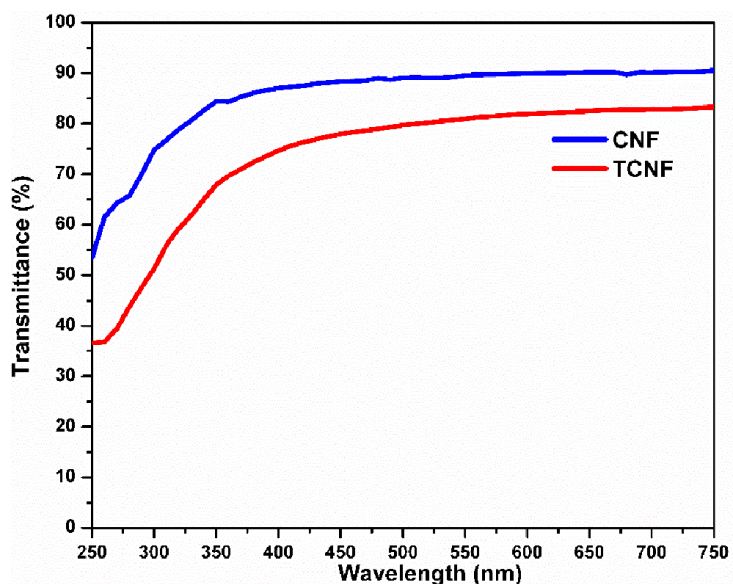


Fig. 3.4 UV-visible spectra of CNF and TEMPO oxidized CNF (TCNF)

3.3.5 Scanning Electron Microscopy (SEM) studies

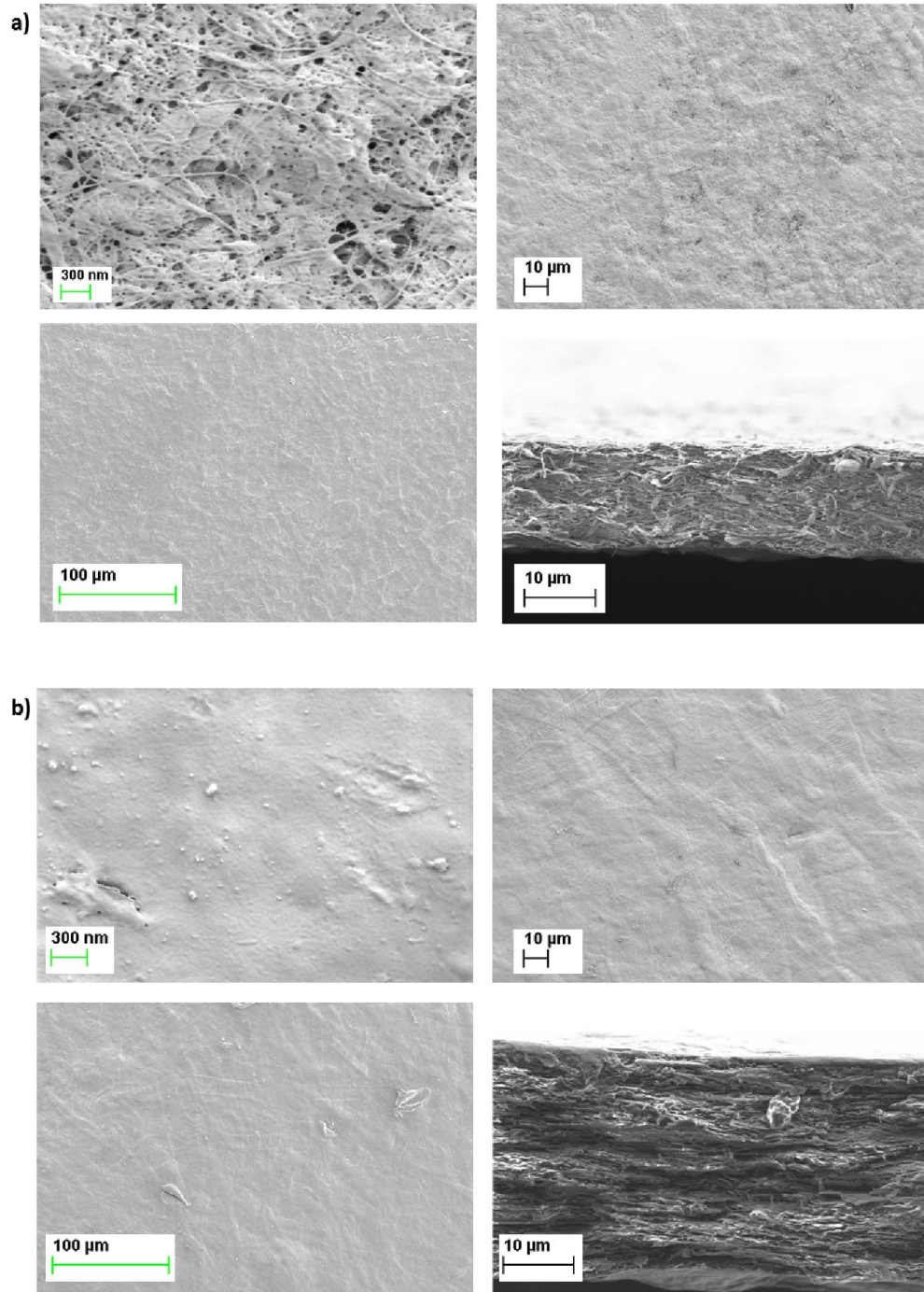


Fig. 3.5 FE-SEM images of (a) CNF and (b) TEMPO oxidized CNF (TCNF)

The SEM analysis of the film surfaces and cross-sections were performed to investigate the morphology of both pristine and oxidized CNF films. As shown on Fig. 3.5 (a), the diameter of pristine cellulose fibrils is in nanometer regime which has in a form of agglomerated fibrous networks. The pristine CNF has quite smooth morphology than oxidized films. The cross-sectional images give the horizontal stacking geometry of fibres and reveal more dense and compact network structure of oxidized films than pristine CNF films. These observations may due to the interfacial interaction that restrains the CNF chains and forms chain bridging between individual fibres.

3.4 Synthesis of graphene oxide

Graphene oxide (GO) was prepared by Hummers method [5-6]. Concentrated H₂SO₄ (24 mL) was added to a mixture of 1 g of graphite flakes and 0.5 g of NaNO₃ chilled to 0 °C using an ice bath. 3 g of KMnO₄ were added slowly under controlled reaction temperature below 20 °C. The mixture could warm at 35 °C and stirred for 1.5 hours and after that 46 mL of warm water were added slowly. Then the solution temperature raised to 98°C and diluted with 132 ml of warm water after 15 minutes, and treated with 3% of H₂O₂. After multiple washing, centrifugation, and drying of resulting suspension, a solid yellow-brown powder was obtained.

3.5 Characterization of synthesized graphene oxide

3.5.1 Transmission Electron Microscopy (TEM) studies

The surface morphology of GO was confirmed by TEM (Fig 3.6). Generally, graphene oxide shows a tendency to assemble and form multilayer sheets including wrinkles [7]. The amorphous nature of graphene oxide was elucidated by high-resolution TEM images as shown in fig 3.6b. The selected area electron diffraction (SAED) image of

graphene oxide from the monolayer region of GO shown in the inset of Fig 1b also confirms its amorphous character. Most of the earlier studies reported sharp and bright diffraction spots of graphene oxide by SAED [7-8]. The clear diffraction spots having the six-fold pattern are an indication of the hexagonal lattice [9].

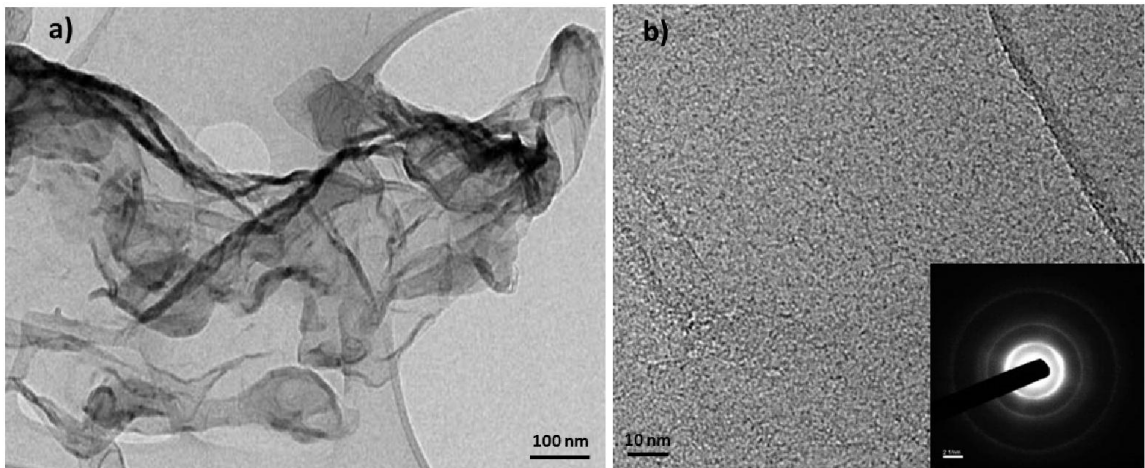


Fig. 3.6 (a) TEM (b) high-resolution TEM images of graphene oxide with inset SAED pattern.

3.5.2 XRD analysis

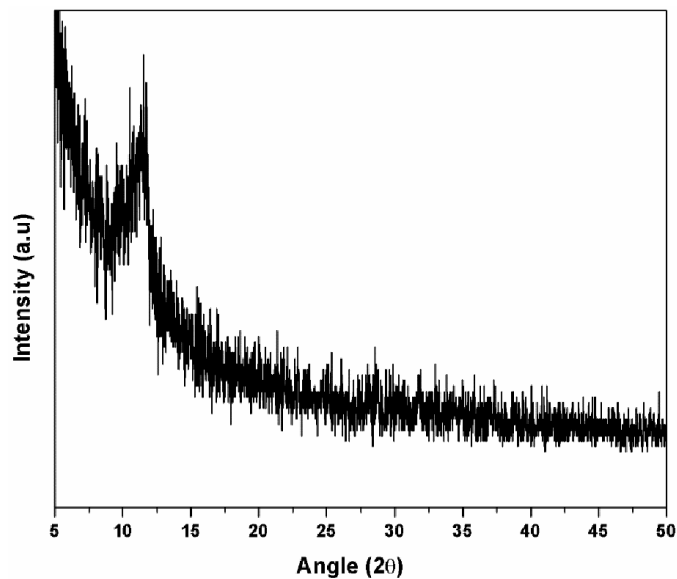


Fig. 3.7 X-ray diffraction pattern of graphene oxide

The XRD pattern of GO shown in fig. 3.7 having a broad diffraction peak corresponds to $2\theta = 10.5^\circ$. The broad and less clear peak confirms an extensive range of interlayer spacing and a considerable amount of exfoliated sheets [10].

3.5.3 Raman spectroscopy

Fig 3.8 shows the micro-Raman spectrum of GO in the region 1200-1700 cm^{-1} . GO shows a broad D band at 1335 cm^{-1} and G band at 1590 cm^{-1} . The broadened G band and D band indicate the severe disruption of sp^2 carbon lattice which is in good agreement with previous investigations of GO [8].

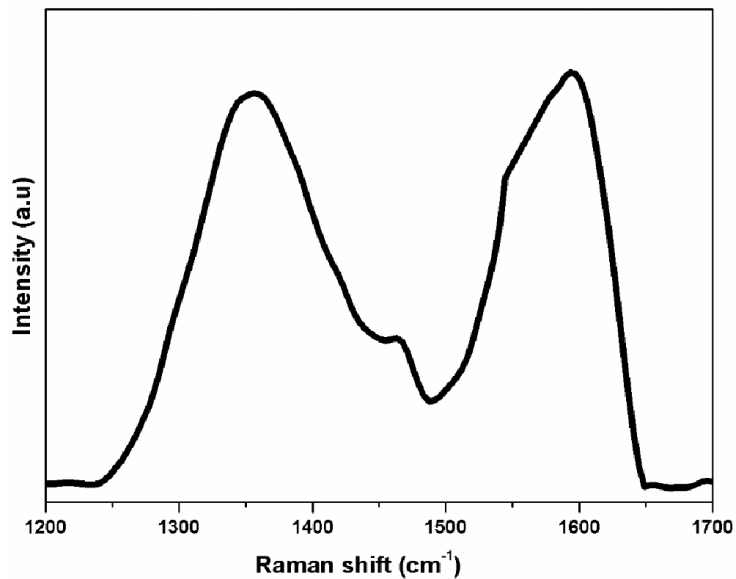


Fig. 3.8 Raman spectrum of graphene oxide

3.5.4 ATR-FTIR analysis

The FTIR spectrum of GO (fig. 3.9) shows a broad absorption peak at 3222 cm^{-1} which is related to -OH stretching and typical carbonyl and carboxyl absorption bands are observed at 1625 cm^{-1} and 1732 cm^{-1} .

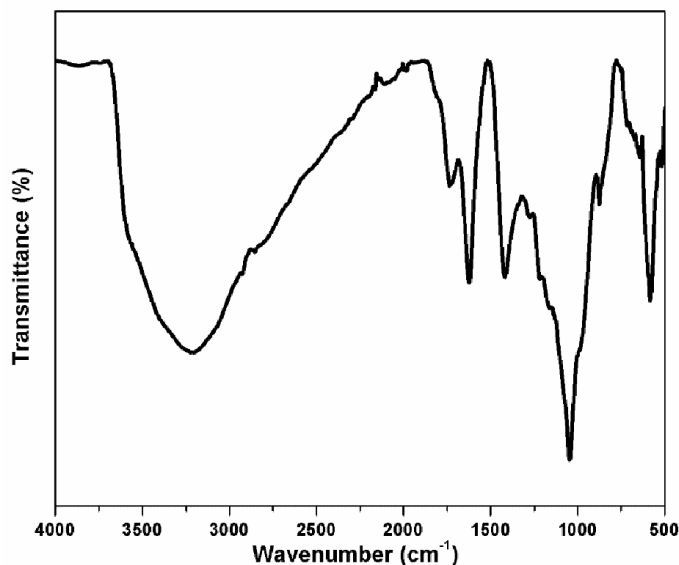


Fig. 3.9 ATR-FTIR spectrum of graphene oxide

3.6 UV induced reduction of graphene oxide (GO) filled pristine and oxidized CNF composites

3.6.1 UV irradiation experiment

The UV irradiation experiments were performed by using Novascan Digital UV ozone system (USA) in presence of nitrogen atmosphere as shown in fig 3. 10. The distance between the UV lamp and the samples has been fixed as 10 cm. The UV-chamber has a mercury lamp as a light source with a power of 300 W. The GO incorporated CNF and TCNF samples were systematically UV irradiated for different time intervals of 15 minute, 30 minute, 1 h, 2 h and 5 h to check the ability of treatment effects.

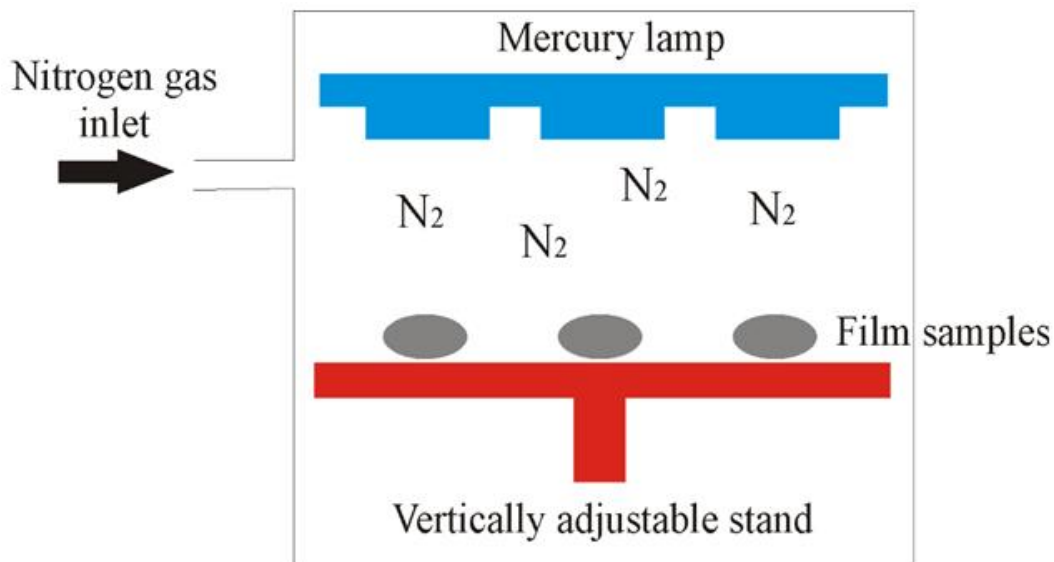


Fig. 3.10 Experimental set up for UV irradiation experiment

3.9 Thermal reduction of graphene oxide (GO)

The thermally reduced graphene oxide (RGO) was obtained by heating the GO powder at 400 C for 10 minutes.

3.10 Characterization of thermally reduced graphene oxide (RGO)

3.10.1 Transmission Electron Microscopy (TEM) studies

TEM images clearly confirm the exfoliation of GO sheets after thermal treatment. The reduced GO (RGO) sheets are randomly aggregated and closely connected with each other with an average width of less than 2 nm (Fig. 3.b).

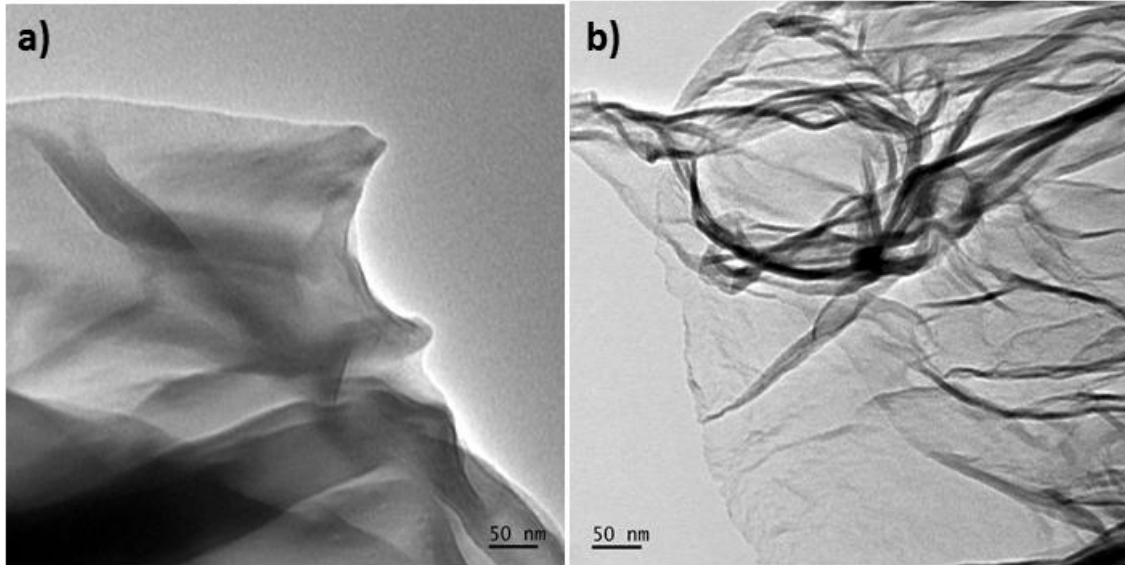


Fig. 3.11 TEM images of (a) graphene oxide and (b) thermally reduced graphene oxide.

3.10.2 XRD analysis

The observed wide peak at 2θ of 10.5° for GO in XRD pattern (Fig. 2c) may be because of the presence of trapped water molecules between the graphitic sheets and by the oxygen-rich species on both sheets surfaces [11]. The disappearance of this peak for RGO confirms the formation of single layers of graphene after thermal reduction.

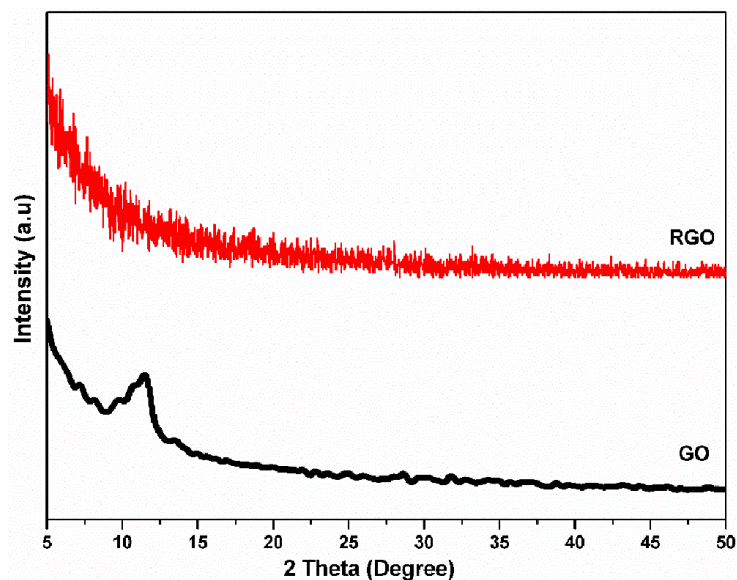


Fig. 3.12 X-ray diffraction pattern of graphene oxide and thermally reduced graphene oxide

3.10.3 Raman spectroscopy

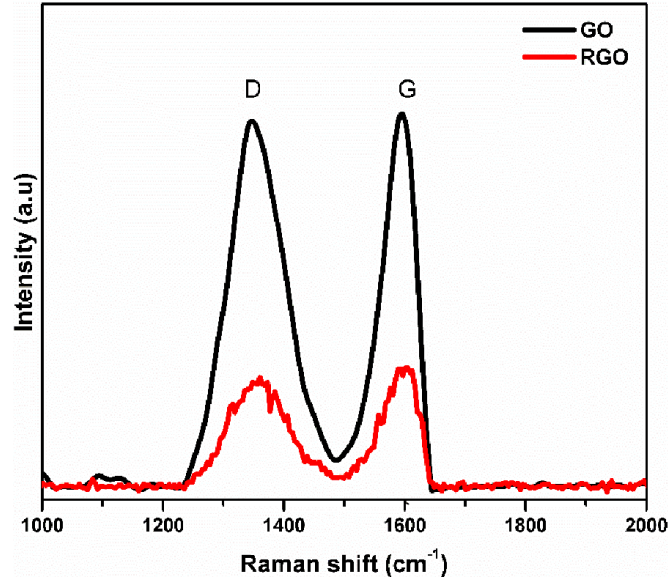


Fig. 3.13 Raman spectra of graphene oxide and thermally reduced graphene oxide

The prominent D and G Raman peaks at about 1342 cm^{-1} and 1591 cm^{-1} , respectively, (Fig. 2d) of GO clearly indicates the attachment of functional groups such as epoxides and hydroxyls on the carbon basal plane of graphene sheets which leads to structural inadequacies compared to RGO [12]

3.10.4 ATR- FTIR analysis

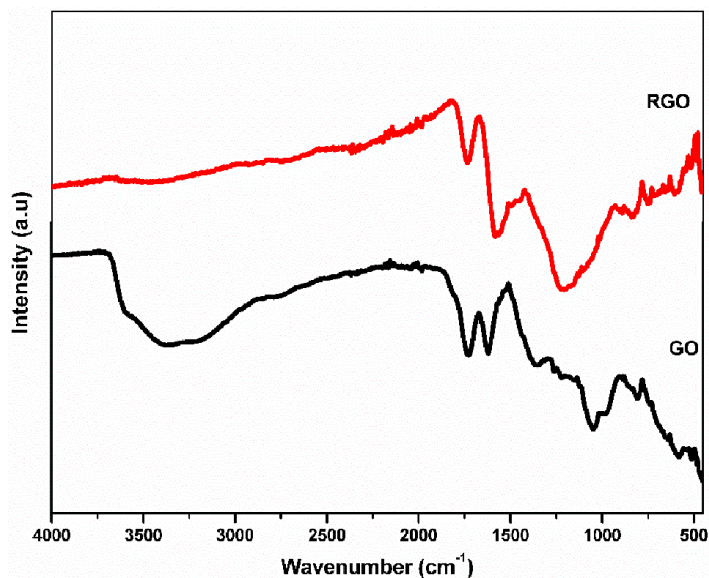


Fig. 3.14 ATR FTIR spectra of graphene oxide and thermally reduced graphene oxide

The broad absorption peak at about 3405 cm^{-1} for GO in FTIR spectra (Fig. 2e) is connected to -OH stretching of water molecules which almost disappeared in the case of RGO due to its removal after thermal treatment. The intensities of the stretching vibration peaks of C=O at about 1725 cm^{-1} , C-O of epoxy at about 1220 cm^{-1} and C-O of alkoxy at about 1058 cm^{-1} are decreased or disappeared obviously for RGO sample in comparison with GO [13].

3.11 Conclusion

This chapter has given the complete details about the synthesis and characterization of materials used for the composite preparation. After the oxidation of cellulose nanofibrils (CNF) using TEMPO reagent, the carboxylate content increased from $0.3 \pm 0.15\text{ mmol g}^{-1}$ for pristine CNF, to $1.63 \pm 0.21\text{ mmol g}^{-1}$ for the oxidized CNF. The pristine and oxidized CNF has been characterized by ATR-FTIR spectroscopy analysis, XRD studies, UV-Visible spectroscopy and SEM analysis. The graphene oxide is synthesised and characterized by using TEM analysis, XRD

studies, Raman spectroscopy and ATR-FTIR spectroscopy analysis. The UV induced reduction procedure of composites and the thermal reduction of graphene oxide have been explained and characterized by using TEM analysis, XRD studies, Raman spectroscopy and ATR-FTIR spectroscopy analysis.

References

1. Fukuzumi, Hayaka, et al. "Transparent and high gas barrier films of cellulose nanofibers prepared by TEMPO-mediated oxidation." *Biomacromolecules* 10.1 (2008): 162-165.
2. Saito, Tsuguyuki, et al. "Cellulose nanofibers prepared by TEMPO-mediated oxidation of native cellulose." *Biomacromolecules* 8.8 (2007): 2485-2491.
3. Saito, Tsuguyuki, et al. "Homogeneous suspensions of individualized microfibrils from TEMPO-catalyzed oxidation of native cellulose." *Biomacromolecules* 7.6 (2006): 1687-1691.
4. Kabiri, Roya, and Hassan Namazi. "Nanocrystalline cellulose acetate (NCCA)/graphene oxide (GO) nanocomposites with enhanced mechanical properties and barrier against water vapor." *Cellulose* 21.5 (2014): 3527-3539.
5. Hummers Jr, William S., and Richard E. Offeman. "Preparation of graphitic oxide." *Journal of the American Chemical Society* 80.6 (1958): 1339-1339.
6. Marcano, Daniela C., et al. "Improved synthesis of graphene oxide." *ACS nano* 4.8 (2010): 4806-4814.D
7. G. Wang, B. Wang, J. Park, J. Yang, X. Shen and J. Yao, *Carbon N. Y.*, 2009, **47**, 68–72
8. N. R. Wilson, P. A. Pandey, R. Beanland, R. J. Young, I. A. Kinloch, L. Gong, Z. Liu, K. Suenaga, J. P. Rourke, S. J. York and J. Sloan, *ACS Nano*, 2009, **3**, 2547–2556.
9. K. Krishnamoorthy, M. Veerapandian, K. Yun and S. J. Kim, *Carbon N. Y.*, 2013, **53**, 38–49
10. Littlejohn, Samuel, et al. "Pressure Sensing and Electronic Amplification with Functionalized Graphite–Silicone Composite." *Advanced Functional Materials* 23.43 (2013): 5398-5402.

11. Bourlinos, Athanasios B., et al. "Graphite oxide: chemical reduction to graphite and surface modification with primary aliphatic amines and amino acids." *Langmuir* 19.15 (2003): 6050-6055.
12. Pimenta, M. A., et al. "Studying disorder in graphite-based systems by Raman spectroscopy." *Physical chemistry chemical physics* 9.11 (2007): 1276-1290.
13. Peng, Hongdan, et al. "Simultaneous reduction and surface functionalization of graphene oxide by natural cellulose with the assistance of the ionic liquid." *The Journal of Physical Chemistry C* 116.30 (2012): 16294-16299.

Chapter 4

Structure, morphology, mechanical, dielectric and electrochemical storage properties of ammonia functionalized graphene oxide (NGO) filled pristine and oxidized cellulose nanofibrils (CNF) composites

4.1 Summary

Cellulose materials have become widely interesting recently in scientific and industrial fields as a promising sustainable substrate for its versatile usage also in flexible energy storage devices [1], transistors [2], sensors [3], supercapacitors [4] etc. Currently, the main strategy in the fabrication of these types of materials with improved dielectric performance is focused on using nano-additives, such as carbon nanotubes and graphene or graphene oxide (GO) nanosheets, due to their ultra-high specific surface area ($\sim 2630 \text{ m}^2/\text{g}$) and excellent electric properties [5]. However, matrices with a high dielectric constant are crucial for the energy storage materials which, in the case of cellulose based materials, depend primarily on the cellulose fiber size and porous structure, as indicated by the material free space [6]. The cellulose/graphene-based nanocomposites with high mechanical and thermal properties are therefore reported as flexible energy storage materials for electronic applications [3,7].

GO possesses a planar construction with abundant oxygen containing functional groups (epoxy, hydroxyl and carboxyl) on both basal planes and edges [8,9] and aromatic sp^2 domains that give it excellent dispersibility in a polymer matrix by generating interfacial bonding [10–12].

As such, GO has become an effective functional filler in the cellulose matrix [13]. The presence of many hydroxyl groups of cellulose along the GO skeleton causes the formation of comprehensive networks of intra- and inter-molecular hydrogen bonds with the cellulose, thus forming the two-crystalline and amorphous structural regions in the same polymer. When the polar fillers are uniformly bonded with the neat cellulose, flexible materials are formed. However, the facile aggregation of graphene during synthesis may reduce the material's performance. The low conductivity of GO does not allow for the formation of electronic devices; therefore, reduced GO is largely used for these purposes. Both effects can be minimized by modifying the GO sheets with the proper functional groups, to maintain strong interactions with the cellulose matrix [5,6] as well as to increase the dielectric performances. However, most of the previously reported improvements in dielectric responses for the cellulose/graphene composites [6,14,15] have been focused on the lower frequency regions of the dielectric permittivity of the materials, expressed mainly in the surface layers.

In this chapter, the wood-based cellulose nanofibrils (CNF) and TEMPO oxidized CNFs (TCNF) with ammonia functionalized GO (NGO) were used as highly electroconductive nano fillers, to fabricate flexible energy storage materials. The surface structural, mechanical, thermal, transparency and dielectric properties of the composite films were investigated by analyzing the interactions of the NGO within both cellulosic matrices using ATR-FTIR and XRD spectroscopy; analyzing the morphology/topography and surface properties using SEM and contact angle measurements; evaluating the transmittance, tensile strength/stress and TGA; assessing the dielectric constant and ac conductivity at higher frequency regions, as well as the electrochemical energy storage capacity by cyclic voltammetry and electrochemical impedance studies. The morphology–property correlation was established to provide the real intrinsic properties.

4.2 Structural and morphological properties

The structure and morphology of the nanocomposite films were studied to explain their functional properties. The structural composition was identified by using FTIR and XRD spectroscopic techniques. The ATR-FTIR spectra of differently fabricated samples are presented in Fig. 2.1. The NGO shows O–H stretching (broad-coupling hydroxyl group) at $\sim 3230\text{ cm}^{-1}$, C=O stretching at $\sim 1725\text{ cm}^{-1}$, C–O alkoxy at ~ 1376 , and C–O epoxy at $\sim 1049\text{ cm}^{-1}$. Additionally, two peaks were observed at $\sim 1586\text{ cm}^{-1}$ and $\sim 1224\text{ cm}^{-1}$, which attributes to the N-H bend and C-N stretching, respectively. The typical cellulose-related IR bands at $\sim 3333\text{-}3335\text{ cm}^{-1}$, $\sim 2900\text{-}2923\text{ cm}^{-1}$, $\sim 1318\text{ cm}^{-1}$, $\sim 1160\text{ cm}^{-1}$, $\sim 1023\text{ cm}^{-1}$, $\sim 1028\text{ cm}^{-1}$ were identified within both CNF and TCNF spectral lines, while the bands at $\sim 1596\text{ cm}^{-1}$ and $\sim 1739\text{ cm}^{-1}$ were associated with C=O stretching vibration in carboxylic (COO^-) and its protonated (COOH) form, respectively, identified within the TCNF spectra only. Moreover, the vibration peaks at $\sim 1318\text{ cm}^{-1}$ indicate the presence of bending vibration of C-H bonds in the cellulose glucose rings, while the peak at $\sim 1023\text{-}1028\text{ cm}^{-1}$ is characteristic for the anhydrous group' C-O stretching vibration. In the spectral lines of NGO-embedded CNF/TCNF films, the appearance of relatively weak, yet NGO concentration-dependent vibration lines at $\sim 2918\text{ cm}^{-1}$, $\sim 1742\text{ cm}^{-1}$ and $\sim 1542\text{ cm}^{-1}$, confirm the NGO presence within the composite films, while shifting of their position implies their interaction pattern with cellulose.

A closer look at the de-convoluted spectral lines in the region between $3000\text{-}3700\text{ cm}^{-1}$ (Fig. 2.2), revealed the presence of six hidden peaks, related to particular inter- and intra-molecular vibrations of OH groups in the C-2, C-3 and C-6 position within the glucose ring [16], i.e. 1st to

the O---H stretching, 2nd and 3rd to the inter-molecular hydrogen bond of O(6)H---O, 4th and 5th to the intra-molecular hydrogen bond of O(3)H---O, and 6th to the intra-molecular hydrogen bond of O(2)H---O. Observed, also supported from calculated data (inserted Table in Fig. 2.2), was the dominant presence of intra-molecular-bonding after addition of NGO, dominating in the TCNF mixture (related to the peaks' total area) over the composite with CNF, while inter-molecular bonding remained almost un-changed in both cases. These may imply an interruption of amorphous cellulosic parts by the NGO and possible inter-penetration, which allowed very close contact among the components, also bringing the mechanical strengthening and dielectric enhancements.

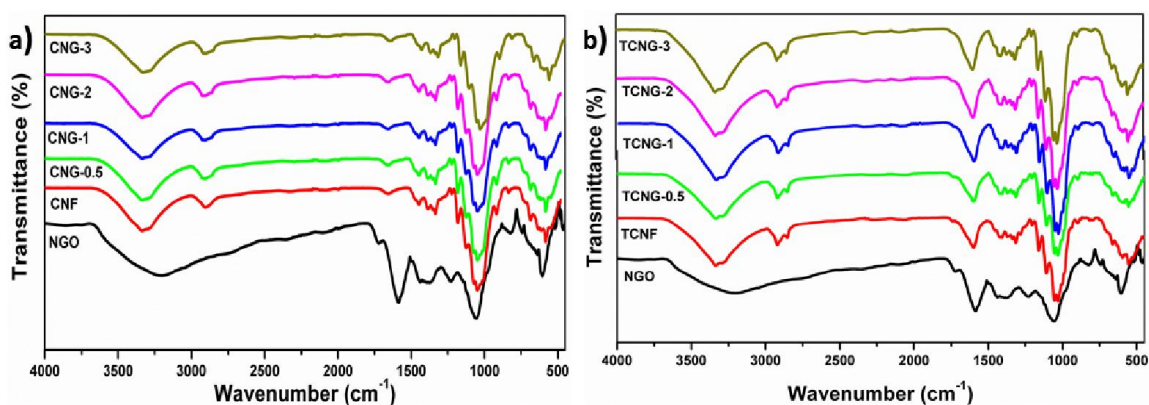


Fig 4.1. FTIR spectra of (a) CNG and (b) TCNG composites.

The involvement of NGO's amino (-NH₂) surface groups in H-bonding with OH and carboxylic groups of TCNF is demonstrated by the N-H bend shifting from ~1586 cm⁻¹ to ~1637 cm⁻¹ and by the appearance of three additional bends in these regions as illustrated in the inserted de-convoluted spectra lines in the region between 1500-1700 cm⁻¹ as well as presented in Scheme 1. In the TCNG composites, the C=O stretching vibration peak at ~1596 cm⁻¹ is more intense due to the merging with the N-H bend of NGO at ~1586 cm⁻¹. The NGO made the interaction with

both CNF and TCNF owing to hydrogen bonding between the carboxyl and OH groups of the NGO and the carbonyl groups of the cellulose matrix. When GO is added into the cellulose matrix, a hydrogen bond occurs between the carbonyl groups of GO and OH groups of cellulose which resulted in an enhanced interaction as confirmed by the SEM studies.

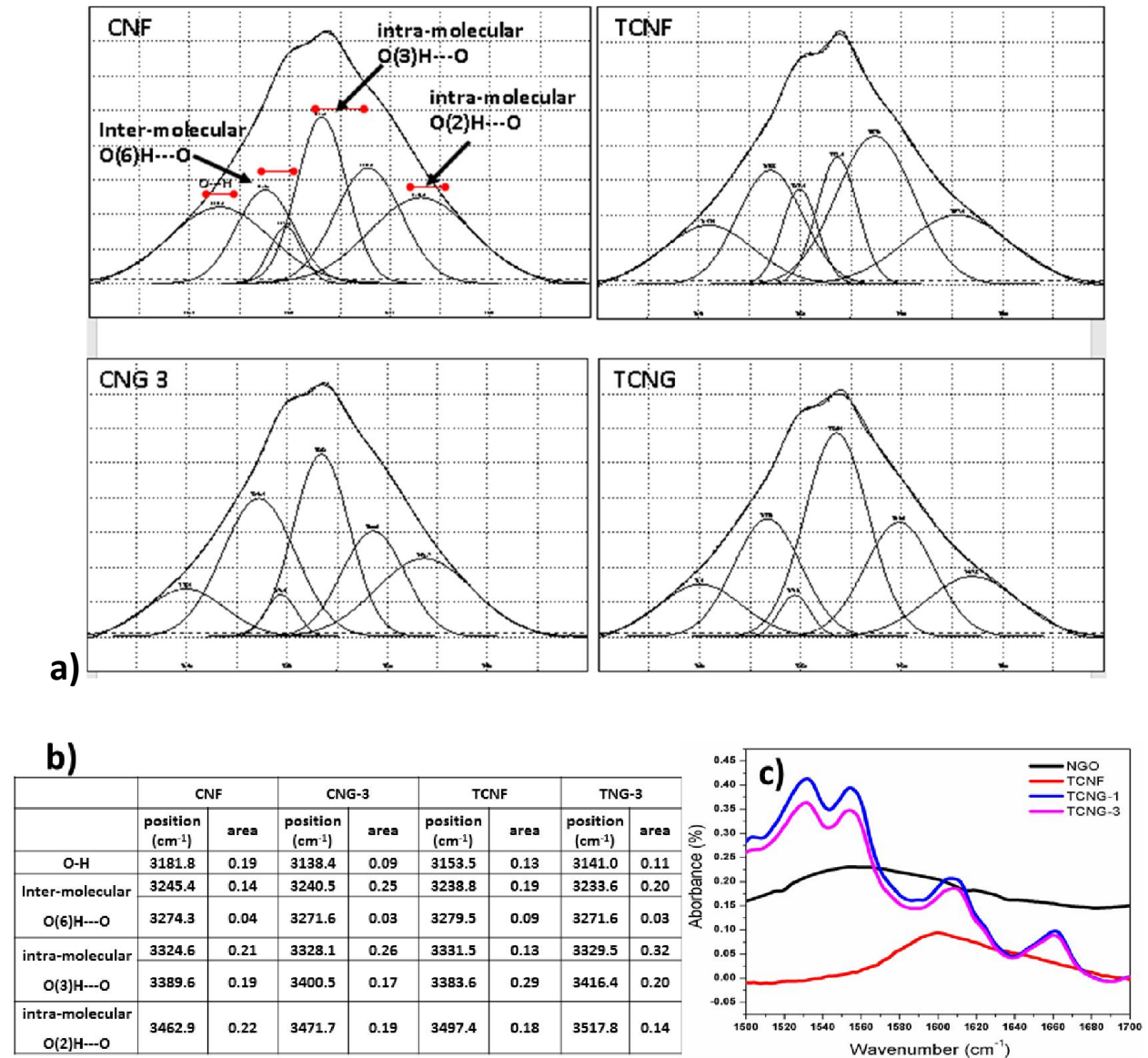
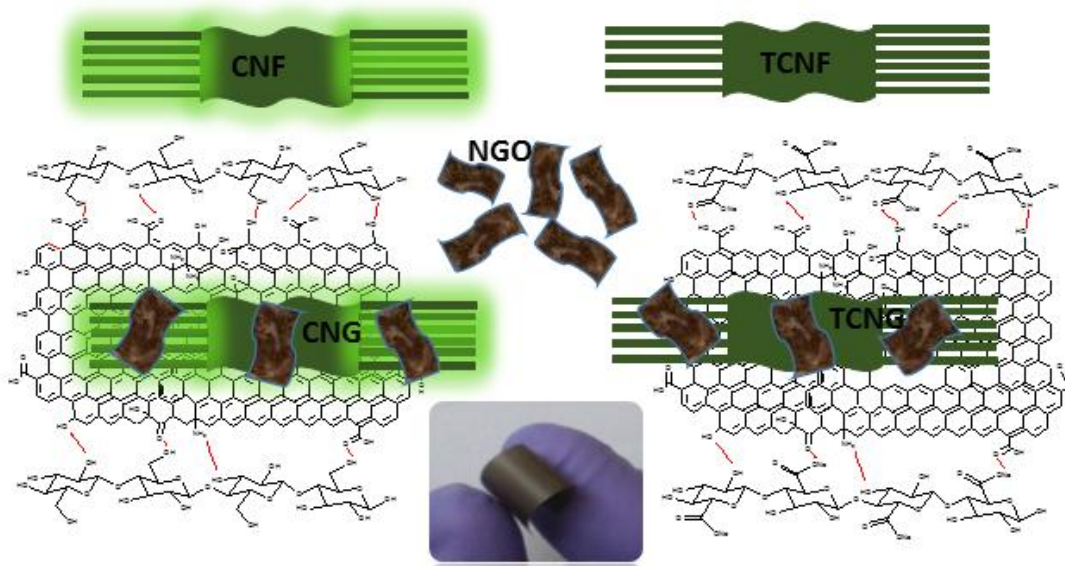


Fig 4.2. De-convoluted FTIR spectra of ν OH region (a) between 3000-3700, (b) table with relevant positions and areas of peaks for CNF and TCNF films without and with inclusion of 3 wt% of NGO and (c) 1500-1700 for NGO, TCNF, TCNG-1 and TCNG-3 composite films.



Scheme 1: Schematic illustration of possible interactions of CNF/TCNF with NGO with inserted digital image of the composite film.

The XRD patterns of CNF, TCNF and the nanocomposite films with different NGO loadings are shown in Fig. 2.3, which reveals interesting facts about the dispersion of NGO and the sample morphology. In the case of CNF and TCNF, two characteristic peaks centred at around 15.5° and 22.8° are observed, corresponding to the planes (1 0 1), and (0 0 2), a typical profile of cellulose I allomorph [17]. The broad diffraction peak at 15.5° indicates the partly crystalline nature of the cellulose. By increasing of NGO into the CNF matrix, a separation of the broader peak at 15.5° into two and an intensity decrease of the peak at 22.8° can be seen, indicating on the exfoliation of the layered NGO nanosheets from the cellulose matrix. Instead, in the case of using TCNF, the XRD spectra are similar, showing the excellently dispersed NGO without effect on the crystallinity.

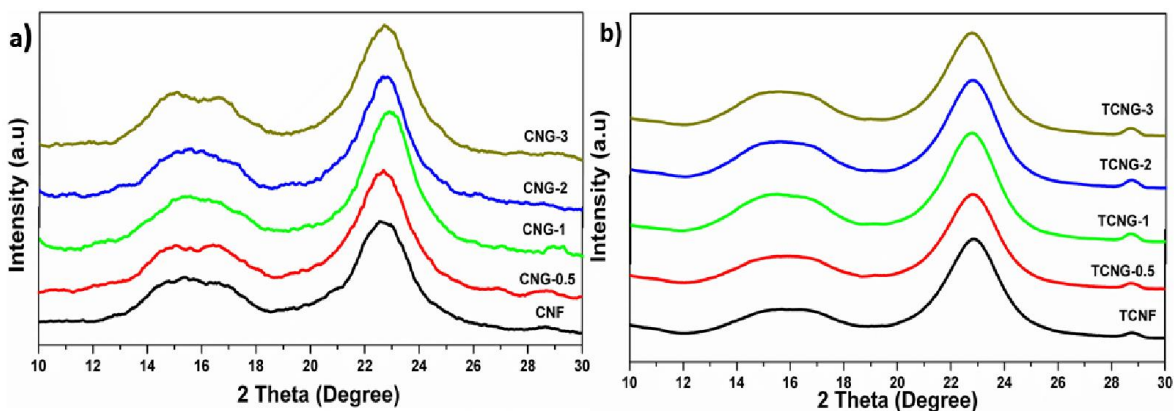


Fig. 4.3. XRD patterns of (a) CNG and (b) TCNG composite films.

The light transmittance of neat CNF vs. TCNF and nanocomposite films with embedded NGO were measured by UV-Vis spectroscopy in the wavelengths region of 250-750 nm, being illustrated in Fig. 2.4 and the transmittance data given in Table 2. The spectrum of CNF exhibits the highest transmittance (~90 %) compared to the TCNF film (~83%) in the visible light range (400-800), which may be credited to the presence of the large amount of carboxyl functional groups in TCNF as compared to the CNF matrix. The transparency of all composite films decreased with an increment of NGO content, more prominent in the case of TCNG composite films as compared to the CNG ones, leading to ~30% and ~46% transparency at 3 wt% of NGO addition. A different decrease of transmittance with NGO loading may be due to the light scattering effect at the interface of cellulose/GO and their defects, as well as the number of graphene layers and the composite films.

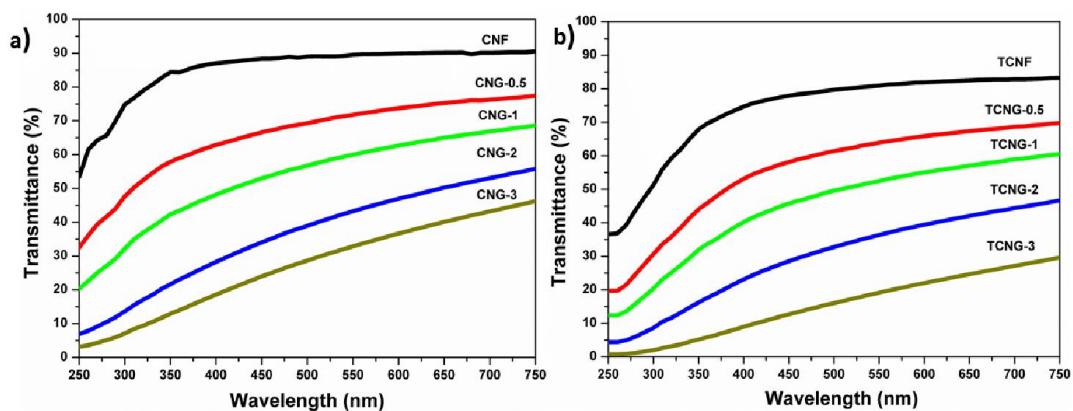


Fig. 4.4. UV-visible spectra (a) CNG and (b) TCNG composite films

The SEM analysis of the film surfaces and cross-section was performed to investigate the dispersion quality and the surface morphology of the nanocomposite films. No agglomeration of NGO was observed in the nanocomposites, as illustrated in the images in Fig. 2.5. However, the cross-section images reveal that the cellulose nanofibrils interacted strongly with the NGOs, also partly leading to nanofibrils entangling, being seen by the more compact and dense network structure. At the 3 wt% of NGO loading, the layers are stacked in a much more compact manner and CNFs became oriented horizontally, expressed more in the TCNF-based composites due to the interfacial interaction which restrained the CNF chains and the formed chain bridging between individual NGO sheets as already confirmed by XRD and FTIR spectroscopic study.

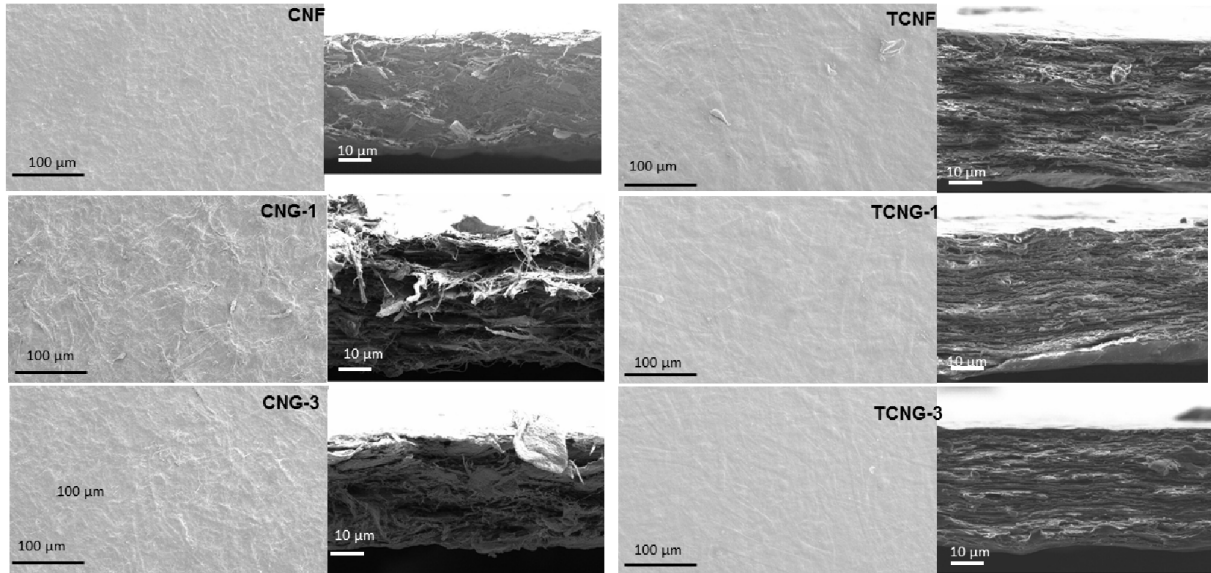


Fig. 4.5. SEM images of surface (left) and cross-section (right) of native and NGO loaded CNF and TCNF films.

The surface structure evaluation (i.e. root mean square roughness and surface area measured with the Surf CharJ plugin given in Table 2), indicated that both pure CNF and TCNF films show a comparatively smooth surface. By increasing of the NGO loading the roughness increase is more significant in the case of CNF as compared to the TCNG based films being supported by the Contact Angle measurements, which indicate indirectly the films' surface wettability properties. The water Contact Angle of the pure CNF film was found to be lower compared to the pure TCNF film ($\sim 49^\circ$ vs. $\sim 55^\circ$), which not only suggests the enhancement of hydrophobicity of the TCNF films but also reveals the surface microstructure properties of the films. Generally, a smoother surface gives a high Contact Angle value than a rough surface, although rough surfaces may also have substantially larger Contact Angles due to heterogeneous wetting being related to the formation of air compartments between the droplets and the substrate [18, 19]. The incorporation of NGO increased the water Contact Angles (to $\sim 64^\circ$ vs. $\sim 68^\circ$) which

supports strongly that the NGO sheets are exposed directly on the film surfaces by being embedded in the cellulose matrix, leading to an increased surface hydrophobicity of both CNF and TCNF film samples. Also, an increase of the contact angle of the other less polar solutions being tested (above all the formamide from $\sim 5^\circ$ to $\sim 29^\circ$ in the case of CNF, and from $\sim 25^\circ$ to $\sim 31^\circ$ in the case of TCNF) support these conclusions.

The addition of NGO had influence not only on the contact angle but also on the other surface parameters including surface energy, Lifshitz–van der Waals, Lewis acid and Lewis base components. The total surface free energy (γ^{TOT}) of CNF and TCNF is similar ($\sim 50 \text{ mJ m}^{-2}$) and quite high compared with NGO incorporated composites and it decreased to around $\sim 43 \text{ mJ m}^{-2}$ in the case of CNG-3 and TCNG-3 composite films, well correlated with an increased hydrophobicity. A closer look at the contributions of γ_s^{TOT} gives some interesting facts. There is no significant difference in the Lifshitz–van der Waals component of the film samples, whereas the electron donating contribution (γ_s^-), which is originating from the unsubstituted hydroxyl groups and impurities, decreased with the addition of NGO and were more noticeable at the highest NGO loading. Nevertheless, the acid-base term did not contribute significantly to the total surface free energy of the film samples. The higher value of γ_s^{LW} of the film samples may be attributed to the higher interaction ability of the dispersive part of C-O and C-C bonds within the cellulose molecule [20].

Samples	RMS roughness (μm)	Surface area (μm^2)	Contact angle θ ($^\circ$)				Surface energy (mJ m^{-2})			
			CH_3NO	H_2O	CH_2I_2	$\text{C}_3\text{H}_8\text{O}_3$	γ^{IW}	γ^*	γ^v	γ^{TOT}
CNF	10.38 ± 0.12	6.61 ± 0.14	5 ± 2	49 ± 3	59 ± 2	48 ± 3	30.17 ± 1.16	7.75 ± 0.75	15.92 ± 2.99	52.38 ± 4.38
CNG-0.5	15.26 ± 0.11	9.08 ± 0.09	12 ± 2	57 ± 3	56 ± 3	48 ± 3	32.70 ± 1.73	7.11 ± 1.00	9.58 ± 2.59	49.20 ± 5.13
CNG-1	24.13 ± 0.1	13.33 ± 0.19	31 ± 2	62 ± 3	60 ± 3	50 ± 2	30.08 ± 1.72	4.70 ± 0.88	10.74 ± 2.95	44.29 ± 5.00
CNG-2			24 ± 4	57 ± 1	55 ± 2	49 ± 2	32.03 ± 1.14	3.47 ± 0.55	16.26 ± 1.46	47.05 ± 3.00
CNG-3	15.07 ± 0.09	9.68 ± 0.12	29 ± 4	64 ± 2	56 ± 2	51 ± 2	31.29 ± 1.15	3.76 ± 0.65	10.47 ± 2.12	43.83 ± 3.51
TCNF	8.00 ± 0.14	5.13 ± 0.18	25 ± 2	55 ± 2	53 ± 4	75 ± 5	34.31 ± 2.31	3.78 ± 0.88	15.70 ± 2.27	49.72 ± 5.22
TCNG-0.5	11.4 ± 0.07	6.42 ± 0.07	30 ± 2	57 ± 2	58 ± 4	70 ± 2	37.15 ± 2.47	1.22 ± 0.49	18.59 ± 2.54	46.68 ± 5.04
TCNG-1	8.28 ± 0.08	5.33 ± 0.06	24 ± 3	62 ± 3	51 ± 2	45 ± 3	33.98 ± 1.12	4.95 ± 0.80	8.67 ± 2.68	47.07 ± 4.20
TCNG-2			31 ± 1	66 ± 2	55 ± 3	43 ± 3	31.78 ± 1.69	5.45 ± 0.82	6.68 ± 1.59	43.85 ± 4.03
TCNG-3	7.739 ± 0.18	4.97 ± 0.11	31 ± 1	68 ± 1	53 ± 2	53 ± 2	33.48 ± 1.13	4.81 ± 0.51	5.53 ± 0.77	43.80 ± 2.39

Table 4.1 Surface properties (roughness, area, contact angle, surface energy) of native and NGO loaded CNF and TCNF composite films.

4.3 Mechanical properties

Tensile testing was performed to identify the effect of NGO content on the mechanical properties of the CNF and TCNF film composites. Fig 4.6 displays a typical stress-strain curves of CNG and TCNG composites with different contents of NGO, and the results are listed in Table 4.2. Compared to the native CNF, TCNF has about a 25% increment (from ~ 59 MPa to ~ 74 MPa) of tensile strength and 33% increment (from ~ 1540 MPa to ~ 2045 MPa) in Young's modulus. This increment in tensile properties may be attributed due to the difference in inter and intra hydrogen bonding patterns of the films, already well defined by FTIR analysis. As such, the enhanced properties of TCNF over CNF provide great potential for the application of ultra-strong and ultra-stiff materials.

The addition of NGO increased the Young's modulus and tensile strength significantly and, as expected, was more intensive in the case of using TCNF. The incorporation of NGO to CNF also increases significantly the strain-to-failure (%) that slightly fluctuated in the composites with TCNF. The CNF-based films are more ductile compared to the brittle nature of the TCNF-based

ones, showing an enhanced toughness. However, this phenomenon again illustrates that the reinforcement effect of GO sheets has a close relationship with the dispersion state of NGO in the cellulose matrix. The addition of 0.5 % of NGO into the CNF matrix resulted in an enhanced tensile strength and modulus of ~77 MPa and ~2060 MPa, respectively, which corresponds to about a 30 % and 34 % increment than that of the CNF film. At the highest (3 wt%) of NGO loading, both values were increased further to ~81 MPa and ~2920 MPa by using CNF, reaching values of ~88 MPa and ~3390 MPa at TCNF-based film composites, respectively. The observed superior mechanical properties at 3 wt% of filler loading shows significant enhancement than reported studies. Kim *et. al* reported a 10.5% tensile strength enhancement and around 67% of decreased toughness at 3 wt % of graphene oxide filled cellulose composites with N-methylmorpholine-N-oxide monohydrate solvent [21]. B. wang et al. also studied the mechanical properties of microcrystalline cellulose-graphene oxide composites. At 3 wt% of GO, the tensile strength increased by 9.6% and a decreased stress to strain failure of 34% [12]. It was generally observed that the GO started to aggregate in the polymer composites at the higher loading levels due to the sheet-to-sheet interaction caused by the inadequate compatibility between the sheet and the polymer chains [22, 23]. The mechanical properties in this work were improved continuously up to 3 wt% of its loading in both types of composites, indicating well dispersed and distributed NGO sheets within both the CNF and TCNF matrices as already evidenced by SEM observations.

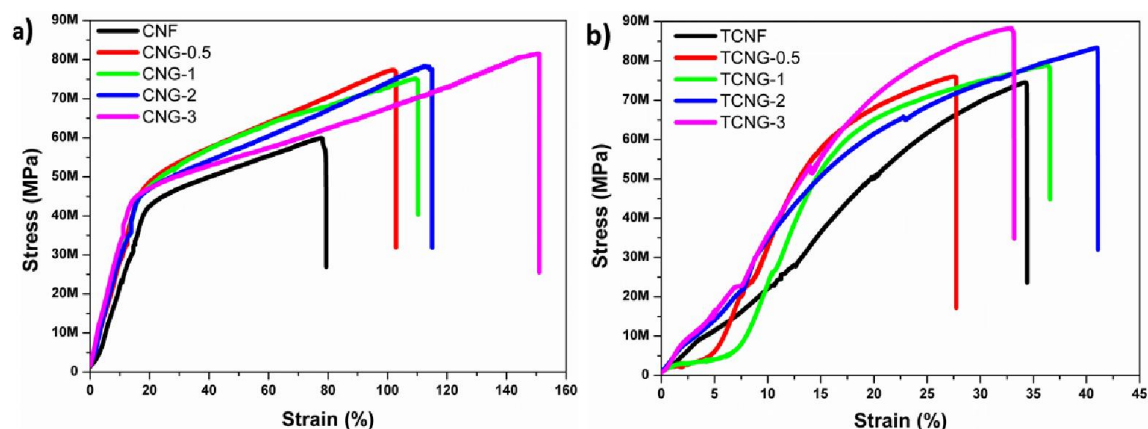


Fig. 4.6. Stress-strain curves of (a) CNG and (b) TCNG composite films.

Sample	Tensile strength (MPa)	Strain-to-failure (%)	Young's modulus (MPa)	Transmittance (%)	Dielectric constant at 1 MHz
CNF	59.8 ± 1.3	93.1 ± 3	1540 ± 297	90.5	7.54
CNG-0.5	77.3 ± 0.8	117.2 ± 2	2060 ± 419	78.1	33.43
CNG-1	75 ± 0.5	126.0 ± 0	2220 ± 280	69.8	38.63
CNG-2	78.3 ± 2	129.7 ± 1.5	2480 ± 170	62.9	39.14
CNG-3	81.5 ± 1.8	168.3.7 ± 3	2920 ± 155	46.2	46.01
TCNF	74.5 ± 1.5	57.6 ± 0.4	2045 ± 260	83.3	9.74
TCNG-0.5	76.0 ± 0.5	41.0 ± 0.5	2820 ± 129	69.7	28.05
TCNG-1	78.8 ± 0	50.3 ± 0.3	3040 ± 52	60.4	30.97
TCNG-2	83.3 ± 1.2	66.4 ± 0.8	3190 ± 95	46.6	31.70
TCNG-3	88.3 ± 2	57.01 ± 0.5	3390 ± 164	29.5	51.46

Table 4.2 Mechanical, Transmission and dielectric data of native and NGO loaded CNF and TCNF composite films.

4.4 Thermal properties

Thermal stability has a significant importance in such material applications. The thermal properties were evaluated by studying the thermal decomposition behaviours of CNF and TCNF with incorporated NGO fillers performing TGA analysis in a nitrogen atmosphere over the temperature range of 100-800°C. As seen from the thermograms in Fig. 6A the first stage weight loss, which occurred over the temperature range between 125-200 °C, resulted from the evaporation of water, and second weight loss occurred between 200-374 °C being related to the decomposition of the CNF in the composites [24]. In the case of TCNG composite films (Fig. 4.6 b), the first weight loss occurred between 115-230 °C and the second one between 235-344 °C.

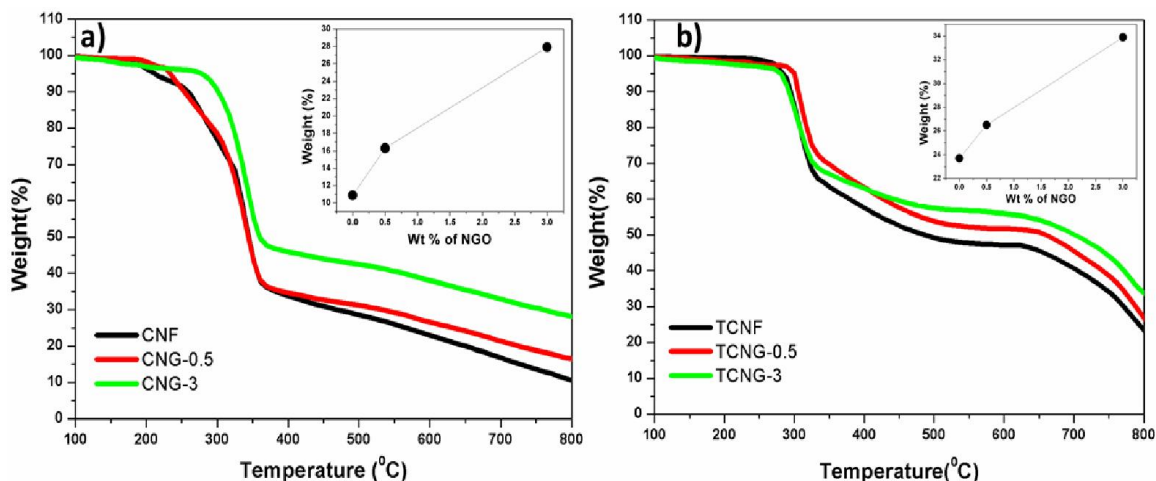


Fig. 4.7. TGA curves of (a) CNG and (b) TCNG composite films and their carbon yield values at 800 °C as a function of NGO loading (inserted graph).

The thermal degradation temperature (T_d) and the carbon yields at 800°C of both sets of composites (CNF vs. TCNF based ones) at 3 wt% of NGO loading were improved compared with the reference ones. The T_d at 10% weight loss of CNF was at ~262.4 °C whereas it increased to ~295.5°C at TCNF, indicating the enhanced thermal stability already of the neat matrix material.

The addition of NGO to the CNF matrix enhanced the T_d without changing the network of TCNG composites. The carbon yields of CNG-3 (~28 %) and TCNG-3 (~34 %) had a drastic improvement compared to the neat CNF (~11 %) and TCNF (~24 %), respectively, being accredited to the firm interaction between the cellulose fibrils and GO sheets as confirmed by FTIR and SEM analysis and mechanical behaviour. The high carbon yield is due to the suppression of cellulose fibrils' mobility at the interface of the composite films due to their strong interaction with the NGO loaded sheets [13]. Such an increment in carbon yield of the composite materials is a useful property for high temperature applications.

4.5. Dielectric properties

The frequency dependence dielectric constant (ϵ') and conductivity (σ') of the neat CNF vs. TCNF matrices and respective NGO embedded composites measured at room temperature from 10 Hz to 1 MHz are shown in Fig. 2.8. The dielectric constant of polymer nanocomposites is the measure of micro-capacitors which are formed by filler particles acting as electrodes filled with insulating matrices and the polarization centres which are initiated from the defects in the nanofiller structure³⁴. Several studies have been reported on the enhancement of dielectric responses of the cellulose polymer with graphene-based fillers [6,14,15]. The dielectric properties of cellulose/GO composites were studied by Kafy et al⁶ at 20 Hz and achieved for 190 times enhancement for the 3 wt% GO filled composites rather than neat cellulose. Mohiuddin et al.¹⁴ reported an 80% increase in the dielectric constant in modified reduced GO/cellulose acetate composites compared to the neat cellulose acetate at 150 Hz. Sadasivuni et al [15] described the dielectric enhancement of reduced GO/cellulose films at 22 Hz and 1 KHz and obtained 44 and 4 times improvements respectively over neat polymer.

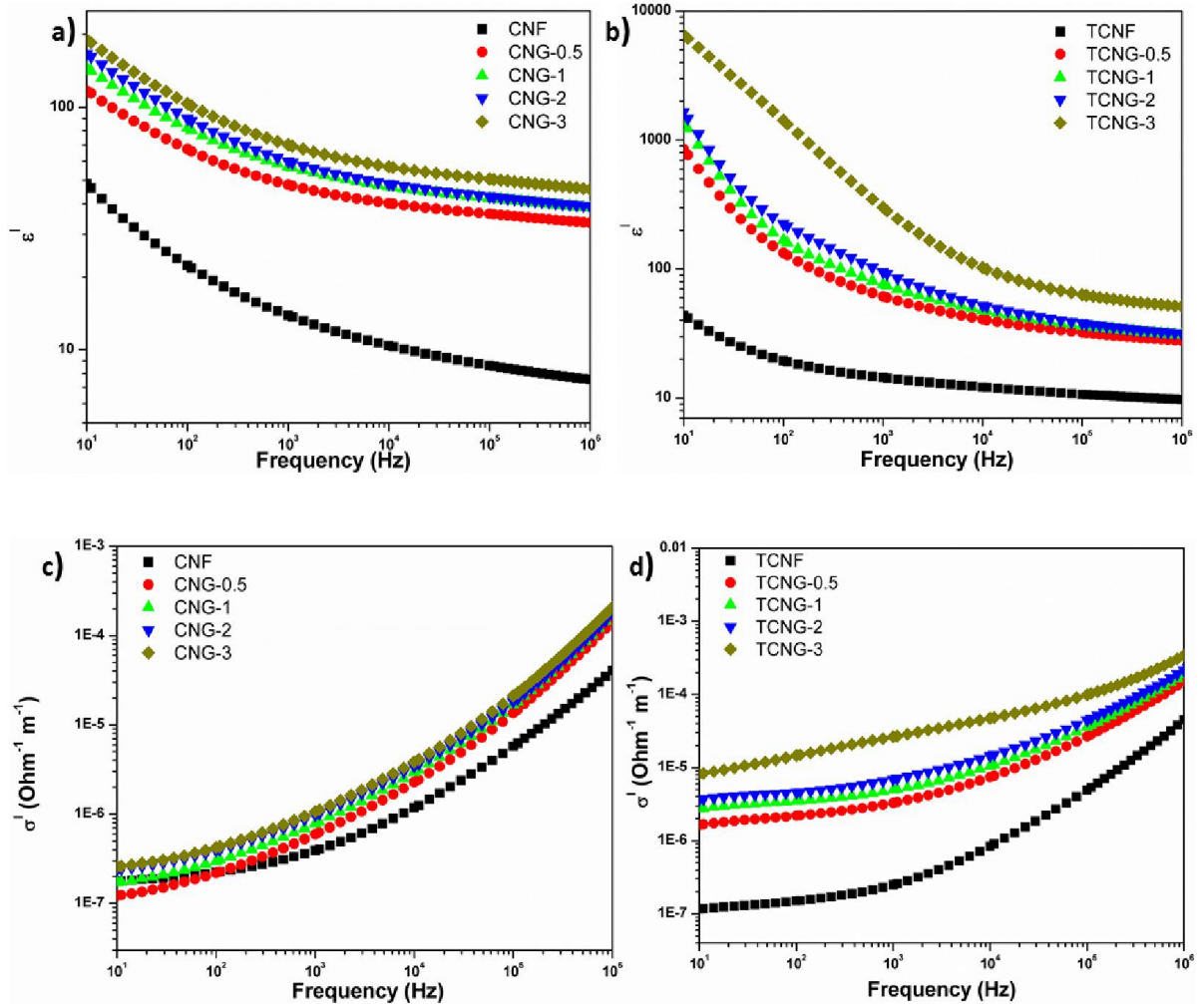


Fig.4.8. Frequency dependence of the dielectric constant (ϵ') of (a) CNG and (b) TCNG; ac conductivity (σ') of (c) CNG and (d) TCNG composite films measured at room temperature.

However, all the previous reported studies investigated the dielectric properties of the materials at lower frequency regions. Generally, the dielectric constant increases with frequency-lowering due to the space charge contribution. Moreover, at low frequencies, the external effects, such as the presence of surface layers (for example, due to the formation of Schottky barriers) often govern the dielectric response [25]. To provide the real intrinsic materials' properties, we, therefore, compared (Fig. 4.9) the values detected at the highest measured frequencies, i.e. at 1 MHz. The ϵ' values of CNG-3 and TCNG-3 composite films increased from ~ 7.5 and ~ 9.7 to ~ 46

and further to ~ 51.5 , respectively, compared to the neat CNF and TCNF films. The enhancement of dielectric properties in the present study than reported studies may be attributed to the improved dispersion effect of graphene oxide fillers and cellulosic matrices, already discussed by mechanical analysis.

The evolution of the dielectric constant (ϵ') of CNG and TCNG composite film samples is shown in Fig. 4.9. The enhancement in the case of composites originates from the synergetic Maxwell–Wagner–Sillars (MWS) polarization effect in which the polymer–filler interfacial interaction is necessary to induce changes in the dielectric properties of the nanocomposites. The nanocomposite provides the enormous interfacial area for abundant sites for the reinforced MWS effect. When a current flow across the two-material dielectric interfaces, GO sheets and CNFs matrix, charges accumulate at the interface because of the presence of functional groups and conjugation on the GO sheet surface, which forms an effective capacitor network to store energy [6]. The presence of an intensive amount of charges in the case of TCNF may be attributed to the enhanced dielectric property of TCNG film samples. This enormous enhancement in dielectric constant by adding NGO sheets into the cellulose matrices can be credited to the more MWS effect leading to high dielectric permittivity due to the entrapment of charge carriers in the interface.

AC conductivity (σ') of CNG and TCNG composite films is also increased with an increase of the frequency over the whole investigated frequency range, as well as with increases of the NGO content (Fig. 4.8). At lower frequency, the NGO sheets are effectually blocked, whereas at higher frequencies the charge carriers cannot block the boundaries, giving an effective conductivity. At 1 MHz, the composite film showed a σ' value of $\sim 2.07 \times 10^{-4} \text{ Sm}^{-1}$ and $\sim 3.46 \times 10^{-4} \text{ Sm}^{-1}$ for CNG-3 and TCNG-3, respectively. This increment in TCNG composite film may be

related to the formation of a network with more densely and horizontally oriented components as compared to the CNG one, being already well defined by SEM images.

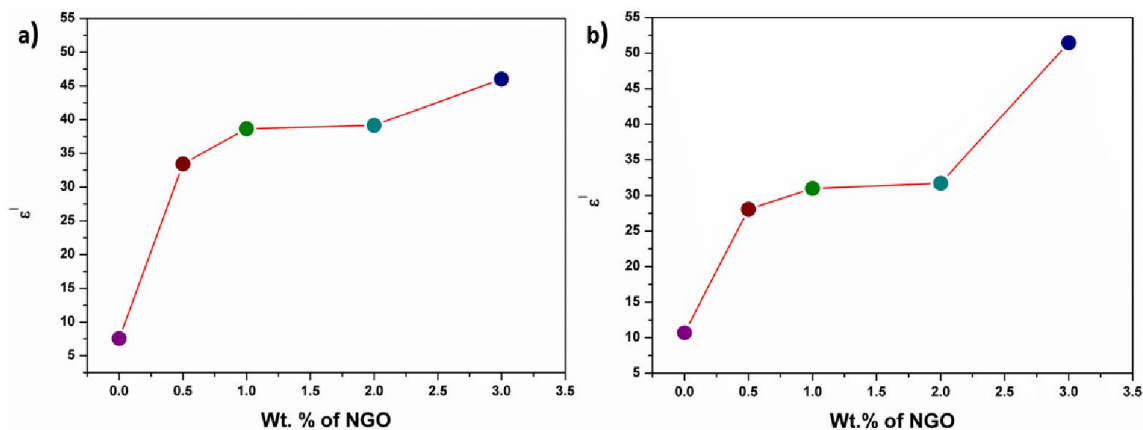


Fig.4.9. Evolution of the real part of the dielectric constant (ϵ') at frequency of 1 MHz vs. NGO loading for (a) CNG and (b) TCNG composite films.

4.6 Electrochemical properties

The electrochemical behaviour (electron transfer) and charge storage performance was evaluated for the CNG and TCNG films with 3wt% of NGO as paper electrodes by cyclic voltammetry (CV) recorded with a three-electrode setup in 1M H₂SO₄ electrolyte solution. A well-defined quasi-reversible ($I_{pc}/I_{pa} \leq 1$) shapes of CV curves (Fig. 4.10) show that the samples have a capacitive behavior [26]. Since the discharge current is restricted, the material is more suitable to be used as negative electrodes. The reduction peaks around -0.2V in the case of TCNG-3% sample shows the excellent reduction effect. Also, a decrease of the specific capacitances (SCs) with increasing scan rates attributed to the fact that the electrolytic ions cannot fully adsorb on the active electrodes because of the low diffusion time [27]. However, the SCs of studied cellulose films are comparable to the reported results. Dengteng et al. reported a volumetric capacitance of 40.5 F/cm³ and areal capacitance of 0.33 F/cm² for foldable supercapacitor electrodes using a

macroporous cellulose fibers with single-walled carbon nanotubes/PANI nanowires, which was attributed to the synergistic effect of electron transport within the SWCNTs network and fast charge transfer of the PANI nanoribbons [28]. Nanocellulose derived porous carbon aerogels are reported by Guoqing et al. with SC of 205 F/g reached at a current density of 20 A/g within a potential window of -1.0 to 0 V [29].

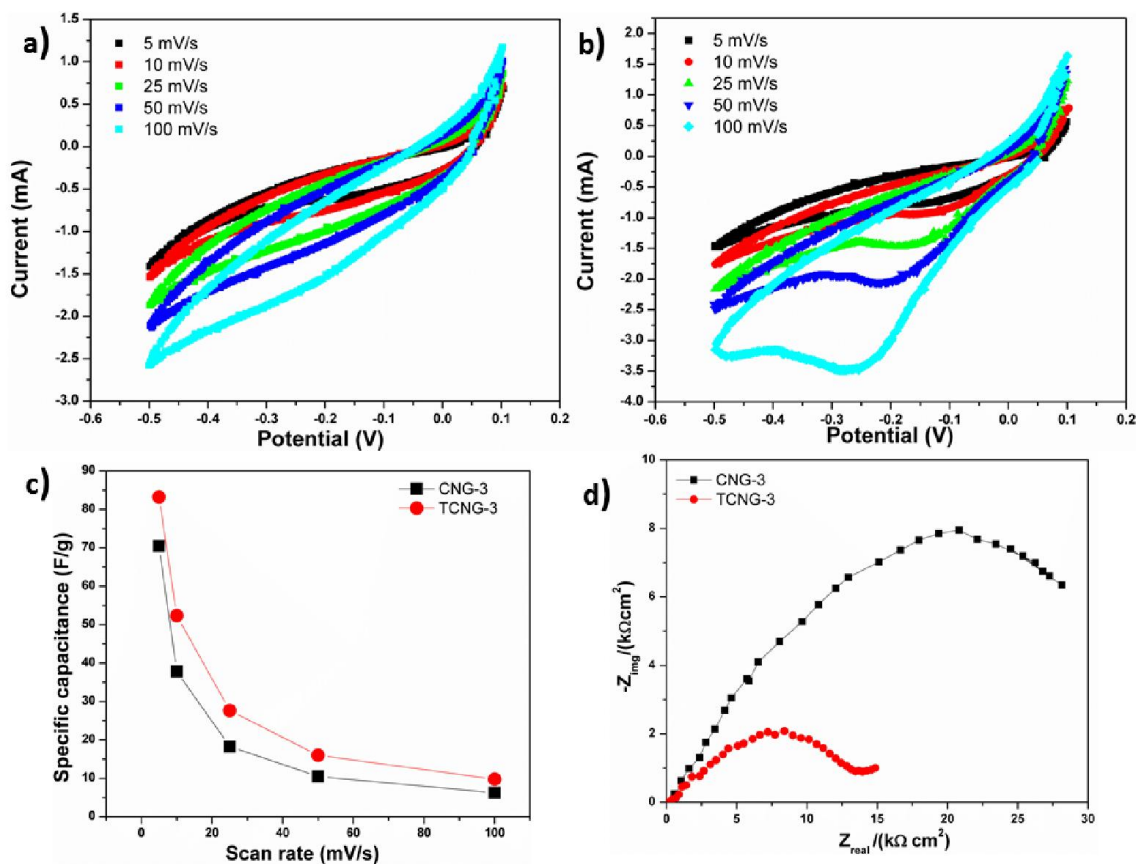


Fig. 3.10. Cyclic voltammograms of CNG-3 (a) and TCNG-3 (b); specific capacitance (c) of CNG-3 and TCNG-3 composite films as working electrodes with different scan rates; (d) Nyquist spectra for CNG-3 and TCNG-3

Nyquist spectra were measured at an open-circuit potential and are presented in figure 10 d. The Nyquist plot for TCNG – 3% shows a depressed semi-circuit. For that sample no indication

for the diffusion process is involved (in the case of diffusion the measured data would deviate at low frequencies from the Z_{real} axis). The depressed semi-circuit is usually explained with the inhomogeneity of the electrode (in this case the both used materials) and this occurs due to the random distribution of the nanoparticles. The depressed semi-circuit results from a parallel combination of the charge-transfer resistance and constant phase element (CPE). Therefore, the TCNG – 3% system is under kinetic-controlled process and can be represented with a $R_s(RQ)$ equivalent electrical circuit. R_s stands for the solution resistance (resistance of the ion conducting paths that developed inside the material), R stands for the charge-transfer resistance and Q for CPE. The impedance of the CPE is described as $Z(\text{CPE}) = (Q(j\omega)^n)^{-1}$ [30]. On the other hand, the measurement for the CNG – 3% shows also depressed semi-circuit, but at the lowest frequencies measured (at the highest Z_{real} values in the figure 9d), also the deviation of the measured impedance data from the Z_{real} axis. This implies that the CNG – 3% system is also under diffusion-controlled process, due to the ions that migrate into the electrode material, which is associated with capacitive performance. Therefore, sample CNG – 3% is under kinetic-controlled and diffusion-controlled processes and can be represented with a $R_s(R(QW))$ equivalent electrical circuit. W stands for the semi-infinite (unrestricted) layer thickness diffusion.

4.7 Conclusion

Flexible eco-friendly nanocomposite films were fabricated by incorporating ammonia-functionalized graphene oxide (NGO) into the native (CNF) and TEMPO-oxidized (TCNF; carboxylated) cellulose nanofibrils matrix using a solvent casting method. The reduced wettability and increased smoothness of the films' surface, as well as increased mechanical strength and thermal stability, are in good agreement with the increased (0.5-3 wt%) NGO loading concentration revealed on its low aggregation and good dispersibility within the CNFs matrix, being improved further within more densely and horizontally-orientated TCNFs due to increased physico-chemical interactions with the NGO nanosheets. Besides, the high dielectric constant and AC conductivity at a relatively high-frequency region (1 MHz) with comparable electrochemical energy storage capacity demonstrated that such ultra-strong and ultra-stiff composite films are suitable cost-effective alternative green materials for flexible energy storage devices.

3.7 References

1. Zhang, Yi-Zhou, et al. "Flexible supercapacitors based on paper substrates: a new paradigm for low-cost energy storage." *Chemical Society Reviews* 44.15 (2015): 5181-5199.
2. Wang, Cheng-Yin, et al. "Stable low-voltage operation top-gate organic field-effect transistors on cellulose nanocrystal substrates." *ACS applied materials & interfaces* 7.8 (2015): 4804-4808.
3. Yang, Gwangseok, et al. "Flexible graphene-based chemical sensors on paper substrates." *Physical Chemistry Chemical Physics* 15.6 (2013): 1798-1801.
4. Weng, Zhe, et al. "Graphene–cellulose paper flexible supercapacitors." *Advanced Energy Materials* 1.5 (2011): 917-922.
5. Inui, Tetsuji, et al. "A miniaturized flexible antenna printed on a high dielectric constant nanopaper composite." *Advanced Materials* 27.6 (2015): 1112-1116.
6. Kafy, Abdullahil, et al. "Designing flexible energy and memory storage materials using cellulose modified graphene oxide nanocomposites." *Physical Chemistry Chemical Physics* 17.8 (2015): 5923-5931.
7. Tian, Mingwei, et al. "Enhanced mechanical and thermal properties of regenerated cellulose/graphene composite fibers." *Carbohydrate polymers* 111 (2014): 456-462.
8. Dreyer, Daniel R., et al. "The chemistry of graphene oxide." *Chemical Society Reviews* 39.1 (2010): 228-240.
9. Marcano, Daniela C., et al. "Improved synthesis of graphene oxide." *ACS nano* 4.8 (2010): 4806-4814.
10. Novoselov, Kostya S., et al. "Electric field effect in atomically thin carbon films." *science* 306.5696 (2004): 666-669.

11. Valentini, L., et al. "A novel method to prepare conductive nanocrystalline cellulose/graphene oxide composite films." *Materials Letters* 105 (2013): 4-7.
12. Wang, Baogang, et al. "Relationship between dispersion state and reinforcement effect of graphene oxide in microcrystalline cellulose–graphene oxide composite films." *Journal of Materials Chemistry* 22.25 (2012): 12859-12866.
13. Yao, Lili, et al. "Effect of graphene oxide on the solution rheology and the film structure and properties of cellulose carbamate." *Carbon* 69 (2014): 552-562.
14. Mohiuddin, Md, et al. "Flexible cellulose acetate/graphene blueprints for vibrotactile actuator." *RSC Advances* 5.43 (2015): 34432-34438.
15. Sadasivuni, Kishor Kumar, et al. "Reduced graphene oxide filled cellulose films for flexible temperature sensor application." *Synthetic Metals* 206 (2015): 154-161.
16. M. Fan, D. Dai and B. Huang, *Fourier Transform Infrared Spectroscopy for Natural Fibres in Fourier Transform – Materials Analysis*, ed. Salih Mohammed Salih, ISBN 978-953-51-0594-7, May 23, 2012
17. Kabiri, Roya, and Hassan Namazi. "Nanocrystalline cellulose acetate (NCCA)/graphene oxide (GO) nanocomposites with enhanced mechanical properties and barrier against water vapor." *Cellulose* 21.5 (2014): 3527-3539.
18. Ryan, Bernard J., and Kristin M. Poduska. "Roughness effects on contact angle measurements." *American Journal of Physics* 76.11 (2008): 1074-1077.
19. Cassie, A. B. D., and S. Baxter. "Wettability of porous surfaces." *Transactions of the Faraday society* 40 (1944): 546-551.

20. Mohan, Tamilselvan, et al. "Wettability and surface composition of partly and fully regenerated cellulose thin films from trimethylsilyl cellulose." *Journal of colloid and interface science* 358.2 (2011): 604-610.
21. Kim, Chan-Jun, et al. "Graphene oxide/cellulose composite using NMMO monohydrate." *Carbohydrate polymers* 86.2 (2011): 903-909.
22. Han, Donglin, et al. "Cellulose/graphite oxide composite films with improved mechanical properties over a wide range of temperature." *Carbohydrate Polymers* 83.2 (2011): 966-972.
23. El Achaby, Mounir, et al. "Mechanically strong nanocomposite films based on highly filled carboxymethyl cellulose with graphene oxide." *Journal of Applied Polymer Science* 133.2 (2016).
24. Zheng, Qifeng, et al. "Cellulose nanofibril/reduced graphene oxide/carbon nanotube hybrid aerogels for highly flexible and all-solid-state supercapacitors." *ACS applied materials & interfaces* 7.5 (2015): 3263-3271.
25. Li, Yuhan, et al. "Graphene sheets segregated by barium titanate for polyvinylidene fluoride composites with high dielectric constant and ultralow loss tangent." *Composites Part A: Applied Science and Manufacturing* 78 (2015): 318-326.
26. Yang, Peihua, and Wenjie Mai. "Flexible solid-state electrochemical supercapacitors." *Nano Energy* 8 (2014): 274-290.
27. Yang, Guang-Wu, Cai-Ling Xu, and Hu-Lin Li. "Electrodeposited nickel hydroxide on nickel foam with ultrahigh capacitance." *Chemical Communications* 48 (2008): 6537-6539.

28. Ge, Dengteng, et al. "Foldable supercapacitors from triple networks of macroporous cellulose fibers, single-walled carbon nanotubes and polyaniline nanoribbons." *Nano Energy* 11 (2015): 568-578.
29. Zu, Guoqing, et al. "Nanocellulose-derived highly porous carbon aerogels for supercapacitors." *Carbon* 99 (2016): 203-211.
30. Barsoukov, E. "JR Macdonald in Impedance Spectroscopy." *Theory, Experiment, and Applications*, 2nd ed., Edited by Wiley Interscience Publications (2005).

Chapter 5

Structure, morphology, mechanical, dielectric and electrochemical properties of untreated and UV treated composites of graphene oxide (GO) filled pristine and oxidized cellulose nanofibril composites

5.1 Introduction

Modern electronic industry desires high dielectric constant materials for the development of energy storage devices, flexible electronics, embedded capacitors, actuators, and sensors [1–6]. Due to their light weight nature, flexibility, low cost, and ease of processing, polymer based composites generated tremendous attraction as compared to inorganic materials, ceramics, and metals in previous years [3]. The low conductivity of graphene oxide (GO) limits its applicability for the fabrication of electronic devices, and several researchers paid their attention to reducing GO in numerous ways to obtain good electrical properties in cellulose based composites [2, 8-11,13]

Some reports are available for the in-situ chemical reduction of graphene oxide in cellulose based composites [2, 7-11] mainly using poisonous hydrazine as a reducing agent. Thermally reduced graphene was also reported [12,13], but here the addition of reduced graphene oxide into the celluloses matrices required the usage of organic solvents for better dispersion. Reported biological methods used a mannitol culture medium as the reducing agent together with bacterial cellulose [14] and strong alkaline solutions for the spinning of composite fibers [15]. These authors focused on the biomedical and thermomechanical

applications rather than electronic device fabrication. Reduction of graphene oxide, coated on a quartz crystal, in presence of hydrazine vapor in a closed chamber at 80 °C without any damage on the films for transparent conductors was reported recently[16] and cellulose nanocrystal/graphene oxide hybrid films were treated with hydrazine vapor at 50 °C²⁸. The reduction of graphene oxide was confirmed by the color changes of the films after treatment.

Contrary to previous works, this work reporting an environmentally benign method to reduce graphene oxide in cellulosic matrices by ultraviolet (UV) irradiation in an inert nitrogen atmosphere. Graphene oxide and graphene containing cellulose nonfibrillar films could be used in electronic applications with a proper method of material manufacturing and an electrical and mechanical performance that matches or exceeds current composite materials. The aim of this work is therefore to demonstrate the potential of the method and to elucidate the mechanism of reduction which could further also be extended to other polymer systems. Attenuated Total Reflectance-Fourier Transform Infrared (ATR-IR), UV-vis absorbance, X-ray photoelectron spectroscopy and charge titration are used to confirm the reduction. Field emission scanning electron microscopy (FE-SEM) is employed for morphological analysis. The dielectric responses were systematically analyzed for all the composite films. Dynamic storage modulus of the composites was analyzed by Dynamic Mechanical Analysis (DMA). The energy storage capacity was systematically studied by cyclic voltammetry and electrochemical impedance in both native (CNF) and TEMPO oxidized (TCNF) cellulose based composites of highest (3wt.%) graphene oxide loading (termed CGO-3 from CNF, TCGO-3 from TCNF).

5.2 Morphology of composite films

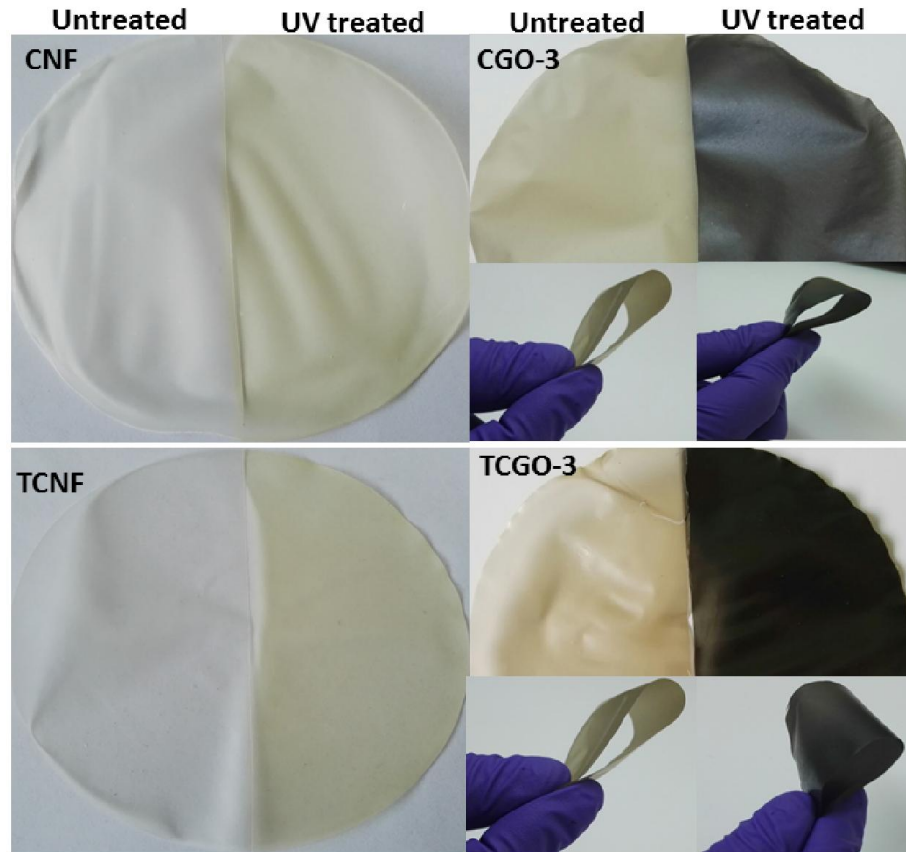


Fig. 5.1. digital images of composites before and after 5 hours of UV treatment.

Homogeneous cellulose nanofibrillar films (CNF) and their oxidized version (TCNF) are transparent/whitish and smooth materials (Fig. 5.1 a left images left half). UV treatment of these materials (left images right half) results in slight yellowish but stable films. Cellulose graphene oxide composites (right image left half) are flexible materials with a light brownish color with a certain transparency. The reduction of 3 wt% graphene oxide

to graphene in the cellulosic matrix is qualitatively confirmed by strong color changes to black (Fig 5.1, right image right half). (CGO-3, TCGO-3) whilst flexibility is retained.

UV-vis (250-750 nm) transmittance spectra (fig 5.2) further confirm quantitatively a reduction in transparency after UV-treatment. The lower transmittance values (~22%) for UV treated CGO-3 compared to the untreated sample (~80%) and (~18%) for UV treated TCGO-3 compared to the untreated sample (~71%) reflects the color changes in the digital images of the composites (Fig 5.1) and suggests the formation of a carbonaceous material with a higher absorbance of visible light.

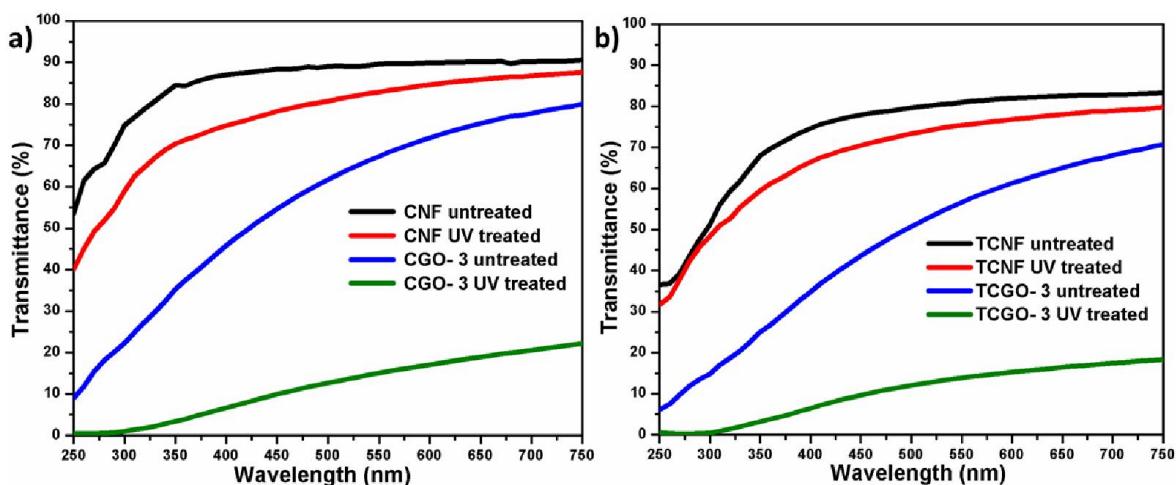


Fig. 5.2. UV-Visible spectra for untreated and 5 hours UV treated (a) CGO and (b) TCGO films compared to GO free reference samples (CNF, TCNF)

FESEM images (fig 5.3) qualitatively reveal the surface morphology of native and reduced composites. All composites appear relatively smooth and only untreated CNF/GO films seem to be somewhat rougher with distinct fibrils visible. More importantly roughness/morphology change slightly upon radiation. It is assumed here that the formation of graphene from GO causes a compaction of the material by the removal of oxygen

species. SEM images also confirm a microscopically intact film without larger pores or holes after UV exposure.

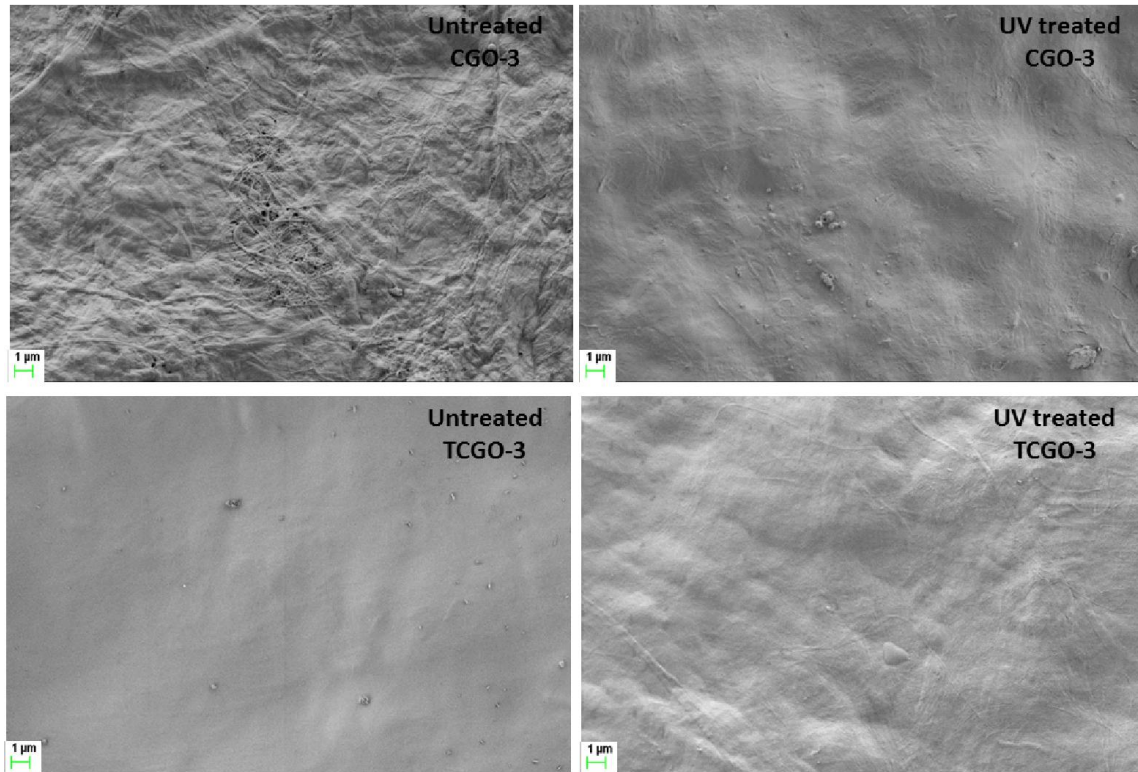


Fig. 5. 3. FESEM images of untreated and 5 hours UV treated CGO-3 and TCGO-3 films.

5.3 Structural properties composite films

The changes in intensity ratio of D and G bands in Raman spectra can manifest the effect of reduction process in graphene based composites [17]. From the Raman spectra (fig 5.4), the ID/IG ratio, gives an insight to the GO reduction process in cellulose composites. After UV treatment, the intensity of D and G band has increased from 1.15 to 1.27 and 1.24 to 1.52 for CGO-3 and TCGO-3 respectively. The increased ID/IG ratio of UV treated samples compared to untreated samples is the outcome of elimination of oxygen functionalities after UV induced reduction. This also suggest the formation of new graphitic domains in addition to the increased sp² cluster number after the UV induced reduction

[18]. The improved reduction of GO (fig 3 b) is observed in TCGO—3 films compared to its pristine counterpart would affect its material properties.

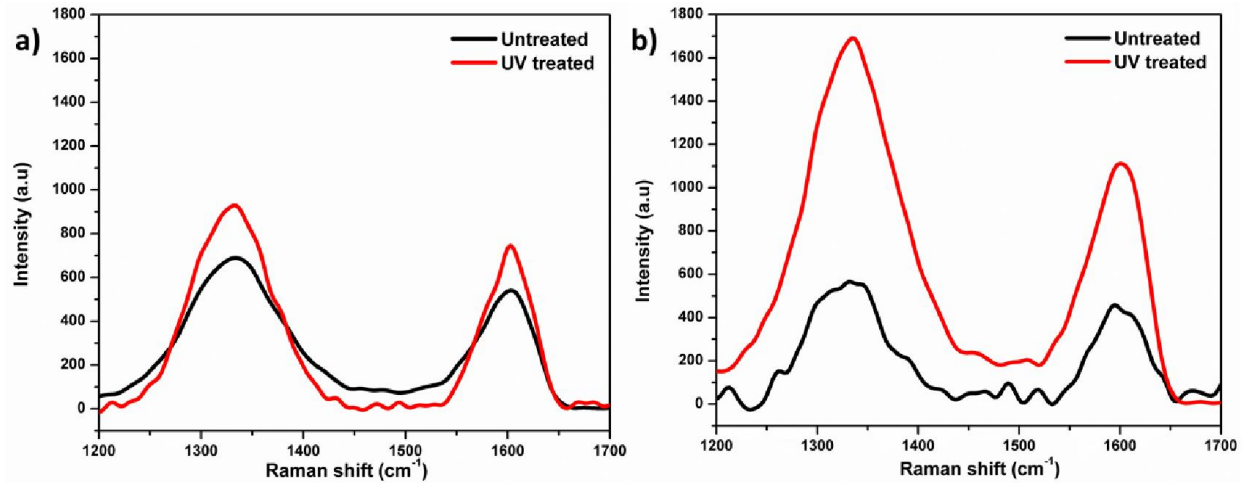


Fig. 5.4 Raman spectra for untreated and 5 hours UV treated (a) CGO-3 and (b) TCGO-3 films.

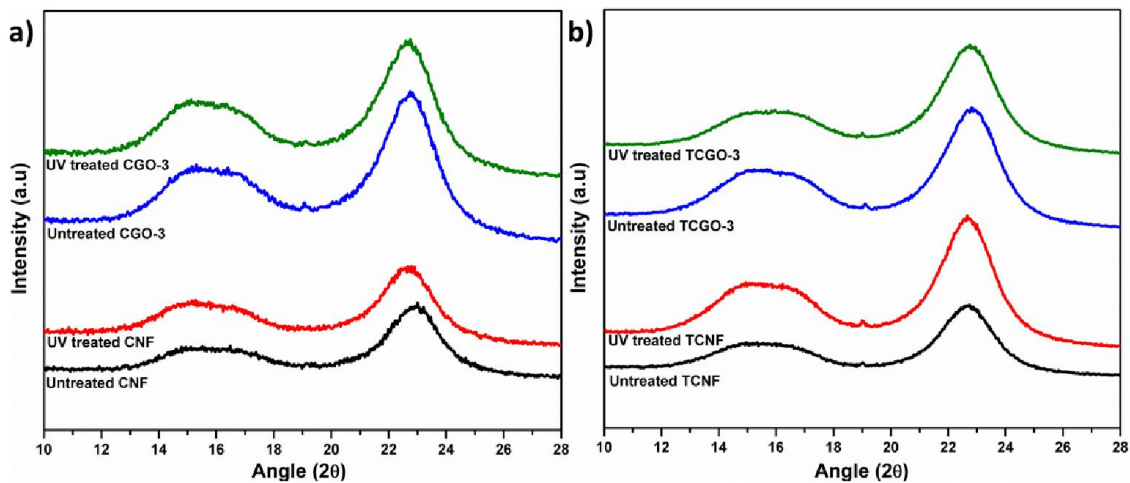


Fig. 5.5. XRD spectra for (a) CNF, untreated and 5 hours UV treated CGO-3 and (b) TCNF, untreated and 2 hours UV treated TCGO-3 film samples.

The crystallinity of cellulose composite films does not change significantly as XRD measurements revealed. The broad diffraction peak at around $2\theta: 16^\circ$ specifies the partial crystalline nature of cellulose [19]. The peaks at 16° and 22° correspond to the crystalline planes (101) and (002) respectively, typical of a cellulose I allomorph [20].

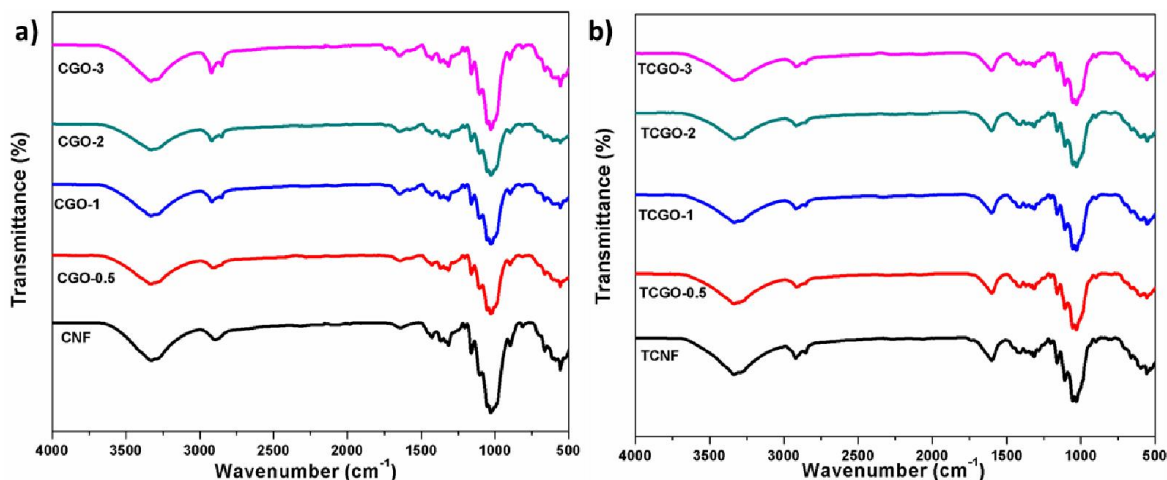


Fig. 5.6. ATR- FTIR spectra of CNF (left) and TNF (right) filled with 0.5; 1, 2 and 3 wt% graphene oxide (CGO, TGO). Curves are shifted by an arbitrary offset.

Infrared spectroscopy confirm the presence of carbonyl compounds 1580 cm^{-1} , 1547 cm^{-1} and bound water (1640 cm^{-1}) in native and graphene oxide filled CNF (Fig. 5.6 a) and TCNF (Fig. 5.6 b) films. Filling CNF with increasing amounts of GO results into a double peak for CH vibrations at 2900 cm^{-1} - and 2850 cm^{-1} (alkane, alkene and arene systems) and a new peak at 1741 cm^{-1} (probably C=O of aromatic systems in GO). Owing to the TEMPO mediated oxidation of cellulose a higher content of carboxylic groups is detected in TCNF a fact that is confirmed by charge titrations (table 5.1). Further TCNF contains already a pattern of aliphatic or aromatic CH groups similar to the IR spectra of filled CNF.

	CNF	TCNF	CGO-3	TCGO-3
Native	0.3±0.15	1.63±0.21	0.35±0.22	2.4±0.23
UV	0.78±0.2	1.07±0.11	0.1±0.12	1.31±0.21

Table 5.1: titrated charges of CNF/TNF and graphene oxide composites CG=3 and TCGO-3 native and UV treated samples

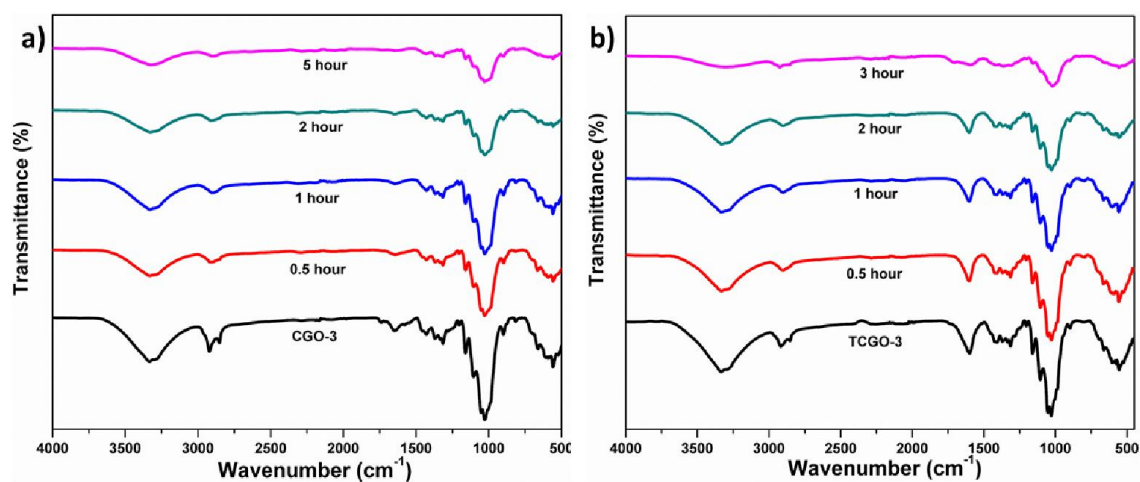


Fig. 5. 7. ATR- FTIR spectra of CGO-3 and TCGO-3 Native and UV-treated for 0.5, 1, 2 and 5 hours. Curves are shifted by an arbitrary offset.

Interestingly UV-treatment from 0.5 to 5 hours decreases the intensity of the aliphatic/aromatic CH peaks at 2850 cm^{-1} in both matrices indicating that the amount or mode of CH bonds in GO (and TCNF) is decreased (Fig. 6 left CGO-3, right TCGO-3).

Concomittantly C=O IR vibrations 1741 cm^{-1} , 1580 cm^{-1} , 1547 cm^{-1} in UV treated CGO-3 and the amount of titratable carboxylic groups in UV treated CGO-3 and TGO-3 (Fig 7, table 2) are reduced. The carboxylic group of TCNF covers the C=O vibrations which are visible for CGO-3 samples but a similar reduction can be assumed. A light induced radical reaction that leads to decarboxylation or cross-linking of carbonyls in the material can therefore be assumed [21].

For TCGO-3 carbonly bands are relatively stable upon irradiation but charges found by titration decrease significantly indicating crosslinking or decarboxylation. The collected data is an evidence for the reduction of GO to graphene by the removal or cross-linking of carbonyls/carboxyls and the reduction of the amounts and bonding mode of aliphatic/cyclic CH compounds. UV irradiation is known to cause photolytic chain splitting of cellulose and the subsequent formation of free radicals [21]. Together with reactions that stem directly from GO this can yield oxidized and reducing groups which are assumed to be responsible for the formation of reduced GO in the composites during radiation.

5.4. Temperature dependent dynamic mechanical properties

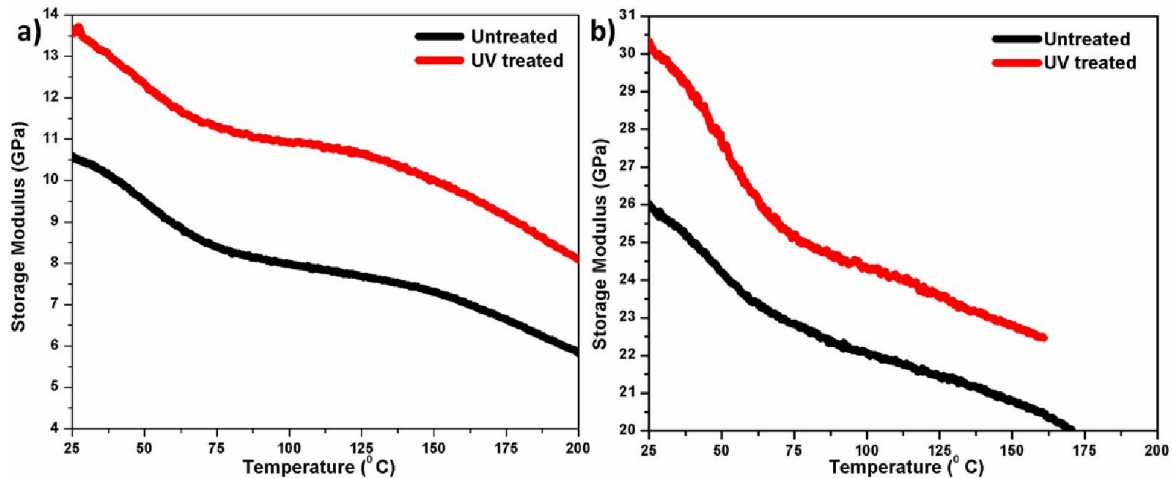


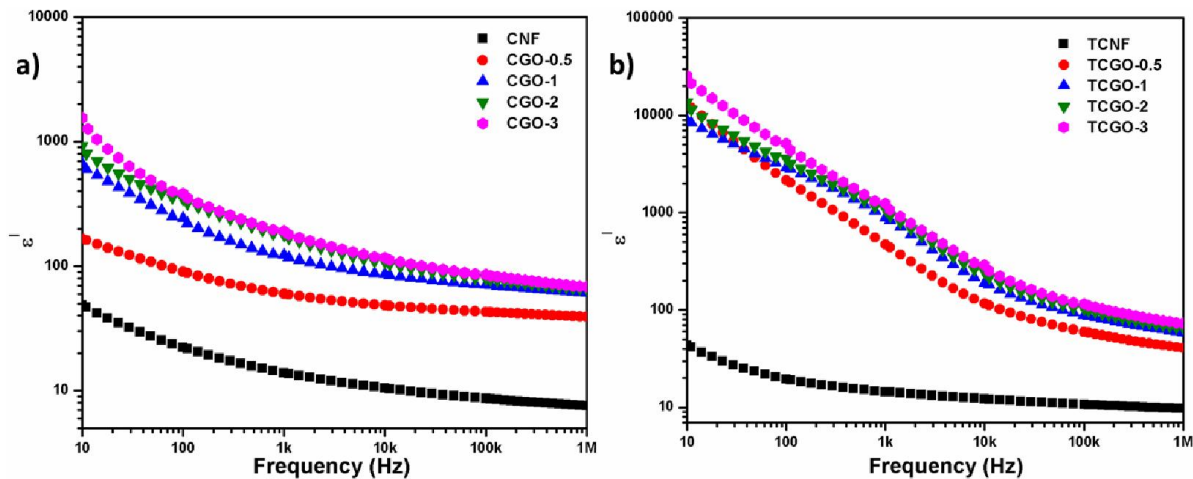
Fig 5.8. Temperature dependence of the dynamic storage modulus E^l for untreated and 5 hours UV treated (a) CGO-3 and (b) TCGO-3 films.

Dynamic mechanical analysis, which measures the response of samples to an applied oscillatory stress, was performed to estimate changes in mechanical properties before and after 5 hours of UV treatment (Fig 5). At 25 °C, untreated CGO-3 and untreated TCGO-3 have a mechanical storage modulus of 10.6 GPa and 25.9 GPa while UV treatment significantly increases it to 13.5 GPa for CGO-3 and 30.1 GPa for TCGO-3. Generally, storage modulus values are usually influenced by the interfacial adhesion between filler and polymer matrix. The results can therefore be interpreted by an increased adhesion between the graphene flakes with the cellulosic matrix or an increase of the interaction in cellulose or graphene itself after the UV induced reduction. For all samples the storage modulus decrease with temperature which can be interpreted as a softening of the composite material. The retention ratio defined as the ratio of the storage modulus at 150 °C to that at 25 °C is increasing with the UV treatment and reaches the highest value of 0.79 for the UV treated TCGO-3 film indicating a lower impact of heat on the deformability of

these films. It is worth noting that at higher temperatures ($>160^{\circ}\text{C}$), the TCGO-3 sample broke and the analysis was stopped confirming a higher brittleness of this type of composite [19]. The results also confirm that analyzed materials can practically resist higher temperatures usually observed in energy storage devices upon de- and recharging [22].

5.5. Dielectric properties

The frequency dependent dielectric properties at room temperature for CGO and TCGO, containing various amounts of GO, are shown in figure 5.9. The dielectric constant ϵ' , which is a measure of energy storage ability of a material, decreases with frequency for all investigated composites. Over the entire frequency range the dielectric constants of CGO and TCGO show a gradual increase with the amount of GO (ϵ' CGO-3: 68.92, ϵ' TCGO-3: 74.05) Previous reports on graphene filled polymeric composites find a comparable trend [1 ,23].



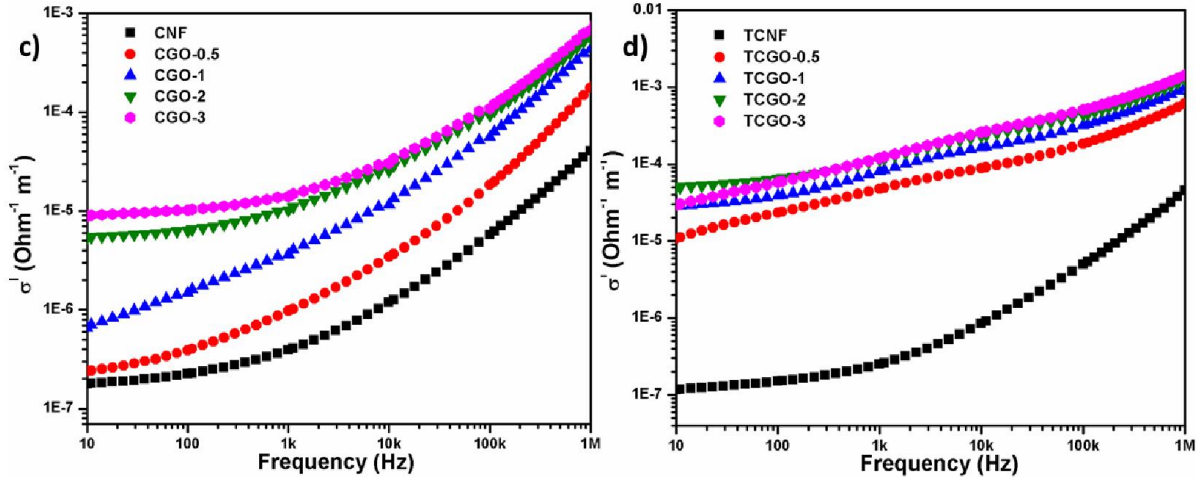


Fig. 5.9: Frequency dependence of the dielectric constant ϵ' (a, b) and ac conductivity σ' (c, d) measured at room temperature for untreated CGO and TCGO.

The present study however shows as significant enhancement of the dielectric constant [1,2,4,6, 12,19,23,24]. Many researchers used functionalized graphitic derivatives and hybrid fillers to achieve a high dielectric response. Chao et al. reported graphene oxide encapsulated carbon nanotube filled polyurethane composites. Functionalized reduced graphene oxide with polyethylenimine fillers were loaded in a PVDF matrix by Wangshu et al [1, 4]. The substantial improvement of the dielectric properties of our composites can be attributed to the obviously efficient dispersion of the hydrophilic GO in the by the water dispersible CNF/TCNF fibers and its subsequent formation of a homogeneous compact film. Generally, higher interfacial polarization, termed as Maxwell-Wigner-Sillars (MWS) polarization, being the result of the improved interfacial connection between filler and polymers, governs the enhanced dielectric response. The ac conductivity shows the same trend as the dielectric constants, increasing with a larger amount of GO for cellulose matrices. At 1 MHz (to provide the real, intrinsic material properties, we compare the

values detected at the highest measured frequencies), the composite film showed an ac conductivity (CGO-3: $\sim 6.7 \times 10^{-4} \text{ S m}^{-1}$, TCGO-3: $\sim 14 \times 10^{-4} \text{ S m}^{-1}$). The larger amount of carboxylic groups present in TCGO-3 is responsible for the higher ϵ' and σ' values compared to CGO.

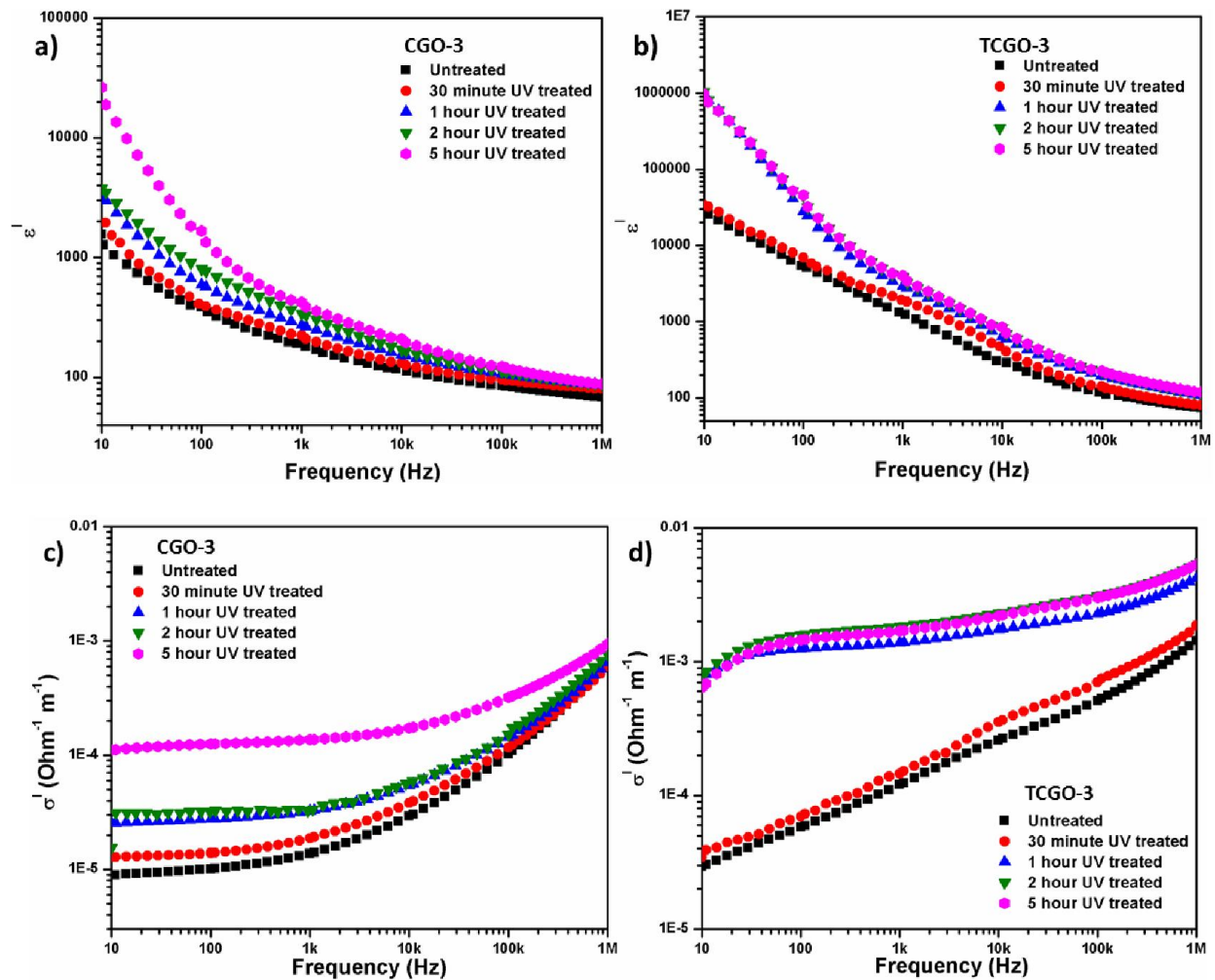


Fig. 5.10: Frequency dependence of the dielectric constant ϵ' (a, b) and ac conductivity σ' (c, d) at room temperature for untreated and 5 hours UV treated CGO-3 and TCGO-3.

The effect of UV radiation on the composites shows a time dependent increase of the dielectric constant ϵ' and the AC conductivity σ' for CGO-3 and TCGO-3 (Fig 5.10). After 1 hour of UV treatment, CGO-3 shows a significant increase of ϵ' (MHz) after 5 hours

of irradiation (ϵ' 1 MHz, 88.85. σ' 1 MHz 9.37×10^{-4}), TCGO-3, shows a gradual increase of ϵ' until 2 hours of UV treatment and displays an abrupt increment after 5 hours of treatment at lower frequency (ϵ' 1 MHz, 112.61. σ' 1 MHz $53 \times 10^{-4} \text{ S m}^{-1}$). The UV treated films show an enhanced dielectric response since reduced GO provides more sites for MWS polarization. The distance between the filler particles is sufficiently large in the case of untreated CGO/TCGO because of the relatively low concentration (3 wt.%) of fillers. UV irradiation induced reduction of graphene oxide, decreases this distance which leads to a higher capacitance i.e., a high dielectric constant. After reduction, graphene sheets with higher intrinsic conductivity are present causing the increase in AC conductivity.

5.6 Electrochemical properties

To analyze the impact of reduction, finally, we explored the electrochemical properties of untreated and 5 hours UV treated CGO-3 and TCGO-3 using the cyclic voltammetry (CV) and electrochemical impedance spectroscopy (EIS). The symmetric and appropriate rectangular CV curves (Fig.5.11) of composite electrodes indicate a capacitive behavior. The intense cathodic peak observed at $\sim -0.45 \text{ V}$ vs Ag/AgCl for TCGO-3 are related to faradaic redox reactions between oxygen related functional groups and the electrolyte [14]. The charge carrying capacity of the composite electrodes for the given voltage range can be due to the large surface of electrodes, which effectively permits the electron transfer. EIS measurements were performed in order to evaluate the charge transfer (and consequently resistance) and/or diffusion processes involved when the materials are immersed in a 1 M H_2SO_4 electrolyte.

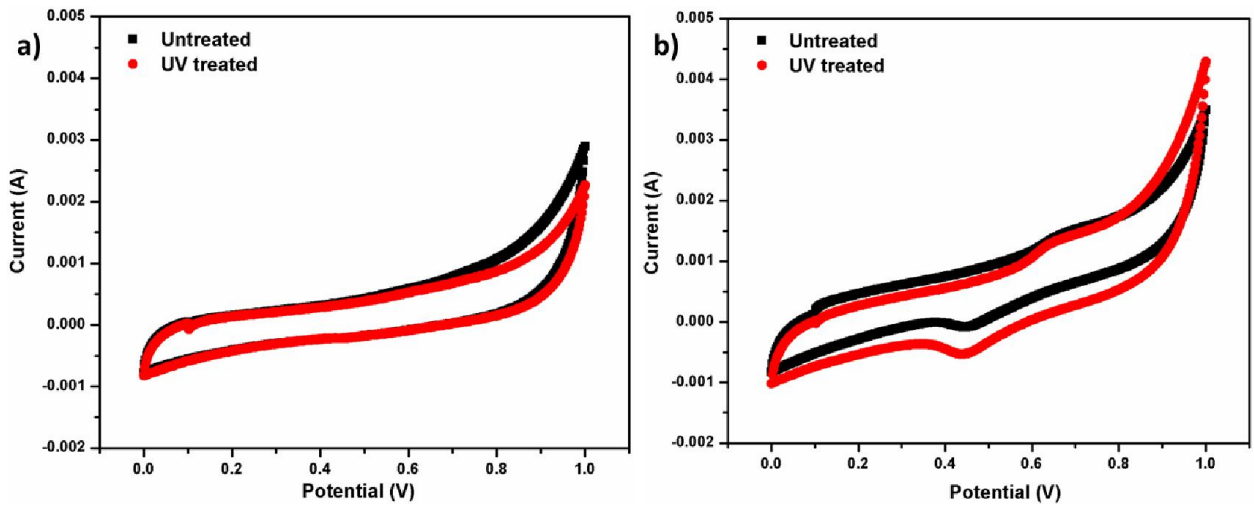


Fig. 5.11: Cyclic voltammetry of untreated and 5 hours UV treated CGO-3 (a) and TCNG-3 composite films with a scan rate of 100 mVs^{-1} .

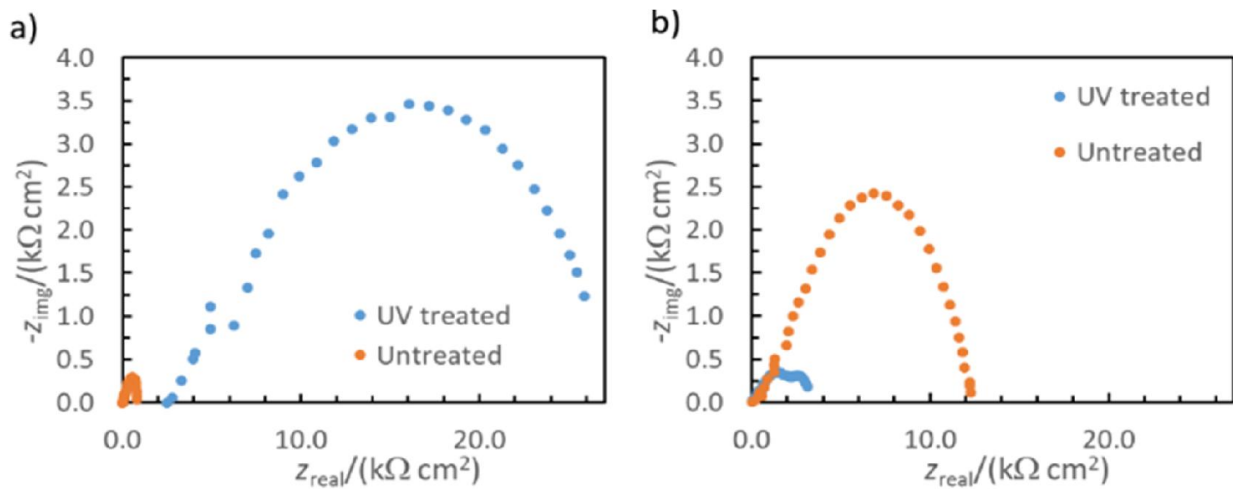


Fig. 5.11: Nyquist spectra of a) CGO-3 and UV treated CGO, and b) TCGO-3 and UV treated TCGO-3 after 1 h of immersion in $1 \text{ M H}_2\text{SO}_4$.

Fig. 5.12.a shows a Nyquist spectra for the untreated and UV treated CGO-3, which demonstrates that the resistance of the UV treated CGO-3 increases compared to the untreated CGO-3. The shape of the Nyquist spectra for both CGO-3 suggest a

kinetically-controlled process involving charge transfer resistance and double layer capacitance, but no diffusion present, as the curve is not deviating at 45° relative to the x -axis (Z_{real} , is the real part of the impedance). On the other hand, UV treated TCGO-3 shows lower resistance compared to the untreated TCGO-3 as seen from the lower Z_{real} values (Fig. 5.12b). Moreover, in the case of UV treated TCGO-3 the shape of the Nyquist spectrum shows two semicircles, implying two processes – it might happen that beside charge-transfer there is also diffusion through a finite layer thickness (represented by the O element, sometimes called the Porous bounded Warburg element). The impedance response for the finite layer thickness diffusion O is:

$$Z_D = Z_O(j\omega)^{-0.5} \tanh[B(j\omega)^{0.5}] \text{ where } B = d \sqrt{(1/D_f)}$$

and the impedance $Z_O = 1/Y_O$ (Y – admittance), D_f is the diffusion of ions, and d is the surface layer thickness or in this case film thickness. B characterizes the time it takes for ions to diffuse through this layer. By taking into account this explanation, we can conclude that UV treated TCGO-3 is under kinetic- and diffusion-controlled processes, whereas untreated TCGO-3 is only under a kinetically controlled process. Moreover, the good reduction efficiency of GO in the treated TCGO-3 composites compared to treated CGO-3 would be the reason for its improved properties than later one.

5.7 Conclusion

Self-standing films were fabricated from native (CGO) and TEMPO oxidized cellulose (TCGO) nano-fibrils containing a maximum of 3 weight percent graphene oxide.

UV light exposure in a nitrogen atmosphere induces the reduction of graphene oxide to graphene which was confirmed by colour changes, ATR-FTIR, UV-Visible spectroscopy and charge titration. The reduction of graphene is assumed to be caused by the formation of radicals and reducing species upon irradiation of cellulose. An increase in the mechanical storage modulus of the composites is observed after the photoreaction. After 5 hours of UV irradiation the dielectric properties of CGO and TCGO are drastically enhanced. The dielectric constants at 1 MHz frequency increase from 68.92 to 88.85 for CGO and 74.05 to 121.61 for TCGO after reduction filled with three percent graphene oxide. The AC conductivity is also significantly enhanced after reduction from $6.7 \times 10^{-4} \text{ S m}^{-1}$ to $9.37 \times 10^{-4} \text{ S m}^{-1}$ for CGO and $14 \times 10^{-4} \text{ S m}^{-1}$ to $53 \times 10^{-4} \text{ S m}^{-1}$ for TCGO filled with three percent graphene oxide.

The symmetric and rectangular CV curves of electroded fabricated from the composite materials indicate a capacitive behavior. Electrochemical impedance spectroscopy measurements show that the untreated and UV treated CGO, and untreated TCGO samples are under kinetically-controlled processes, whereas UV treated TCGO might be under kinetic- and diffusion-controlled processes. Moreover, a Nyquist spectra demonstrates that untreated CGO is less resistive (charge transfer can occur faster) than the UV treated CGO, whereas UV treated TCGO has a lower resistance compared to the untreated TCGO. Overall the presented method of UV induced graphene oxide reduction in a matrix of cellulose provides an alternative to hazardous wet chemical processes and can potentially be extended to other combinations of filler and polymer matrix. Investigations into the exact mechanism of reduction are a target and necessity of further research.

5.8 References

1. Wu, Chao, et al. "Graphene oxide-encapsulated carbon nanotube hybrids for high dielectric performance nanocomposites with enhanced energy storage density." *Nanoscale* 5.9 (2013): 3847-3855.
2. Mohiuddin, Md, et al. "Flexible cellulose acetate/graphene blueprints for vibrotactile actuator." *RSC Advances* 5.43 (2015): 34432-34438.
3. Chen, Zhe, et al. "Achieving large dielectric property improvement in polymer/carbon nanotube composites by engineering the nanotube surface via atom transfer radical polymerization." *Carbon* 95 (2015): 895-903.
4. Tong, Wangshu, et al. "Achieving significantly enhanced dielectric performance of reduced graphene oxide/polymer composite by covalent modification of graphene oxide surface." *Carbon* 94 (2015): 590-598.
5. Luo, Bingcheng, et al. "Synthesis, characterization and dielectric properties of surface functionalized ferroelectric ceramic/epoxy resin composites with high dielectric permittivity." *Composites Science and Technology* 112 (2015): 1-7.
6. Ning, Nanying, et al. "Tailoring Dielectric and Actuated Properties of Elastomer Composites by Bioinspired Poly (dopamine) Encapsulated Graphene Oxide." *ACS applied materials & interfaces* 7.20 (2015): 10755-10762.
7. Peng, Hongdan, et al. "Simultaneous reduction and surface functionalization of graphene oxide by natural cellulose with the assistance of the ionic liquid." *The Journal of Physical Chemistry C* 116.30 (2012): 16294-16299.
8. Sadasivuni, Kishor Kumar, et al. "Transparent and flexible cellulose nanocrystal/reduced graphene oxide film for proximity sensing." *Small* 11.8 (2015): 994-1002.

9. Dang, Luong Nguyen, and Jukka Seppälä. "Electrically conductive nanocellulose/graphene composites exhibiting improved mechanical properties in high-moisture condition." *Cellulose* 22.3 (2015): 1799-1812.
10. Luong, Nguyen Dang, et al. "Graphene/cellulose nanocomposite paper with high electrical and mechanical performances." *Journal of Materials Chemistry* 21.36 (2011): 13991-13998.
11. Ouyang, Wenzhu, et al. "Scalable preparation of three-dimensional porous structures of reduced graphene oxide/cellulose composites and their application in supercapacitors." *Carbon* 62 (2013): 501-509.
12. Sadasivuni, Kishor Kumar, et al. "Reduced graphene oxide filled cellulose films for flexible temperature sensor application." *Synthetic Metals* 206 (2015): 154-161.
13. Yan, Chaoyi, et al. "Highly stretchable piezoresistive graphene–nanocellulose nanopaper for strain sensors." *Advanced materials* 26.13 (2014): 2022-2027.
14. Nandgaonkar, Avinav G., et al. "A one-pot biosynthesis of reduced graphene oxide (RGO)/bacterial cellulose (BC) nanocomposites." *Green Chemistry* 16.6 (2014): 3195-3201.
15. Tian, Mingwei, et al. "Enhanced mechanical and thermal properties of regenerated cellulose/graphene composite fibers." *Carbohydrate polymers* 111 (2014): 456-462.
16. Becerril, Héctor A., et al. "Evaluation of solution-processed reduced graphene oxide films as transparent conductors." *ACS nano* 2.3 (2008): 463-470.
17. Jorio, A., et al. "Raman Spectroscopy in Graphene Related Systems, Swiley." (2011).

18. Ferrari, Andrea C., and Jf Robertson. "Interpretation of Raman spectra of disordered and amorphous carbon." *Physical review B* 61.20 (2000): 14095.
19. Beeran, Yasir, et al. "Mechanically strong, flexible and thermally stable graphene oxide/nanocellulosic films with enhanced dielectric properties." *RSC Advances* 6.54 (2016): 49138-49149.
20. Popescu, Carmen-Mihaela, et al. "Vibrational spectroscopy and X-ray diffraction methods to establish the differences between hardwood and softwood." *Carbohydrate Polymers* 77.4 (2009): 851-857.
21. Kleinert, Theodor N. "Free radical reactions in UV irradiation of cellulose." *Holzforschung-International Journal of the Biology, Chemistry, Physics and Technology of Wood* 18.1-2 (1964): 24-28.
22. Zhang, Hao, et al. "Regenerated-Cellulose/Multiwalled-Carbon-Nanotube Composite Fibers with Enhanced Mechanical Properties Prepared with the Ionic Liquid 1-Allyl-3-methylimidazolium Chloride." *Advanced Materials* 19.5 (2007): 698-704.
23. Kafy, Abdullahil, et al. "Designing flexible energy and memory storage materials using cellulose modified graphene oxide nanocomposites." *Physical Chemistry Chemical Physics* 17.8 (2015): 5923-5931.
24. Liao, Wei-Hao, et al. "Effect of octa (aminophenyl) polyhedral oligomeric silsesquioxane functionalized graphene oxide on the mechanical and dielectric properties of polyimide composites." *ACS applied materials & interfaces* 6.18 (2014): 15802-15812.

25. Chen, Yao, et al. "High performance supercapacitors based on reduced graphene oxide in aqueous and ionic liquid electrolytes." *Carbon* 49.2 (2011): 573-580.

Chapter 6

Structure, morphology, dielectric and electrochemical storage properties of thermally reduced graphene oxide (RGO) filled cellulose nanofibrils based xerogels and cryogels

6.1 Introduction

In this study, reduced graphene oxide (RGO) sheets and cellulose nanofibrils (CNF) in various ratios were used to prepare a film-based xerogel and a pore-oriented cryogel composites by vacuum filtration and one-directional freezing, respectively. CNFs was used as a biodegradable matrix material due to their light weight nature, low price, huge mechanical strength (200-400 MPa) and Young's modulus (7.4-14 GPa), as well as lower thermal expansion coefficient (12-28.5 ppm/K) [16, 17]. The composites were characterized by X-ray diffraction (XRD) and Fourier Transform Infrared (FTIR) spectroscopy's. The temperature dependence of dielectric properties using different frequencies (100 Hz, 1 KHz, 10 KHz, 100 KHz and 1 MHz) were systematically studied. The samples were compared related to their electrochemical charge storage properties evaluated by cyclic voltammetry (CV) and electrochemical impedance spectroscopy (EIS).

6.2 Chemical and structural characterization of the composites

Figure 6.1 shows the synthesis routes and schematic representation of RGO filled CNF composites by air and vacuum.

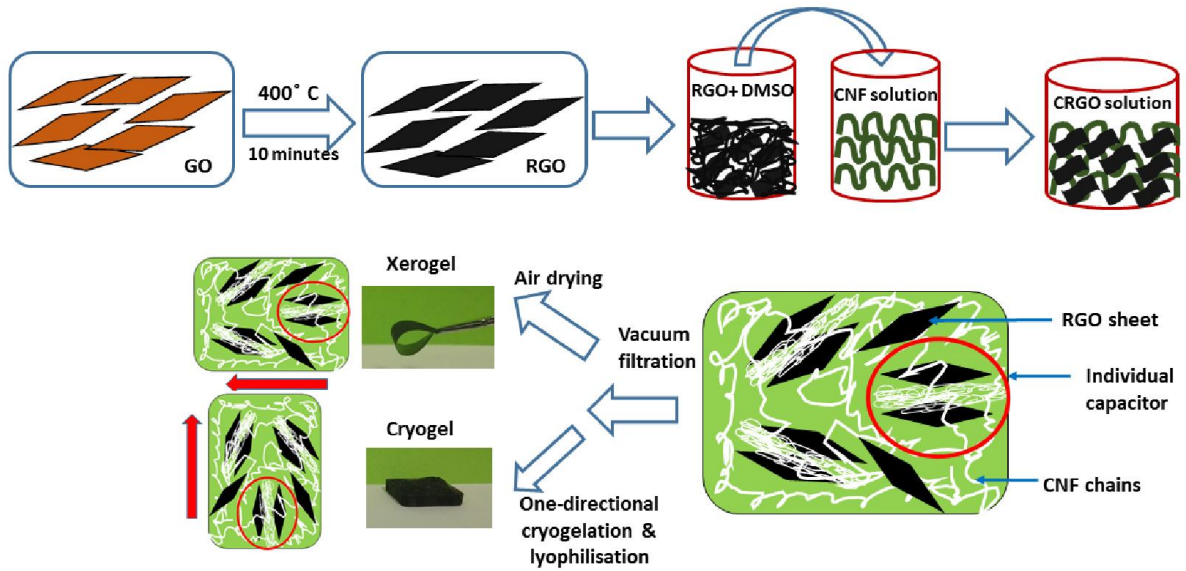


Fig. 6.1 The schematic representation of the fabrication of composite by air (xerogels) vs. vacuum (cryogels) drying.

The composite films prepared by xerogelation were investigated related to the structure, crystallinity and functional properties using XRD and FTIR spectroscopy's. Fig. 6.2a) displays the XRD patterns of CNF and various CRGO composites giving the information about the dispersion of RGO in a nanocellulose matrix. The CNF-based paper exhibit three diffraction peaks at 2θ of 15.1° , 16.8° and 22.6° corresponding to the reflections of (10-1), (101) and (020) of the cellulose I allomorph [1], respectively. All CRGO composites exhibits similar diffraction peaks to that one of CNF paper, indicating on excellent dispersion of RGO sheets in nanocellulose matrix. In addition, the intensity of diffraction peaks is enhanced with respect to the increasing of RGO, indicating on the improvement in the crystallinity for CRGO films.

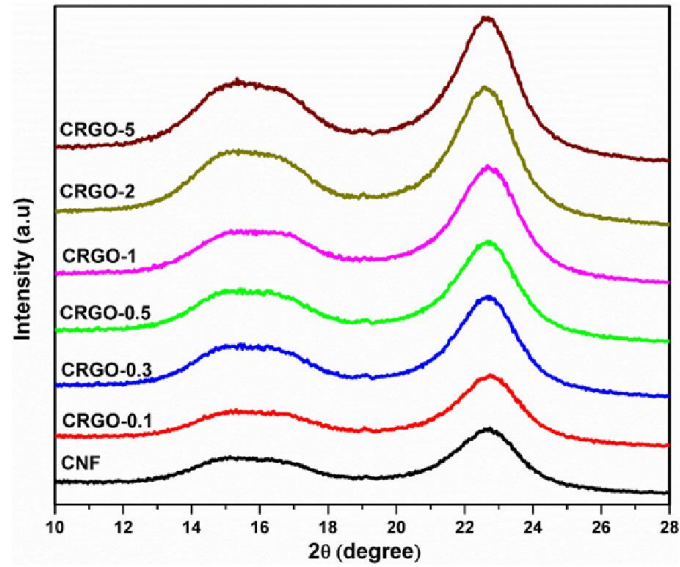


Fig. 6.2. XRD patterns of CNF and CRGO xerogel composites.

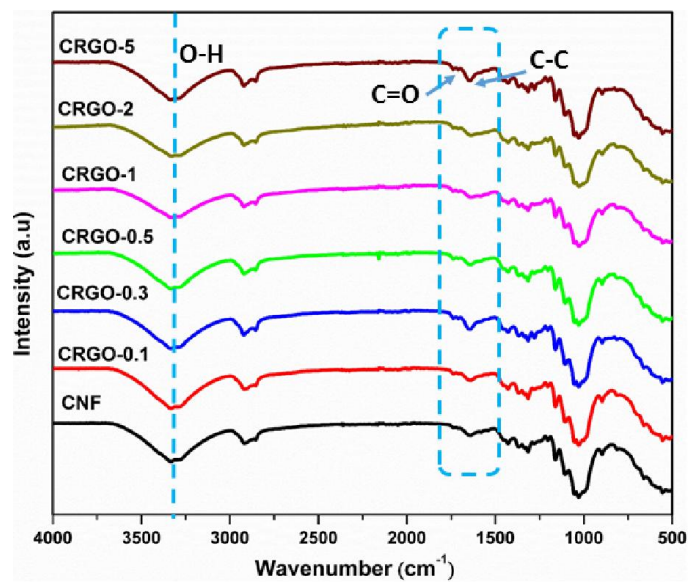
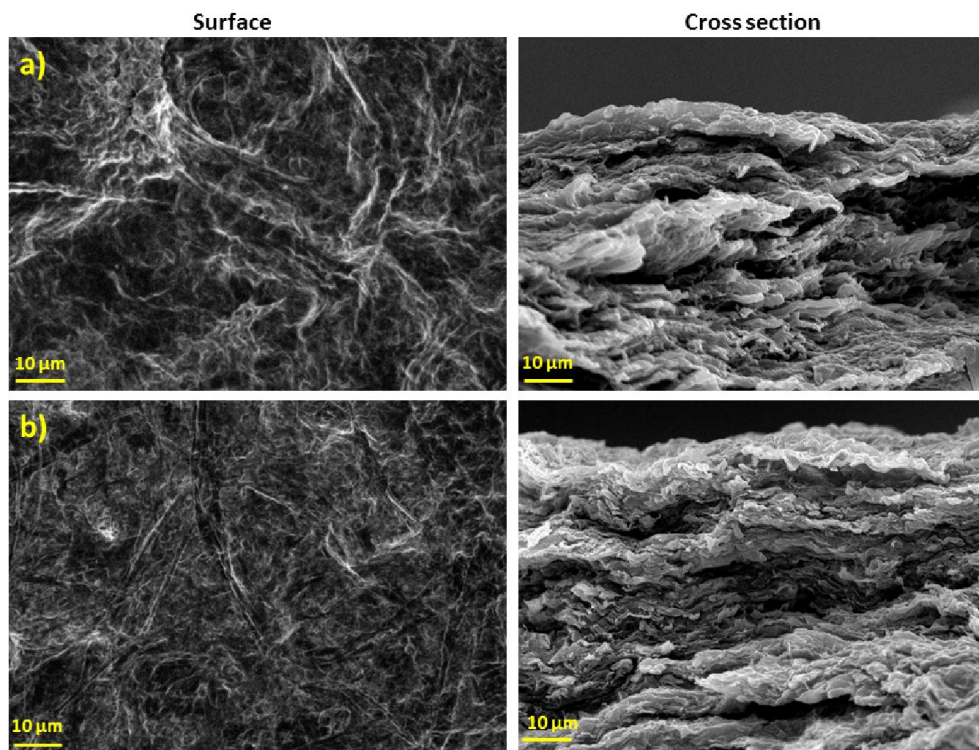


Fig. 6.3. ATR-FTIR spectra of CNF and CRGO xerogel composites.

The characteristic **FTIR spectra** (Fig. 6.3) presented typical cellulose peaks at $\sim 3335 \text{ cm}^{-1}$, $\sim 2920 \text{ cm}^{-1}$, $\sim 1318 \text{ cm}^{-1}$, $\sim 1160 \text{ cm}^{-1}$, $\sim 1023 \text{ cm}^{-1}$, $\sim 1028 \text{ cm}^{-1}$ for CNF film [2]. The observed peak at 1640 cm^{-1} is assigned to the C=O stretching. The CRGO film composites also showing typical IR bands of CNF at around 3335 cm^{-1} , $\sim 2920 \text{ cm}^{-1}$, $\sim 1318 \text{ cm}^{-1}$, $\sim 1160 \text{ cm}^{-1}$, $\sim 1023 \text{ cm}^{-1}$, \sim

1028 cm^{-1} confirming the better dispersion of RGO sheets in the cellulose matrix. The peaks at $\sim 1315 \text{ cm}^{-1}$ and $\sim 1641 \text{ cm}^{-1}$ corresponding to the O-H stretching, C-O-H bending vibrations respectively [2]. The C=O stretching vibrations observed at around 1740 cm^{-1} , giving the information on the hydrogen bonding interactions between the remaining carboxyl groups of RGO with in the CRGO films. The shifting of some peak positions at around 3335 cm^{-1} and 1641 cm^{-1} , assigned to the O-H and C-C rings of graphene, to sharper in the case of CRGO samples, especially CRGO-3 film sample, attributing to the synergistic effect.



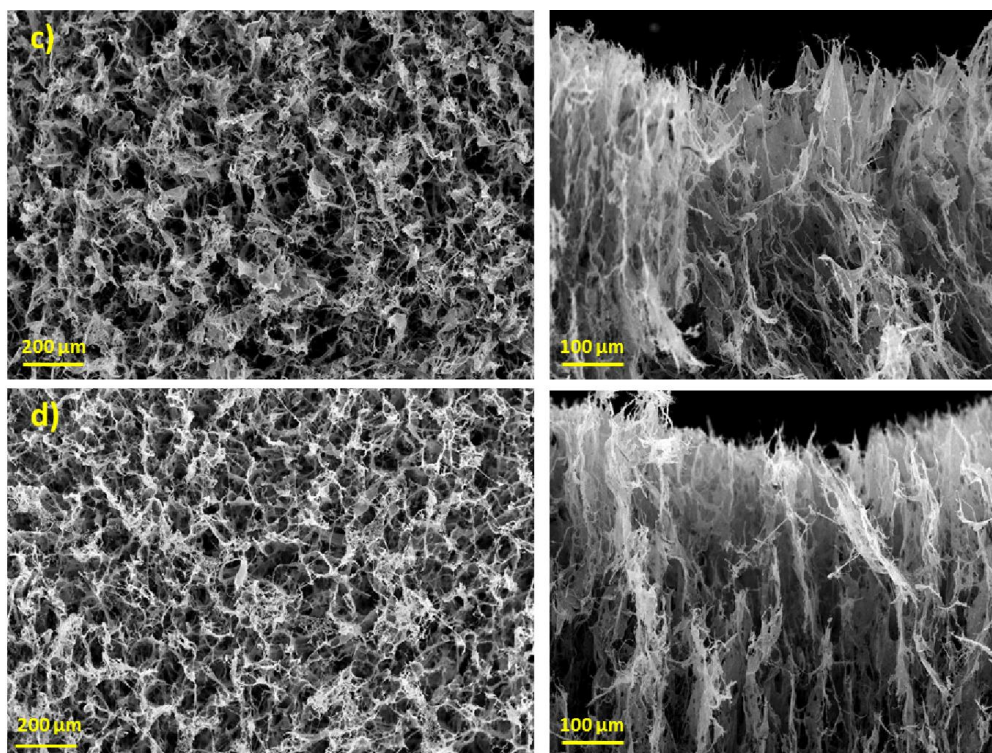


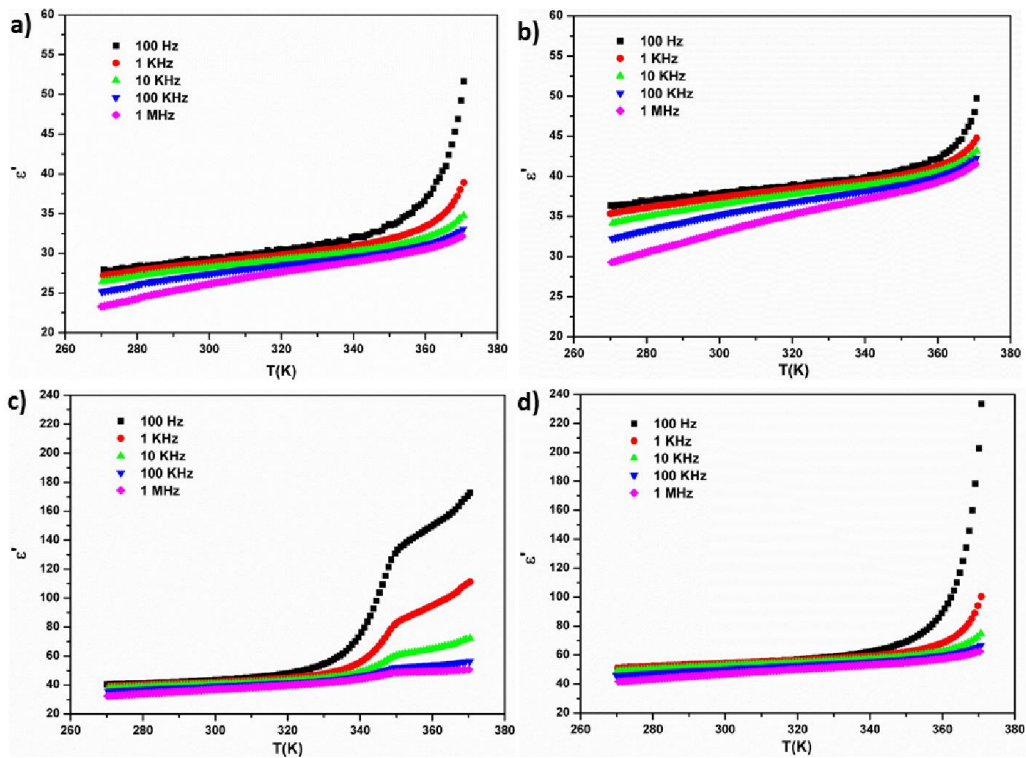
Fig. 6.4: SEM images of surfaces and cross-sections of a) CRGO-0.3% and b) CRGO-5% xerogels, and CRGO-5% cryogels prepared by one-directional freezing at c) -50°C and d) -80°C , respectively.

The surface and cross-section imaging of composites prepared by different approaches (xero- and cryo-gelation) were performed by SEM (Fig. 6.4) to indicate their influence on the morphological structure and RGO sheets dispersion into the nanocellulose matrix. While the surface and the cross-section of the $80\pm 2\ \mu\text{m}$ thick CRGO film-like xerogels with the lowest concentration (0.3%) of RGO is relatively cloudy, the CRGO xerogels with the highest (5 wt%) RGO content clearly disclose denser and layered structure indicating on orientation of cellulose nanofibrils along the RGO sheets as well as on high adhesion between them. Generally, RGO sheets tend to align parallel in the matrix of a composite film [2 and 3]. On the other hand, the

2±01 mm thick cryogen-prepared samples with 5 wt% of RGO content (CRGO-5) resulted to well-oriented but micro-porous networks with less dense nature, being more significant at cryogel prepared at -50 °C (have the pore diameter of 54±3 μm) than at -80 °C (have the pore diameter of 17±2 μm) due to slower freezing kinetic of the water molecules and thus creation of larger ice crystals at the contact points, where cryogelation occurs [4, 5].

6.3 Temperature dependent dielectric properties of CRGO film-like xerogels

Figs. 6.5 and 6.6 shows the temperature dependent dielectric constants (ϵ') and ac electrical conductivities (σ') of CRGO xerogel samples measured at frequencies of 100 Hz, 1 kHz, 10 kHz, 100 kHz and 1 MHz.



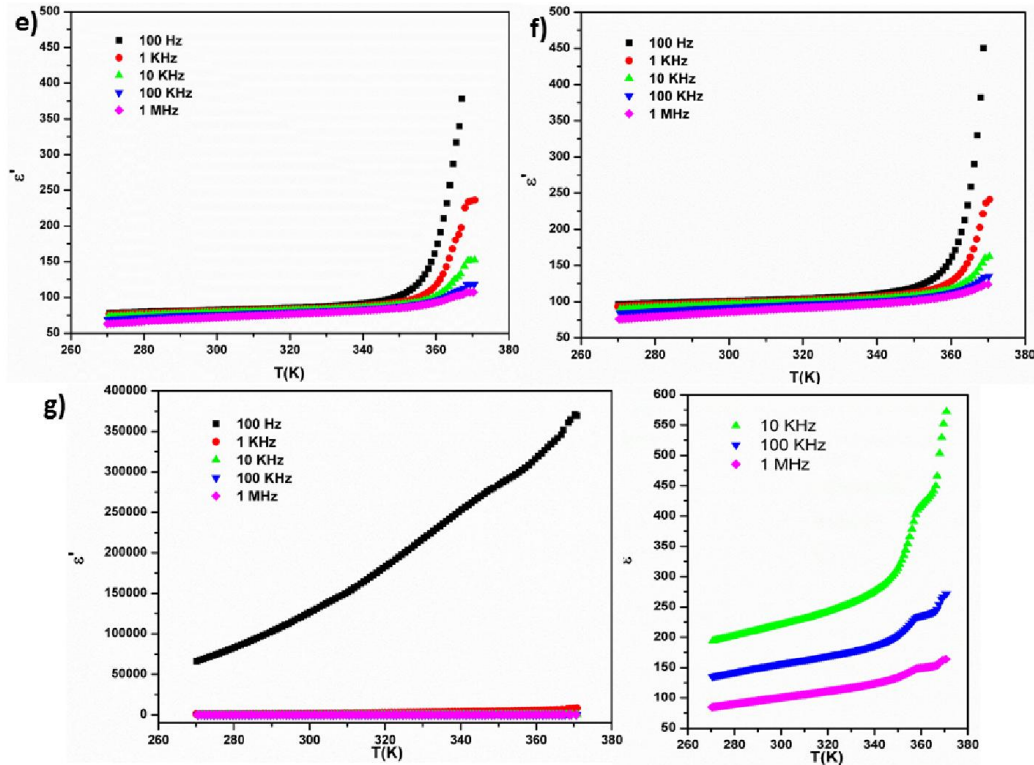
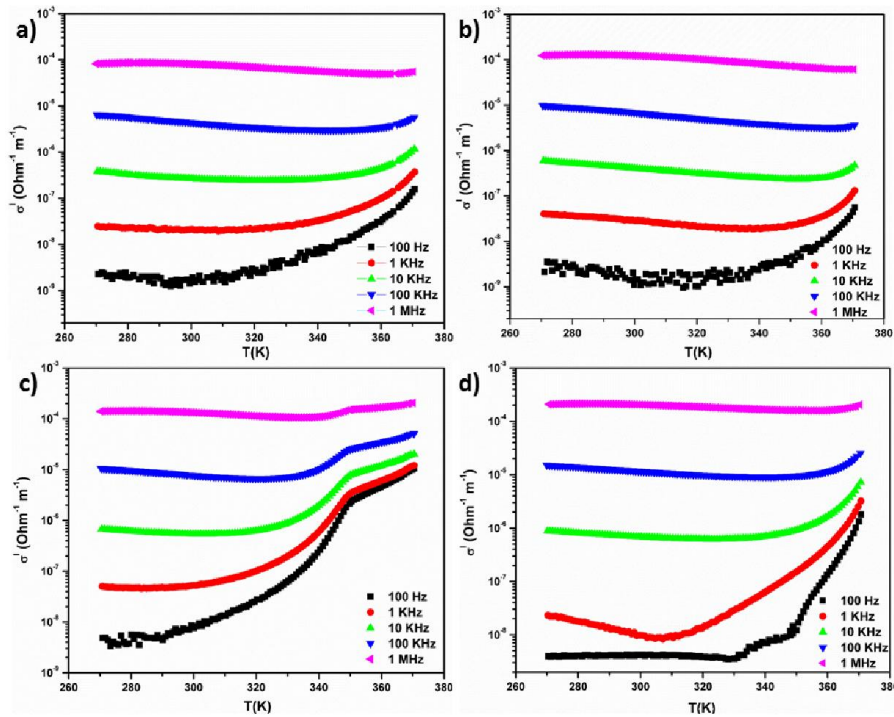


Fig. 6.5 Temperature dependence of the dielectric constant for a) CNF, b) CRGO-0.1, c) CRGO-0.3, d) CRGO-0.5, e) CRGO-1, f) CRGO-2 and g) CRGO-5, measured at various frequencies.

The dielectric behaviour of CRGO samples is strongly frequency- and temperature-dependent, and displays a gradual increment from 0.1% to 5% of RGO admixture. Both, ϵ^1 and ac electrical conductivity reach very high values for CRGO-5% composite, which can be explained in terms of the Maxwell–Wagner–Sillars (MWS) process, where the addition of more RGO sheets into the CNF matrix provides enormous spots for interfacial polarization, being however related to the mechanism and intensity of interaction between RGO sheets and CNFs. Both components act as microcapacitor electrodes and a corresponding dielectric, respectively, thus forming the entire CRGO composite (as shown in Fig. 6.1) as a huge microcapacitor network [6]. At low RGO loading, the capacitance of each microcapacitor is low because of the large distance between graphene sheets, while it increases at high RGO loading due to the reduced distance between them.

The dielectric constant, which is a measure of energy storage ability of a material, decreases with frequency for all investigated composites. Some reports showing similar tendency for RGO and cadmium selenide nanoparticles [7, 8]. In general, the dielectric constant values showing an increment at lower frequency region owing to the space charge contribution. Moreover, some external effects like surface layers, often govern the dielectric response at low frequencies [9]. Therefore, to provide intrinsic material properties, it is necessary to compare values observed at the highest frequencies. Fig. 7 thus shows the evolution of the dielectric constant on increasing RGO content, detected at 1 MHz, at low (270 K) and high (370 K) temperatures, indicating that CRGO film-like composite can be suggested as a suitable candidate for high temperature dielectric applications [10].



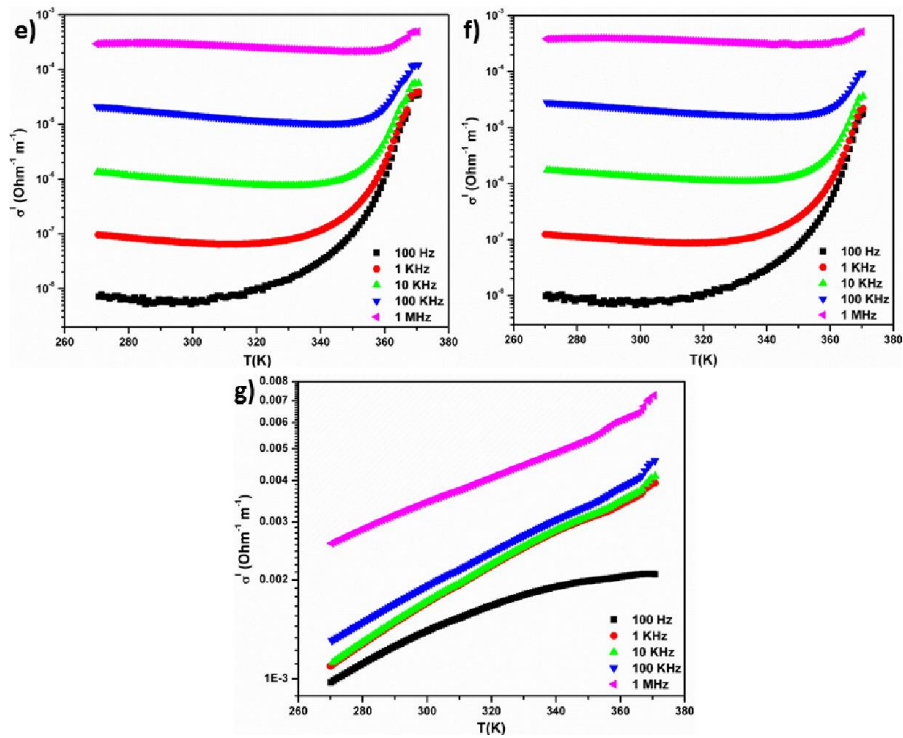


Fig.6.6 Temperature dependence of the ac electrical conductivity for a) CNF, b) CRGO-0.1, c) CRGO-0.3, d) CRGO-0.5, e) CRGO-1, f) CRGO-2 and g) CRGO-5, measured at various frequencies.

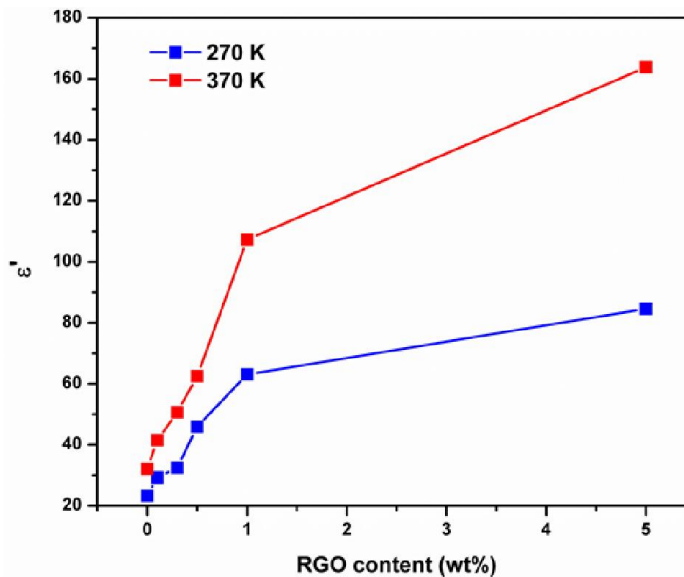


Fig. 6.7. Evolution of dielectric constant at frequency of 1 MHz for CRGO film-like xerogel composites with different content of RGO.

The ac electrical conductivity of CRGO samples (Fig. 6) increases with both, temperature and frequency. Moreover, it also increases with higher RGO content, which may be the result of the tunnelling of charge carriers across the interface and thermionic emission. For the CRGO-5% sample this effect is even more visible, resulting in the highest conductivity of around 0.0074 S/m at 370 K. It is evident that ac electrical conductivity of all samples increases with increasing temperature as well as the dielectric constant. In detail, the ϵ^1 starts abruptly to increase in the temperature range of ~340-370 K. This exponential increment at high temperatures may be due to the special crystal structure and/or the presence of water molecules in CRGO composites. At ~370 K, close to the boiling point of water, the ϵ^1 value reaches the maximum also due to increased interfacial polarization. The similar trend of temperature dependence of cellulose electro active film from low (-133 °C) to high (200 °C) temperature region, as well as the dielectric constant increasing from 7 °C (280 K) to 105 °C (378 K) for a frequency range of 100 Hz to 1 MHz, is reported by Yun et al. [11]. On the other hand, a decreasing trend of ϵ^1 are reported by increasing temperature for cellulose- hexamethylene-1,6-diisocyanate-modified GO composites [12]. In the present study, the mobility of charge carriers and the cellulose dipole chains obviously improves at higher temperatures. The CRGO-5% film-like xerogel is further electrochemically investigated to explore the energy storage properties and compare to its cryogel counterparts prepared at -50 °C and -80 °C, respectively.

6.4 Electrochemical charge storage properties of film-like xerogels and porous cryogels

Cyclic voltammetry (CV) measurements were performed for the CRGO-5 composites prepared by xero- and cryo-gelation, to categorize the charge storage mechanism in an electrolyte of 1 M H₂SO₄.

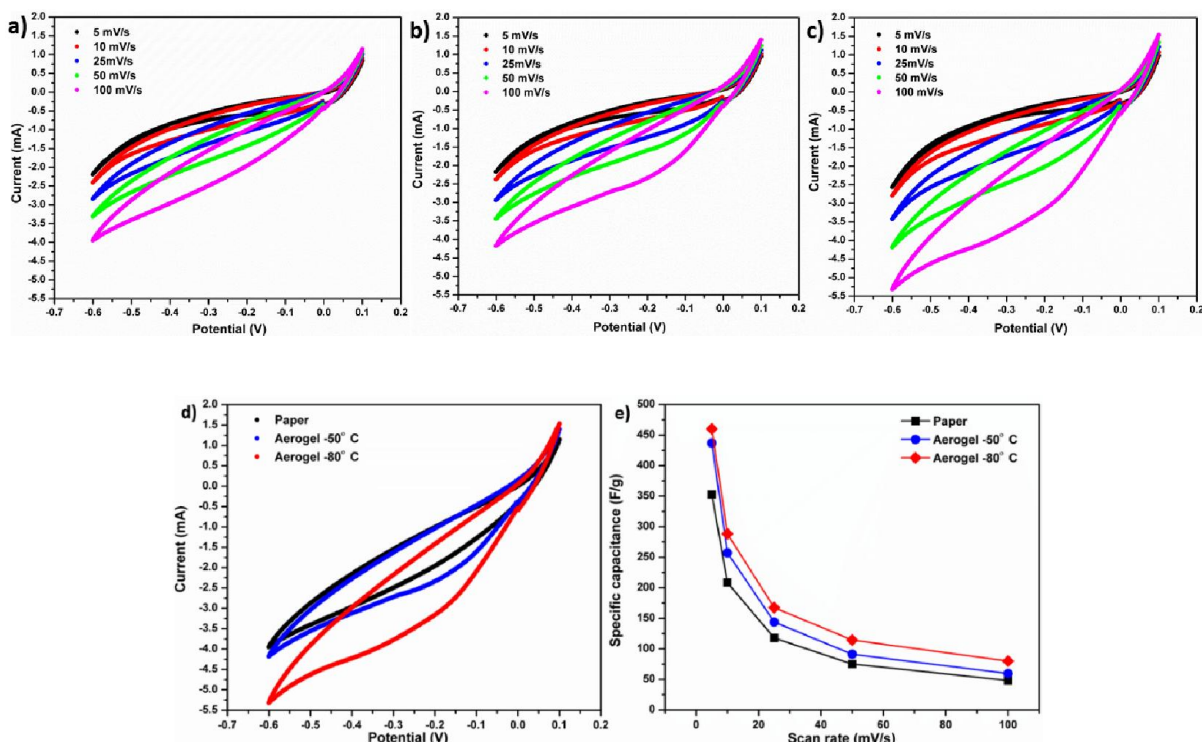


Fig. 6.8 Cyclic voltammograms of the CRGO-5 composites prepared as a) film-like xerogels as well as cryogels at b) -50°C and c) -80°C at different scan rates, and d) all composites at the scan rate of 100 mV/s , in $1\text{ M H}_2\text{SO}_4$. e) Specific capacitance of the composites at different scan rates.

As shown in Fig. 6.8, the CV tests were recorded for different scan rates. The near rectangular shape of CV curves of the electrodes indicating their charge storage ability and capacitive nature. The superior electrochemical performance was observed in the case of cryogel sample prepared at -80°C (Fig. 6.8d). This would be accredited to the effect of both smaller pores (~ 54 vs. $\sim 17\ \mu\text{m}$) and thus high surface area compared with the cryogel sample prepared at -50°C in addition with the pores orientation. The vertical alignment of pores in the cryogels along the thickness of the sample allowing easier electrolyte diffusion and flow through the material (Fig.

1). The specific capacitance of all samples acting as electrodes was calculated with respect to different scan rates by the following equation:

$$C = \frac{1}{m \nu} \int_{V^-}^{V^+} I dV \quad (3)$$

where C is the specific capacitance in F/g, m is the mass (g) of the electrode material, V is the applied potential difference, and ν is the scan rate in m V/s, and compared (Fig 6.8e). The maximum specific capacitance was detected at a scan rate of 5 mV/s in case of all the samples. At lower scan rates, the electrolyte ions have enough time to pass through the pores of the material than at higher scan rates therefore, resulted to an increase in specific capacitance. Cryogel sample prepared at -80°C thus yielded a specific capacitance of ~ 460 F/g, while sample prepared at -50°C and xerogel sample achieved a specific capacitance of ~ 437 F/g and ~ 353 F/g, respectively, at 5 mV/s. Such an improved value of specific capacitance indicated on an outstanding performance of this cryogel sample, being even higher than reported findings for other cellulose-graphene composites [13-16]. Flexible graphene-cellulose paper electrode fabricated by Weng *et al* [13] showed a capacitance per geometric area of 81 mF/cm^2 while graphene filled cellulose fibres as a flexible double layer supercapacitor displays a capacity of 252 F/g at a current density of 1 A/g [14]. Ouyang *et al* [15] fabricated 3D graphene filled cellulose aerogels with a specific capacitance of 71.2 F/g whereas CNF–RGO hybrid aerogel based flexible supercapacitor reported by Gao *et al* [16] having a capacitance of 207 F/g.

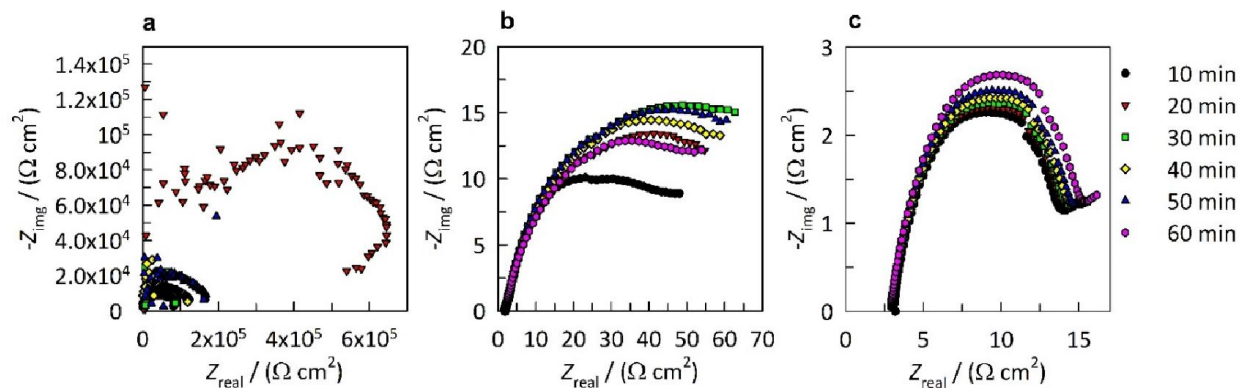


Fig. 6.9 Nyquist plots measured for the CRGO-5 composites prepared as a) film-like xerogels as well as cryogels at b) $-50\text{ }^{\circ}\text{C}$ and c) $-80\text{ }^{\circ}\text{C}$, after 10–60 min of immersion in 1 M H_2SO_4 .

For the developed electrode materials, it is desired to obtain the lowest resistance (fast electron transfer) to store maximal amount of charge. Therefore, the electrochemical performances of all CRGO-5 based samples were used as electrodes for studying by electrochemical impedance spectroscopy followed at different immersion time periods (Fig. 9). The film-like electrode (Fig. 9a) shows high resistance in the range of 100–500 $\text{k}\Omega\text{ cm}^2$, which was notable on the Nyquist spectra in the real part of the impedance by imaginative extrapolation of the loop to the x-axis, and being related to the dense and components- vertically-to-flow aligned structure (Fig 1). In comparison, cryogel prepared at $-50\text{ }^{\circ}\text{C}$ shows significantly lower resistive behaviour within the range of 50–60 $\Omega\text{ cm}^2$ (Fig. 9b), where the shape of the Nyquist spectra might indicate on a presence of diffusion process as the curves deviate from the x-axis at the highest Z_{real} values (the loop does not tend to curve to the x-axis). On the other hand, the resistive behaviour of the cryogel prepared at $-80\text{ }^{\circ}\text{C}$ was 3-4 times lower as seen in Fig. 9c. Moreover, it is well observable that even after 10 min of immersion in electrolyte, the cryogel samples started to show less resistive performance and hasn't degraded during the immersion time (60 min), being related to the

composite pore-structure and orientation (Fig 1). In case of degradation, the resistive and capacitive behaviour of the material would significantly change and impedance spectra *vs.* time would differ significantly. It can be concluded that 17 μm -porous CRGO-5 cryogel prepared at -80 °C has lower electrochemical resistance behaviour to exchange electrons with the electroactive species in electrolytic solution than 54 μm -porous counterprice or dense film-like xerogel, acting as an electrode. This indicates that the capacitive behaviour of low-porous CRGO-5 composite cryogel is much better than other electrodes. These findings are in good agreement with the specific capacitance values from cyclic voltammetry measurements. The relatively smaller and with electrolyte-flow oriented pores of cryogel sample results to an improved electron transfer and lower electrochemical resistance compared to other electrode samples of the same composition.

6.6 Conclusion

Reduced graphene oxide (RGO) incorporated into the cellulose nanofibrils (CNF) matrixes were fabricated as a dense xerogel and well-aligned micro-porous cryogels, and evaluated related to the dielectric properties and electrochemical storage capacity. The xerogel composites show significant improvement in dielectric properties with respect to the temperature and frequency by increasing of the RGO loading. The xerogel with 5 wt% content of RGO thus showed outstanding dielectric performance and ac electrical conductivity. All the materials being used as an electrode, showed capacitive nature with nearly rectangular shape of cyclic-voltammetry curves. The cryogel with relatively smaller and aligned porosity as well as higher surface area exhibited less electrochemical resistance and more capacitive nature than other samples of the same (5 wt%) RGO content. High flexibility of film-like xerogel sample make it promising candidate as highly-performing dielectric materials for energy storage applications, while porous and light cryogel shows high electrochemical resistance and capacitive performance which however depends on the bulk structure of the samples.

References

1. Oh, Sang Youn, et al. "Crystalline structure analysis of cellulose treated with sodium hydroxide and carbon dioxide by means of X-ray diffraction and FTIR spectroscopy." *Carbohydrate Research* 340.15 (2005): 2376-2391.
2. Beeran, Yasir, et al. "Mechanically strong, flexible and thermally stable graphene oxide/nanocellulosic films with enhanced dielectric properties." *RSC Advances* 6.54 (2016): 49138-49149.
3. Luong, Nguyen Dang, et al. "Graphene/cellulose nanocomposite paper with high electrical and mechanical performances." *Journal of Materials Chemistry* 21.36 (2011): 13991-13998.
4. Liapis, A. I., M. L. Pim, and R. Bruttini. "Research and development needs and opportunities in freeze drying." *Drying technology* 14.6 (1996): 1265-1300.
5. Kiani, Hossein, and Da-Wen Sun. "Water crystallization and its importance to freezing of foods: A review." *Trends in Food Science & Technology* 22.8 (2011): 407-426.
6. Wu, Chao, et al. "Graphene oxide-encapsulated carbon nanotube hybrids for high dielectric performance nanocomposites with enhanced energy storage density." *Nanoscale* 5.9 (2013): 3847-3855.
7. Wen, Bo, et al. "Reduced graphene oxides: light-weight and high-efficiency electromagnetic interference shielding at elevated temperatures." *Advanced Materials* 26.21 (2014): 3484-3489.
8. Suresh, S., and C. Arunseshan. "Dielectric properties of cadmium selenide (CdSe) nanoparticles synthesized by solvothermal method." *Applied Nanoscience* 4.2 (2014): 179-184.

9. Lunkenheimer, P., et al. "Origin of apparent colossal dielectric constants." *Physical Review B* 66.5 (2002): 052105.
10. Ponpandian, N., P. Balaya, and A. Narayanasamy. "Electrical conductivity and dielectric behaviour of nanocrystalline NiFe₂O₄ spinel." *Journal of Physics: Condensed Matter* 14.12 (2002): 3221.
11. Yun, Gyu-Young, Joo-Hyung Kim, and Jaehwan Kim. "Dielectric and polarization behaviour of cellulose electro-active paper (EAPap)." *Journal of Physics D: Applied Physics* 42.8 (2009): 082003.
12. Kafy, Abdullahil, et al. "Designing flexible energy and memory storage materials using cellulose modified graphene oxide nanocomposites." *Physical Chemistry Chemical Physics* 17.8 (2015): 5923-5931.
13. Weng, Zhe, et al. "Graphene–cellulose paper flexible supercapacitors." *Advanced Energy Materials* 1.5 (2011): 917-922.
14. Kang, Yan-Ru, et al. "Fabrication of electric papers of graphene nanosheet shelled cellulose fibres by dispersion and infiltration as flexible electrodes for energy storage." *Nanoscale* 4.10 (2012): 3248-3253.
15. Ouyang, Wenzhu, et al. "Scalable preparation of three-dimensional porous structures of reduced graphene oxide/cellulose composites and their application in supercapacitors." *Carbon* 62 (2013): 501-509.
16. Gao, Kezheng, et al. "Cellulose nanofiber–graphene all solid-state flexible supercapacitors." *Journal of Materials Chemistry A* 1.1 (2013): 63-67.

Chapter 7

Conclusions and perspectives

This thesis comprises the comparison of energy storage properties of all fabricated composites. Out of three different types of graphene based filler loaded cellulose composites, there are several kinds of systems were discussed in terms of their dielectric and electrochemical properties.

The previous reports on dielectric properties of polymer composites mainly focused on the lower frequency regions. Generally, the dielectric performance of a material increases with frequency-lowering, due to the space charge contribution. At low frequencies, the external effects, such as the presence of surface layers (for example, due to the formation of Schottky barriers) often govern the dielectric response. To provide the real, intrinsic material properties, we have therefore investigated the dielectric properties at the highest frequency region of 1 MHz and got significant enhancement than reported studies. This approach gives a new insight to the exact performance of materials on dielectric charge storage applications.

First system explains the fabrication of flexible and eco-friendly films from ammonia-functionalized graphene oxide (NGO) nanoplatelets and wood-based cellulose nanofibrils (CNF) vs. TEMPO pre-oxidized (carboxylated) CNFs (TCNF) by the solvent casting method. Various CNF-NGO (CNG) and TCNF-NGO (TCNG) composite films prepared with 0.5–3 wt% of NGO were analysed structurally by FTIR and XRD spectroscopies, and evaluated optically by UV-Vis spectroscopy. Good dispersibility of NGO sheets in the randomly-distributed (CNF) or dense and parallel-oriented (TCNF) cellulose nanofibrils were observed by morphology analysis using SEM.

Such a synergistic effect of both components contributes to ultra-strong and ultra-stiff composite films with good mechanical and thermal stability, although they were more brittle with a smoother surface and lower transmittance by using TCNF based films due to the stronger physico-chemical interactions with NGO. The dielectric performance was verified with higher (3 wt %) NGO loading capacity which resulted in a dielectric constant of ~ 46 vs. ~ 52 and conductivity of $\sim 2.07 \times 10^{-4} \text{ Sm}^{-1}$ vs. $3.46 \times 10^{-4} \text{ Sm}^{-1}$ for CNG vs. TCNG films, respectively, at a frequency of 1 MHz, showing enhancement than reported studies. Cyclic voltammetry results show the comparable energy storage ability and electrochemical performance of the composite films as electrodes with a small amount of NGO.

An effective dry method to reduce graphene oxide (GO) to graphene in a film of pristine and oxidized cellulose nanofibrils (CNF) by UV irradiation in the presence of nitrogen gas were discussed in chapter five as a second system. The presented methods of UV induced reduction of graphene oxide (GO) to graphene on pristine and oxidized cellulose nanofibrils (CNF) are promising alternatives to solvent based treatments avoiding the deterioration of material properties and the use of organic solvents. The formation of graphene and removal of carbonyl and carboxyl moieties were confirmed by infrared spectroscopy, UV-Vis absorbance and potentiometric charge titration. The crystallinity of native and reduced composites was elucidated by x-ray diffraction measurements. The resulting graphen nanocomposite films remain flexible and show improved mechanical performance and competitive dielectric properties. After 5 hours of UV irradiation a 3 wt% graphene loaded film increased its dielectric constant from 68.9 to 88.9 for pristine and 74.1 to 121.61 for oxidized cellulose. The AC conductivity reaches values of $9.37 \times 10^{-4} \text{ S m}^{-1}$ for pristine and $5.3 \times 10^{-3} \text{ S m}^{-1}$ for oxidized cellulose. The electrochemical performance of the samples was tested by cyclic voltammetry and electrochemical impedance spectroscopy. UV

treated samples showed a higher capacitive nature than untreated samples demonstrating their potential use in energy storage applications. The unexpected UV induced reduction of graphene oxide to graphene in presence of cellulose are promising alternative to solvent based methods. Alternative polymer composites could be used to obtain similar properties.

In the sixth chapter, the effect of structure and composition of dense film-like xerogels and micro-porous cryogels or aerogels, prepared from cellulose nanofibrils (CNF) and reduced graphene oxide (RGO), were investigated related to their dielectric performance and electrochemical energy storage abilities. A very small content (5 wt%) of RGO in xerogelic composite was shown to give a relatively high dielectric constant of ~ 85 and ~ 164 and an ac electrical conductivity of 0.0028 S/m^2 and 0.0072 S/m^2 at 270 K and 370 K, respectively, at a frequency of 1 MHz. On the other hand, micro- and longish porous cryogels were observed to show a specific capacitance of $\sim 460 \text{ F/g}$ evaluated by cyclic voltammetry and electrochemical resistance of $12\text{-}15 \text{ } \Omega \text{ cm}^2$ obtained by electrochemical impedance spectroscopy measurements. High performing dielectric xerogels have the potential to be used as green energy storage materials in engineering and electronic fields, while their cryogel counterparts as electrodes for electrochemical storage devices. The comparison of electrochemical properties of film like xerogels and porous cryogel composites by vacuum filtration and one-directional freezing respectively. We believe that it is original to compare the electrochemical properties of film like xerogels and cryogels prepared with different freezing temperatures.

The potential integration of energy storage technologies was discussed for the optimal energy management and were also be considered within this thesis. Although, significant progress has been made in the fabrication of bio based energy storage composites, we have a long way to go for achieving enhanced engineering properties for better performance. Research should be

focused on the cellulose based composites with hybrid fillers of graphene derivatives and conducting nanoparticles for high dielectric materials. In addition with the TEMPO oxidization of cellulose fibers, different types of surface modifications should be tried for the better performance. The cellulose based matrices should alter with other biopolymers like chitosan, chitin, gelatin, alginate etc. for exploring biopolymers and for property enhancement. The UV induced reduction of graphene oxide in the cellulose matrices should be extended to the other biopolymer matrices for effective reduction for an environmental friendly dry method. Proper exploitation of differently fabricated composites such as xerogels, aerogels, porous foams, etc. will give more insight to the energy storage technologies.

Publications

1. " Beeran, Y., Bobnar, V., Gorgieva, S., Grohens, Y., Finšgar, M., Thomas, S., & Kokol, V. (2016). Mechanically strong, flexible and thermally stable graphene oxide/nanocellulosic films with enhanced dielectric properties. RSC Advances, 6(54), 49138-49149. <http://pubs.rsc.org/en/content/articlepdf/2016/RA/C6RA06744A>
2. "A flexible, disposable hydrogen peroxide sensor on graphene nanoplatelet coated cellulose" O. Koshy, Y.B Pottathara, M. Finšgar and S. Thomas. Current Analytical Chemistry, 13, 2017 <http://www.eurekaselect.com/node/151940/article>
3. "***Solvent free reduction of graphene oxide-nanocellulose composites for energy storage applications***" Y. B. Pottathara, S. Thomas, Y. Grohens, V. Bobnar, M. Finšgar V. Kokol, and R. Kargl (submitted)
4. "***Highly Performing Dielectric Paper and Aerogels based on Reduced Graphene Oxide filled Cellulose Nanofibrils for Energy Storage applications***" Y. B. Pottathara, S. Thomas, Y. Grohens, V. Bobnar, M. Finšgar and V. Kokol (submitted)